Wireless Links for Telecare and Telemedicine Applications using Compact Body-Worn Antennas.

Waddoup, W. Dave

Wireless Links for Telecare and Telemedicine Applications using Compact Body-Worn Antennas

PhD Student:

W. Dave Waddoup

Supervisors:

Prof. Yang Hao &

Dr. Akram Alomainy

A Thesis Submitted to the faculty of the University of London
in partial fulfillment of the requirements for the degree of

Doctor of Philosophy

School of Electronic Engineering and Computer Science,

Queen Mary University of London, E1 4NS, United Kingdom

June 2013

PhD #2\PhD Thesis\Drafts\Tranche#3\WDW_PhD_Thesis_1.0_SS

12th Jul 2013

TABLE OF CONTENTS

ABSTRACT

This thesis concerns the design of body-centric wireless communications for short-range indoor Telecare/Telemedicine applications. Such communications are starting to be used to convey key, relatively low data-rate body-sensor data wirelessly between on-body sensor node(s) located on potentially mobile clients/patients and fixed off-body Access Point(s).

From the outset, key *practical* considerations/constraints were assumed; in particular that, wherever possible, *existing* components (including antennas) and established protocols would be employed. This approach should enable existing manufacturers of mobile wireless components to rapidly adapt to the potential Telecare/Telemedicine market segment with minimum R&D capital outlay.

In addition, maximum user convenience of the on-body nodes has been taken into account to ensure that they are readily accepted and hence actually used.

As anticipated, using existing mobile antennas (designed for nominally free space use) in close proximity to the human body poses several limitations. These are quantified here for a particular candidate commercial device. In the process, however, a novel *un*anticipated effect of the nearby body was also discovered; namely that the body completely depolarises the (otherwise reasonably polarised) antenna patterns. A *potential* physical explanation for this effect is identified and evaluated by means of analysis based on a *modified* Geometric Optics approach. The result of this analysis agrees with those simulated and measured here to remarkable accuracy.

The thesis then presents several multi-antenna schemes to overcome these severe limitations and identifies that best suited to the indoor Telecare/Telecommunication application here. Simulations at the Physical Layer are reported with this optimum

single-input multiple-output (SIMO) antenna scheme for a typical indoor scenario. These quantify the overall system performance when such measures are adopted, demonstrating that it is adequate in this role.

Finally, promising techniques are suggested for Future Work which could afford further significant system improvements for future upgrades of the solution presented here. In particular, the use of metamaterial techniques are indicated which could substantially reduce on-body transmit powers currently required. This would give highly desirable increases in battery lifetimes for the mobile battery powered on-body nodes.

PUBLICATION LIST

Papers:

i) *Waddoup W.D., Hao Y., Alomainy A., 'Effects of Using a Low-Cost Antenna in Close Proximity to the Body', presented at European Conference on Antennas and Propagation (EuCAP 2011), Rome, April 2011.*

Journals:

i) *Waddoup W.D., Foster R.N., Alomainy A., and Hao Y., 'Effect of Depolarised On-body Antenna on Spatial and Depolarisation Diversity Schemes in Off-body Radio Channels', IEEE Antenna Wireless and Propagation Letters (AWPL) – submitted April 2012.*

ii) *Waddoup W.D., Foster R.N., Hao Y., and Alomainy A., 'A Physical Explanation of the Depolarising Effect on an Unshielded Antenna when Located in Close Proximity to Human Body', IEEE Antenna and Wireless Propagation Letters (AWPL) – to be submitted May 2013.*

Trade Journals:

i) *Kingsley S., 'Personal Healthcare Goes Wireless with Commercial 2.4GHz Technology', Electronics Weekly, 16-22 May 2012*

ACKNOWLEDGEMENTS

I would like to dedicate this thesis to my wife, Shenagh Clare Waddoup, without whose patience and encouragement it would not have been completed. As a dedicated social worker, responsible for allocating limited resources most effectively to vulnerable clients, her ongoing vision and that of her profession for the use of Telecare to assist them has helped me to weather the more frustrating periods during my studies.

I would like first to thank my primary supervisor Prof. Yang Hao for his technical input and encouragement. In particular, his weekly seminar approach, requiring every student to briefly present the findings of their studies, has proven to be an excellent discipline to regularly assess progress achieved, thereby identifying the most effective immediate step forward. These also provide a good opportunity to critically assess potential ideas with informed colleagues in a semi-formal environment.

I would also like to make special mention of Dr. Akram Alomainy who, as my secondary supervisor provided valuable technical input and consistent encouragement. As my studies progressed, I have increasingly come to appreciate his sound advice and support. This is especially true of their more difficult phases towards their end and during the writing up when he found the time to critically appraise the thesis in its entirety.

There are many other Queen Mary colleagues and friends to whom I am grateful for their technical input. Although too numerous to mention all, I would especially like to thank Dr. Robert Foster, Dr. Khalid Rajab and Mr. Max Munoz.

At the same time, I would also like to record my thanks to Queen Mary’s support and administration staff for their assistance throughout my studies; in particular Mr. Ho Huen for ensuring that the department's computing facilities was run in an effective manner, and Mrs. Melissa Yeo for efficiently managing the administration aspects of the research department.

Lastly, I am also most grateful to Prof. Simon Kingsley of Antenova and Dr. Dean Kitchener of AceAxis (formerly Standard Telecommunication Laboratories). Despite their busy schedules in industry, Simon was kind enough to provide antenna samples and find time to encourage me to investigate their application to the less conventional Telemedicine/Telecare field, and Dean found time to respond promptly to queries on specialised technical issues offering his valuable expertise.

I would also like to record my thanks to the Engineering and Physical Science Research Council (EPSRC) for funding, including a studentship, which has enabled me to pursue this study.

Finally, it remains my sincere hope that my efforts over the last 48 months will do something to hasten the long awaited and much needed deployment of next-generation Telecare/Telemedicine solutions; in particular, those employing on-body sensors to directly generate objective on-body data without active participation by the user in online Q&A sessions. These should reduce the need for human intervention by Service Providers, relieving them from needlessly addressing more routine cases, and allow them to concentrate their resources on those having higher priority.

LIST OF ACRONYMS

A

ADC	Analogue to Digital Convertor
AoA	Angle of Arrival
AoD	Angle of Departure
AP	Access Point
AWP	Antennas Wireless and Propagation
AWPL	Antennas, Wireless and Propagation Letters

B

BAN	Body Area Network
BCL	Body Centric Laboratory (located at QMUL)
BER	Bit Error Rate
BMI	Body Mass Index

C

CDF	Cumulative Distribution Function
COTS	Commercial Off The Shelf

CO-pol	Co-Polar(ised)
CST	Computer Simulation Technology™ (of America Inc.)

D

2-D	Two Dimensional
3-D	Three Dimensional
D	(inter element) separation
dB	decibels
DPSK	Differential Phase Shift Keying (modulation scheme)

E

EBG	Electromagnetic Band Gap
ECG	ElectroCardioGraphy
EEG	ElectroEncephaloGraphy
EGC	Equal Gain Combining
EPSRC	Engineering and Physical Science Research Council
ERC	Equal Ratio Combining
EuCAP	European Conference on Antennas and Propagation

F

FCC	Federal Communications Commission
FF	Far Field
FS	Free Space
FT	Fourier Transform

G

3G	3^{rd} Generation
GND	Ground (Plane)
GO	Geometric Optics

H

HDA	High Dielectric Antenna
HMG	Her Majesty’s Government (UK)
HP	Horizontally Polarised
H-pol	Horizontally Polarised

I

IEEE	Institute of Electronic and Electrical Engineers
IET	Institute of Engineering and Technology
ISM	Industrial Scientific and Medical (band)
ISO	International Standards Organisation
IoP	Institute of Physics

L

L	Length
LOS	Line Of Sight

M

MATLAB	MATrix LABoratory (MathWorks Inc)
MIMO	Multiple Input Multiple Output

MISO	Multiple Input Single Output
MRC	Maximum Ratio Combining
MWJ	MicroWave Journal
N	
NASA	National Aeronautics and Space Agency
NB	Narrow Band
NF	Near Field
NLOS	Non Line Of Sight
P	
PC	Personal Computer
PCB	Printed Circuit Board
PDG	Polarisation Diversity Gain
PEC	Perfect Electric Conductor
PhD	Doctor of Philosophy
PHY	Physical (layer)
PMC	Perfect Magnetic Conductor
Q	
QMUL	Queen Mary University of London
R	
R&D	Research and Development
RF	Radio Frequency

Rx	Receive(r)

S

SBR	Shooting Bouncing Ray
SC	Selection Combining
SDG	Spatial Diversity Gain
SIMO	Single Input Multiple Output
SISO	Single Input Single Output
SNR	Signal to Noise Ratio
SW	Surface Wave

T

T	Thickness
TBD	To Be Determined
TEG	Thermo-Electric Generator
Tx	Transmit(ter)

U

UK	United Kingdom
ULP	Ultra-Low Power
UPW	Uniform linear Plane Wave
USB	Universal Serial Bus
UWB	Ultra Wide Band

V

VNA	Vector Network Analyser
VP	Vertically Polarised
V-pol	Vertically Polarised

W

W	Width
WAN	Wide Area Network
WB	Wide Band
WI	Wireless Insite (Remcom™)
WLAN	Wireless Local Area Network
WPAN	Wireless Personal Area Network
WSN	Wireless Sensor Network

X

X-pol	Cross-Polar(ised)

Z

Z	complex impedance

Chapter 1

Introduction

1.1 Context of Study

It is now widely accepted that developed societies are becoming increasingly characterised by:

i. more aged, less mobile/healthy, population demographics,
ii. the rising cost of remedial medical procedures, and
iii. diminishing financial resources to meet this increasing demand.

To tackle these generally conflicting issues, Telecare/Telemedicine, involving pre-emptive measures to monitor clients/patients in a timely fashion within their own home, is beginning to be deployed to provide a much more cost effective, and less traumatic, solution than subsequent remedial treatment in a hospital or other institution [1], [2], [3] and [4].

Further, it is found that most clients/patients, when faced with this situation, generally prefer to be (and consequently respond more favourably when) monitored within their own home environment rather than within an institution, which is currently the only alternative option.

The primary advantage of *wireless* Telecare/Telemedicine solutions, with battery powered wireless-equipped on-body sensor nodes, is that they allow remote monitoring of clients/

patients without unduly affecting their mobility. This allows them to continue everyday life in a more independent fashion with a minimum of intervention by outside agencies, thereby greatly enhancing their dignity and self-reliance; factors that are increasingly being regarded as essential to their well-being by welfare and health professionals.

Figure 1.1, below, illustrates the simplest possible architecture of wireless link(s) for Telecare/Telemedicine applications allowing remote monitoring of client/patient parameters provided by several sensors in an indoor scenario.

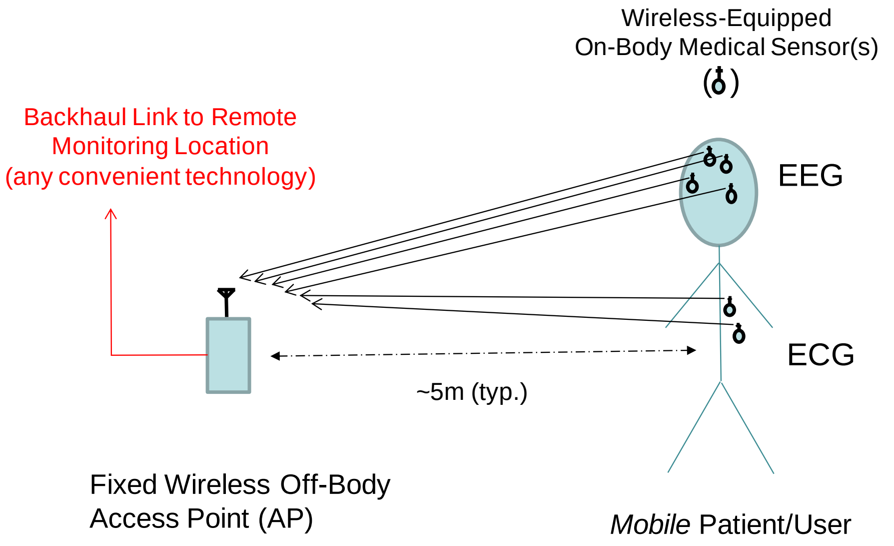

N.B. Only simple SISO wireless links shown here for illustrative purposes

Figure 1.1: Example Telecare/Telemedicine Wireless Link Architecture

Although wireless solutions have long been cited as the ideal candidate for such Telemedicine/Telecare applications, key acceptability requirements still need to be addressed to stimulate their more universal adoption. These requirements include:

i) low cost; particularly for the more numerous (and possibly even disposable) on-body sensor nodes,

ii) small size for the wireless-equipped on-body sensor nodes; in particular a low profile to ensure user acceptability,
iii) ultra low power consumption for these on-body nodes, to ensure long battery life ,
iv) the ability to co-exist with other wireless nodes and wireless-sensitive electronic equipment which may be in use within their immediate vicinity, and of course
v) the maintenance of high integrity for the key medical data being communicated.

It is interesting to note that of the twelve clinical trials reported in a recent volume of the Journal of Telemedicine and Telecare [2], only one concerns on-body sensor readings. The rest comprised (relatively subjective) question and answer sessions by online teleconferencing between the client/patient and a medically trained person. Further, the on-body (motion) sensor device mentioned in [2] stored considerable information for subsequent downloading to a suitable USB-equipped device for storage/analysis when available/convenient. So, unlike a *wireless*-equipped on-body sensor under consideration here, the information could not be transmitted in real-time fashion, but constituted a more long-term monitoring (rather than pre-emptive) measure.

1.2 Aims of this Study

Besides obtaining a PhD, from the outset of this study a key aspiration of the present author was to realise a truly affordable wireless sensor communication link as well as satisfying the technical and user acceptability criteria given in the preceding section 1.1 above. By satisfying this objective, it is hoped that the study might contribute something of value to the well-being of the society that financed it.

Experience indicates that the most successful engineering developments, in common with most other enterprises, generally start by considering the simplest *viable* solution [5]. Then, once this most basic viable solution has demonstrated user/provider acceptability, increased sophistication can be incorporated into subsequent versions to further refine the basic solution’s performance and add additional features. Generally, these refinements are only incremental, but sometimes a more drastic redesign is required to implement a major improvement. Therefore, given the current start-of-the-art, the present study has adopted this incremental approach.

Investigations to be presented here will show that *provided additional measures are taken*, in particular diversity-gain afforded by multi-antenna techniques, existing narrowband Commercial off the Shelf (COTS) ISM-band RF hardware, will suffice for the most common low data-rate applications required for more routine client/patient monitoring. This finding includes miniaturised COTS antenna elements. For example, in the IEEE 802.15.4 [6] protocol/standard for the 2.4GHz ISM-band, typical data rates are 90-115kHz, which are entirely consistent with key basic information such as:

i) is the patient/client breathing in a normal fashion?
ii) is the patient/client's heart beating in a normal fashion?
iii) has the patient/client recently experienced deceleration consistent with a fall?

If, however, the additional measures identified here were not included in the design, the study shows that the substantial innate drawbacks of using such COTS antenna elements in close proximity to the body would preclude their on-body use in such applications.

Finally, besides being more affordable, novel applications that employ existing COTS hardware elements (designed to officially recognised standards), will be electrically compatible with existing approved electronic equipment. This advantage is equally desirable from a service provider's point of view, and would avoid the cost and time to market delay associated with getting new developments certified for use I this critical application.

1.3 Scope/Extent of this Study

Only short-range *indoor* wireless scenarios and propagation, appropriate for less mobile housebound clients/patients, are investigated here. Consequently, the IEEE series of protocols/standards for Wireless Personal Area Networks (WPANs) [6] are assumed for use. Modifications to existing conventional longer-range outdoor wireless systems (e.g. cellular) may be better suited for monitoring clients/patients able to venture outdoors [7].

Thus, only the Physical (PHY) Layer is studied here and, for compatibility and interoperability with existing associated devices, the IEEE 802.15.4 [8] protocol/standard is assumed to apply to higher layers.

Since the great majority of Telemedicine/Telecare applications will only involve fairly intermittent communication of information at a relatively low data rate, *only low data rate* wireless link types have been considered in the present study (specifically 802.15.4 types, with 5MHz channel bandwidths, giving typically 1Mbps & 250kbps data rates [8], [9], [10], and [1]).

Higher data rates, for example involving imagery of within-body cavities for investigative procedures and keyhole surgery, would be useful, but their specialised usage would be far less universal. In such cases, more sophisticated and costly wideband wireless links (IEEE 802.15.3 type) [12], are more likely to be justified. References consulted concerning such wideband techniques include [13], [14], [15], [16] and [17]. These cover aspects such as channel characterization for links between on-body to off-body nodes and between nodes located on a common body (Body Area Networks (BANs). Also addressed are wideband on-body antenna design techniques.

The presence of *multiple* on-body wireless nodes, and the consequent opportunity for ad-hoc networking between these, cannot be guaranteed in all cases. Further, networking considerations between such multiple on-body nodes would constitute an added dimension of complexity outside the scope of the present study. So, instead, the study here was limited to investigating techniques necessary to guarantee reliable information transfer between a *single on-body wireless sensor node* and its *single associated Access Point node*, as previously illustrated in Figure 1.1 here. However, as will become evident later, this single off-body AP node will need to include two antennas.

Nonetheless, ad-hoc networking between different on-body nodes, comprising a Body Area Network (BAN), might be of particular value in routing data to the node within this BAN having the most favourable propagation condition to its associated off-body Access Point node. For example, this might be an effective means to overcome the inevitable body blockage between a single on-body node and its associated off-body Access Point node that occurs in some instances. As a result, this BAN concept is included in Chapter 6 which includes ‘Suggested Further Work’.

The author's original remit was to investigate potential advantage of wireless equipped on-body sensor nodes, each having a multi-element *on*-body antenna. However, at an early stage, it became apparent that twin element *on*-body antennas afford only limited technical merit (less than twice the data-rate), but have significant disadvantages in terms of reduced acceptability to service providers (increased complexity/capital cost) and reduced user acceptability (inconvenience, due to more than doubling of physical size).

So instead, attention was turned to the more attractive option of having multi-element antennas at the less numerous *off*-body Access Points, where size is also less constrained.

1.4 Study Methodology

To study the *on-body antenna* aspects the following strategies were employed:

i) Numerical simulations were conducted using the well established CST electromagnetic software package. To do this, an accurate model of the candidate COTS antenna and a relatively simple 3-layer dielectric sandwich representation of the body had to be written by the user.

ii) Measurements of the COTS 'Rufa' antenna's RF performance, in free-space and on-body were made in QMUL's anechoic chamber to confirm these simulations.

To investigate the *system* implications of the PHY layer in the indoor scenario considered here, the following strategies were adopted:

i) Simulation of propagation paths, using the well established Wireless Insite (WI) ray-tracing software package. Output data of the raw signal strengths generated by this WI package was then processed to provide diversity and analysed using a MATLAB programme written by the present author,

ii) Well established technical journals (e.g. IEEE Spectrum magazine, NASA Technical Briefs, Medical Design Briefs, and Microwave Journal (MWJ)) with associated webinars were regularly monitored. This allowed the present author to keep abreast of the latest developments in the wireless

Telecare/Telemedicine field and the latest hardware offerings that might be useful in this area.

1.5 Contributions of Author to Original Research

Reference [18] gives no fewer than 13 definitions of novelty and indicates that these are by no means exhaustive. However, arguably the most stringent definition, being ‘adding to knowledge in a way that that has not been done before’, is taken here.

On this basis, several interesting ‘novel’ research contributions emerged as a natural consequence of developing a viable solution in this study. These contributions include:

i) The observation that an otherwise reasonably polarised largely omnidirectional antenna in Free-Space becomes completely depolarised when it is relocated to be within close proximity to a sizeable dielectric object such as the human body,

ii) Identifying the underlying physical mechanism to adequate explain this unanticipated depolarisation effect,

iii) Demonstrating the need for off-body diversity gain to offset fading in multipath-rich indoor environments here, thereby permitting substantially increased times between on-body node battery replacements, and

iv) Quantifying the effect of the on-body antenna depolarisation effect on the achievable diversity-gains for two types of diversity scheme; spatial and polarisation diversity. This identified that of the two schemes considered, spatial diversity is least affected by the on-body depolarisation effect and is therefore the more effective.

It is anticipated that these novel contributions, plus material presented here, will satisfy the novelty and competence criteria of a PhD, whilst at the same time achieving the author’s other aspiration to realise a viable system.

Further, in addition it is considered that much of the other work reported within this thesis falls within the remit of the other (arguably less stringent) definitions given in [18].

1.6 Outline of Thesis

A brief outline of this thesis is presented here. It is noted that each chapter ends with conclusions summarising findings appertaining to that particular chapter.

Chapter 1, of which this section is the final part, has set the study in context and stated the current author’s main aspirations. The aim of achieving a viable system has resulted in the study being focused in directions which were judged to be of more practical value, whilst de-emphasising other avenues which were considered to be less so. Justification of the choices made is given as/when appropriate throughout the text. Chapter 1 then proceeded to describe the scope/extent of the study necessary to fulfill these two aims, and the manner in which the study was conducted to satisfy the necessary rigour for a PhD. Finally, the contribution of the present author to the furtherance of research knowledge has been clearly set out to enable the reader to readily assess this aspect.

Chapter 2 describes the initial exploratory literature review of existing *academic* publications, along with an ongoing literature review prompted by subsequent study as it uncovered additional new areas requiring consideration. *Trade* publications were also regularly monitored throughout the study to ensure that the author remained aware of new technology developments, which might be of particular significance in this rapidly advancing wireless sensor field.

The initial exploratory literature review, described in section 2.5, revealed that inexpensive COTS unshielded antennas, designed primarily for Free-Space (FS) use, have a markedly modified RF performance when relocated to be in close proximity to the human body. In particular, as anticipated, a substantial reduction in antenna efficiency and also detuning were reported when on-body.

The present study focuses on means adopted to address these two deficiencies to yield a viable system in the *near*-term. In particular, section 2.7 describes literature surveyed to choose the two most promising diversity techniques; spatial and polarisation diversity.

These candidates were subsequently investigated in greater detail in chapter 5 for the indoor propagation scenario considered here.

Section 2.8 summarises useful references which assisted the selection of the most appropriate (networked or non-networked) architecture topology to use in the current Telecare/Telemedicine application. It also considers the most appropriate multi-antenna architecture to use here. The choices adopted for both aspects resulted from the outcome of the literature research, so justification of these choices is also included in section 2.8.

In addition, towards the end of the ongoing literature search, more novel measures were uncovered, which might be applied to a *longer*-term system. These could circumvent, and hence address, the unshielded antennas' fundamental on-body deficiencies, without compromising the inherently low-profile nature of these antennas which is essential for user acceptability. Section 2.3.2 outlines the significant improvement on battery lifetimes that they are expected to produce for battery-powered on-body wireless sensors.

However, since these *longer*-term measures are beyond the scope of the present study, they are included instead as part of Suggested Future Work programme in section 6.2.

Towards the end of this study, a previously published paper [19] was found describing the *reduction in mutual coupling* effect experienced between a *pair* of closely separated unshielded antennas when located in close proximity to the human body. This confirmed the same finding observed and reported by the present author in reference [20] and detailed here in section 3.9 here. Prior to the discovery of reference [19], the reduced mutual coupling effect reported in [20] was believed to have been novel.

However, ongoing literature searches have yet to reveal any previously reporting of the *depolarising* effect of the nearby body on the unshielded antenna's patterns could be found. So the reporting of this effect, also given in [20] by the present author and included in more detail here in section 3.6, is still believed to be genuinely novel.

As previously intimated, chapter 3 describes extensive CST electromagnetic simulations, and confirmatory measurements, carried out by the author to quantify the effect of the nearby body on a candidate unshielded inexpensive COTS antenna when relocated to be on-body. The particular candidate antenna used here was Antenova's 'Rufa' antenna [21].

As well as confirming the *anticipated* (efficiency reduction and detuning) effects of the nearby body, section 3.5 describes the *un*anticipated depolarisation effect when the antenna is on-body.

Chapter 4 then describes an analysis conducted to identify a physical explanation of this *on*-body depolarising effect. Initially, it was thought that this *un*anticipated effect might need to invoke a relatively sophisticated propagation mechanism; for example surface waves. Interestingly, however, despite the extremely close proximity of the body in this application, a conventional simpler geometrical optics approach, in which the orthogonal co-polar and x-polar components were analysed separately, was found to provide a co/x-polar ratio that was in remarkable agreement with those given by simulation reported later in sub-section 3.5.9. User-written MATLAB code for this analysis is include here as Appendix A3.

In this regard, it is not argued that surface-wave type propagation is absent here; rather conventional propagation means affords a perfectly adequate primary means and involving surface-wave type propagation may only be required as a second order mechanism to further refine this explanation.

Chapter 5, then proceeds to investigate the effect on the wireless link overall *system* performance of the severe reduction in efficiency of the unshielded candidate on-body antenna. This includes a computation of the system link budget and a sophisticated Wireless Insite (WI) simulation of the propagation effects in the multipath-rich indoor scenario here to derive the signal strengths as the mobile user, wearing the on-body wireless equipped sensor, moves towards two closely-spaced fixed Access Point (AP) antennas. A user-written MATLAB© programme, given here in Appendix A1, then performs a statistical analysis of these signal strengths along the user route.

The option of having two antennas at the Access Point is included in the WI simulation to determine the diversity-gain afforded by the resulting two-branch diversity scheme which is necessary to offset some of the substantial reduction in the on-body antenna efficiency. In the *absence* of this diversity-gain, chapter 5 shows that the on-body transmit power would be unacceptably large, giving rise to greatly reduced on-body battery lifetimes. Both spatial diversity and polarisation diversity schemes have been investigated here.

Chapter 6 summarises the overall conclusions reached at the end of this study to devise a wireless equipped on-body sensor system that is both technically and commercially viable in the *nearer*-term. Chapter 6 also includes Suggested Further Work. This draws on promising topics, mentioned in passing throughout this thesis, which might substantially improve the overall performance for *longer*-term upgrades of the nearer-term system as currently devised here.

This thesis then concludes with a reference section, followed by an appendices section. The appendices contain additional information that may be found useful at a later date and are therefore included for completeness.

Chapter 2

Literature Review and Background Study

2.1 Introduction

Upon commencing this research study (when its outcome was largely indeterminate) the IEEE Xplore search engine was used to conduct an initial broad-ranging literature survey by way of a familiarisation exercise. This covered areas that appeared to be of likely interest to the study as it was originally proposed.

Thereafter, as the study progressed and the more relevant topics became apparent, the same search engine was employed regularly to conduct more topic-specific literature searches to derive state-of-the-art in-depth information on these areas.

In addition, ongoing monitoring of the well established commercial press (for example Microwave Journal) was performed. This strategy enabled the author to remain aware of new technology developments, so that the study could be steered in the direction which was likely to be most productive in terms of a realisable end-product.

2.2 Existing Literature on Indoor Propagation

References [22], amongst others, provide a good generic description of the manner in which the received signal level varies for a short-range wireless link between a mobile node and its associated fixed Access Point node.

In particular, three types of variation are observed:

i) Long term: power-law variation due to the changing transmitter/receiver range,
ii) Medium term: lognormal variations due to shadowing by various obstacles in the direct Line-of-Sight (LOS) path
iii) Short term: Rayleigh or Ricean variations due to constructive/destructive combinations of the various multipath signals and the direct signal (if present)

The exact form of these types of variation and their relative extents are determined by the propagation environment (e.g. indoor/outdoor, rural/urban, etc.) and more detailed link parameters (e.g. antenna heights, antenna patterns, etc.).

It is well known (reference [23] and [24], for example) that indoor environments are particularly rich in multipath signals due to the many scattering surfaces (such as walls, floors and ceilings) present in close proximity to both the transmit and receive nodes.

The vector combination of the indirect multipath signals (and any direct signal which may be present) produces a wide variation in the composite received signal strengths at elements at different locations within a multi-element antenna. In particular, deep nulls (up to 20dB) can be experienced at some element(s), whilst slight signal strength improvements can be present at others. Thus, the use of individual channels experiencing deep nulls should be avoided, or their effect on the composite signal minimised, to ensure that the link still functions reliably. This forms the basis of multi-element diversity techniques to be considered in more detail in Chapter 5.

Now an essential prerequisite for any *multi*-element antenna scheme to effectively mitigate these deep fades (or enhance link capacity with Multiple Input Multiple Output (MIMO) architectures), is that sufficient scattering should occur within the propagation channel to ensure that the multiple antenna elements at the receive end of the link receive sufficiently different (i.e. largely uncorrelated) signals. Such a channel is then deemed to be sufficiently multipath-rich for this purpose.

For example, in the extreme case of the total absence of any multipath, multi-element antennas afford no improvement whatsoever. At the other extreme, when no direct Line Of Sight (LOS) path is available due to blocking by an intervening obstacle(s), diversity techniques *rely* on the presence of one or more *in*direct multipath signal(s) to provide an alternative communication path(s) by which the information can be conveyed.

More quantitatively, reference [25] indicates that, for *space* and *pattern* diversity, sufficiently different signals at the multiple antennas are achieved when the correlation coefficient between them is ≤0.7.

2.3 Existing Literature on Effects of Nearby Body on *Individual* (Unshielded) Antennas

As already described in section 1.2, it was decided at an early stage in the study to determine whether or not it might be possible to use an existing low-cost miniaturised Commercial-off-the-Shelf (COTS) antenna(s) for the on-body sensor node. For this application, such a COTS antenna designed specifically for direct on-body use would have been the most appropriate. However, in so far as could be determined, such a COTS antenna has yet to be produced.

Instead, therefore, data sheets were obtained for several miniaturised COTS antennas, designed primarily for use in portable handset devices. These indicated that they all had pretty similar performance; in particular, nominally isotropic antenna patterns to allow equally effective operation of the portable device whatever its relatively arbitrary orientation.

However, because Antenova™ showed particular interest in the work proposed here for the Telecare/Telecommunications application, were relatively local and willing to supply free samples and support in this largely untapped market, their 'Rufa'™ antenna was chosen for study here. Nonetheless, it is acknowledged that antennas from other manufacturers may well have been equally suitable here.

In common with many COTS devices intended for portable applications, the COTS ‘Rufa’ antenna structure is mounted directly on a thin high dielectric substrate, as given by the drawings in reference [21] and a photograph shown later as Figure 3.1 here. Being planar, this thin dielectric is also very amenable to manufacture. This technique (plus folding) is employed to reduce the *physical* size of an antenna, to allow its inclusion within a confined space, whilst preserving its original *electrical* size to maintain its 2.4GHz resonant frequency unchanged.

Being designed for largely Free-Space (FS) use, the *un*shielded ‘Rufa’™ COTS antenna selected for on-body investigation here will be considerably affected by its close proximity to the human body in the present Telecare/Telemedicine application. In particular, references [26] and [24] indicate that unshielded antenna-types in close proximity to a dielectric object suffer some detuning (lowering their resonant frequency) and a considerable loss in efficiency. As they stand, both these effects could preclude the link functioning, so measures to address them are investigated here.

As regards the *detuning* effect, reference [27], shows the effect of slightly different user handgrips (specifically the location of the index finger) on a 2.0GHz mobile handset having an internal antenna at two different locations within it. This shows that the frequency is reduced by between 2% and 13%, depending on the physical length of the antenna. By way of comparison, measurements and simulations, reported in Chapter 3 here (and [20]) by the current author, of the COTS ‘Rufa’ antenna when mounted in Free-Space and *directly* on-body show a frequency reduction of 13%. However, whilst interesting, direct comparison is not particularly meaningful in these rather different test cases.

Regarding the antenna *efficiency reduction* effect when located in close proximity to the body, reference [26] notes that even a non-metallic mobile handset enclosure has a noticeable effect on the efficiency of the antenna; sufficient, in fact, to make the term *handset* efficiency (i.e. the efficiency of the handset as a whole) more meaningful to mobile design than *antenna* efficiency alone.

In this regard, simulations reported in reference [27] indicate that the presence of a large dielectric block, having tissue-like RF properties and located about 13mm away from the antenna to emulate the effect of the hand, produced an efficiency reduction of typically 6.5dB. Again, by way of interest, measurements and simulations, reported in Chapter 3 here (and [20]) by the current author, of the COTS 'Rufa' antenna when mounted in Free-Space and only 3mm above the body show a reduction in efficiency of about 13dB. Although direct comparison is unlikely to be very meaningful in these rather different test cases, at least the much closer proximity of the body in the present case with the 'Rufa' antenna (3mm) does show much greater efficiency loss than for the 13mm case in [27].

As regards the *detuning* effect, in the present case of the COTS 'Rufa' antenna used *directly* on-body, the 13% reduction in resonant frequency is sufficient to cause its resonant frequency to fall outside (thereby precluding its use in) the ISM frequency band (2.4000GHz to 2.4835GHz). Fortunately, however, this frequency reduction is sufficiently small that only straightforward measures need be taken to redress it and restore the antenna's resonant frequency band back to that required.

However, when located only 3mm above the body, the more drastic 13dB reduction in *efficiency* of the unshielded COTS 'Rufa' antenna cannot be countered in a similar straightforward fashion. Therefore, more sophisticated measures at the *system* level are needed to redress this deficiency. These involve diversity techniques, as investigated in detail in Chapter 5 here.

Finally, at the start of the study, further references concerning the use of antennas located on or within the human body were considered. These include [28] and [29].

2.3.1 ***Near*-Term Measures Adopted *here* to Address Effects of Nearby Body**

In the *near*-term, antenna *detuning* (specifically lowering the antenna's resonant frequency) due to the presence of the body in close proximity can be addressed by:

i) Scaling (reducing) the Free-Space size of the antenna slightly to increase its resonant frequency back to that required for on-body operation here, or

ii) Introducing a small air-gap (typically 3mm) between the antenna and the body to limit this detuning effect to an acceptable level, as described in Section 3.4 here.

Option (ii) is to be preferred here, as option (i) will require different sized antennas to be manufactured; each specific to the on-body characteristics of individual users or, more likely, to different sub-sets of similar users.

In, the *near*-term, the severe antenna *efficiency reduction* due to the nearby body can be addressed by accepting it in this short-range application and resorting to a combination of techniques, such as diversity schemes and/or increased transmit powers, to compensate for it. An in-depth investigation of this approach is reported here in Chapter 5.

2.3.2 Possible *Longer* Term Measures to Address Effects of Nearby Body More Effectively

In the *longer*-term both the detuning and efficiency loss deficiencies might be avoided by investigating insertion of a thin planar sheet of shielding material between the (otherwise *un*shielded) antenna and the body to largely decouple them electrically.

No work was conducted by the present author on this concept, but references to work by other authors are briefly outlined below.

2.3.2.1 Use of a Conventional (PEC) Shield

Reference [30] indicates that a conventional reflecting ground-plane, acting as a nominally Perfect Electric Conductor (PEC) shield, ideally requires ($\lambda/4$) separation between this plane and the antenna. Coupled with the π phase change which occurs upon reflection from a PEC surface, this ($\lambda/4$) separation ensures that the direct and reflected signals combine in-phase on boresight in the Far-Field.

In fact, smaller separations will still give combinations that combine *largely* in-phase (i.e. constructively). Nonetheless, since ($\lambda/4$) = 30mm at 2.4GHz, this otherwise simple and cheap PEC shield option would give rise to a decidedly non low-profile overall antenna solution, which would be unfeasible for use in the present Telecare/Telemedicine application.

2.3.2.2 Potential Benefits of More Exotic Types of Intervening Planes

In contrast, reference [31] indicates that some artificial planar materials/structures can be made to reflect incident electromagnetic waves with *zero* phase change. Examples here include Perfect Magnetic Conductors (PMC) and Electromagnetic Band Gap (EBG) surfaces which can give *zero* phase change over a relatively narrow frequency band.

On account of this *zero* phase change, the separation between the artificial planar shield and antenna can now be <<($\lambda/4$), thereby affording a low profile antenna solution as desired.

References [32] to [44] describe practical examples of how such PMC and EBG surfaces can be realised.

2.4 Existing Literature on Mutual Coupling between Two Adjacent *Un*shielded Antenna Elements when Located On-Body

The mutual coupling reduction effect observed between a pair of ‘Rufa’ antennas when on-body was reported by the current author at EuCAP 2011 reference [20] and was initially believed to be a novel finding. This reference is also cited in reference [46] by its author. However, subsequently, an earlier reference [19] describing this reduced mutual coupling effect for a pair of parallel dipole elements located directly above a dielectric slab was found. So, this result reported in reference [20] is not in fact novel, but instead constitutes a useful independent confirmation of [19].

No mechanism for this effect is given in [19], although [45] suggests that propagation by Surface Wave means may be responsible.

The reduction in mutual coupling reported in [20] by the author at EuCAP 2011, was subsequently cited in [46]. [46] concluded by suggesting that this reduction might potentially be of benefit for use it *compact* mobile handsets, having *multiple-antennas* to obtain capacity enhancements using MIMO techniques, for a given handset size.

Since the close proximity of the human body is known to have a considerable effect on an individual element's RF performance, literature concerning previous work on the effect of the human body on *multiple* element techniques was also reviewed in case, at some stage, an architecture with multiple onbody elements were proposed for use.

Although, primarily directed towards Body Area Networks (BANs), in which all the nodes are located on the same body, the results given in reference [19] are relevant here regarding coupling between possible multiple on-body elements within an on-body to off-body wireless link. Reference [19] describes modeling and measurements at 2.4GHz of the coupling (S_{21}) between two basic wire-type dipole antenna elements, when both are located above a *single* layer dielectric slab representing a specific type of body tissue. This assumes a semi-empirical formula based on the Friis formula in Free-Space for the coupling, which in dB terms takes the form:

$$|S_{21}(d,h)|_{dB} = P_0(h)|_{dB} - \eta(h) \, . \, 10 \, . \, \log_{10}(d/d_0) \qquad (2.1)$$

where;

d = inter-element separation [mm], and
h = the dipole antennas' height above the single dielectric slab.

$P_0(h)$ is the reference coupling experienced at a reference separation (d_0 = 400mm, here), and $\eta(h)$ here is the (so-called) path-loss exponent, which equals 2 in free-space. As might be expected, the notation above indicates that the reference coupling (P_0) and path-loss exponent (η) are both dependent on the height (h) of the antenna above the dielectric slab.

Simulations and measurements of S_{21} at 2.4GHz are reported for inter-element separations and heights above the dielectric slab of:

$100\text{mm} \le d \le 400\text{mm}$, and
$5\text{mm} \le h \le 50\text{mm}$.

Acceptable agreement between simulations and measurements was obtained in this reference when h = 10mm, which confirmed the validity of the models used. This enabled the h-dependence of η and P_0 to be investigated by means of the simulations for two different tissue types, with appropriate values of conductivity and permittivity.

This investigation revealed that $|S_{2,1}|$dB is strongly dependent on antenna height (h), and decreases as the antennas approach the dielectric slab (i.e. h decreases). By way of example, $|S_{21}|$ = -28dB for h = 5mm, and d = 100mm. Unfortunately, investigations at closer separations, for example ($d \leq 3$mm) which would have been of particular interest for the present study, are not reported in reference [19].

It is noted that the ranges of d and h investigated in reference [19] are both quite a bit larger than in the simulations conducted by the author (to be presented in Section 3.9 here) where:

$21\text{mm} \leq d \leq 63\text{mm}$, and
$h \leq 3\text{mm}$.

So, meaningful comparison of the absolute values of coupling in the two cases is not possible. Nonetheless, the general trends of ‘h’ and ‘d’ dependencies to be reported by the present author in section 3.9 here should probably be compatible with those observed in reference [19].

Reference [47] constitutes a more recent and in-depth version of reference [19]. Conclusions of this study, which includes more extensive measurements, further confirm the findings originally presented in [19].

2.5 Effect of Human Body on Multi-Element On-Body Antennas

References [27], [28] & [29] describe measurements of the effect on *capacity* of a MIMO architecture in which multiple antennas are located *on*-body in a Body Area Network (BAN). Here, it was found that MIMO capacity *in*creases as the separation between the on-body antennas *de*creases. This behaviour is contrary to that experienced in Wide Area Networks (WANs) and Wireless Local Area Networks (WLANs), where the antennas are located *off*-body. However, it is noted that, as expected, in both cases of on-body and off-body antenna location spatial correlation between elements still *in*creases as the inter-element separation *de*creases. Typical correlation coefficients of $\rho = 0.7$ & 0.4 are reported at separations of $d = 0.25\lambda_0$ & $0.4\lambda_0$ respectively between pairs of nearest-neighbour elements. At 2.4GHz here, these inter-element electrical separations correspond to physical separations of about 31 & 50mm respectively.

The difference in the MIMO capacity enhancement behaviour in the two cases is attributed to the effect of the body being in close proximity to the antennas in the BAN here. If confirmed by similar future work, *this effect is potentially advantageous for the proposed application* since it indicates that more MIMO capacity improvement could be realised as the proposed two-element *on-body* wireless sensor node is miniaturised. This is contrary to what might intuitively be expected.

By way of example, reference [48] reports that, for a (2x2) MIMO scheme with 20dB SNR, the measured capacity efficiency is (C/B) = 10.5 [bits/sec/Hz] for an inter-element separation of $d = 0.4\lambda_0$. Now, in the absence of MIMO, application of the Shannon Hartley Theorem (Equation (2.2) below) gives a capacity efficiency of (C/B) = 6.6 [bits/sec/Hz] for the basic reference SISO configuration with the same SNR = 20dB.

$$(C/B) = \log_2[1 + (S/N)] \tag{2.2}$$

So, the effect of the (2x2) on-body MIMO scheme is to provide a 1.6-fold capacity increase in this case. This improvement is slightly less than the maximum theoretical 2-fold expected for such a (2x2) MIMO configuration, when its antennas are used in an off-body free-space environment.

Further references regarding the effects of on-body antenna location for a pair of antennas are considered in more detail in section 3.9 here.

2.6 Depolarisation Effect for On-Body Antenna Element

During the course of routine pattern measurements of Antenova's (unshielded) 'Rufa' antenna, the present author noticed that its reasonably polarised pattern in Free-Space became almost completely depolarised when relocated to be on-body. This unanticipated observation is described in more detail in Section 3.5.1 here.

No previously published information could be found, relating to this effect, which was first reported by the present author at EuCAP 2011 [20]. It is therefore believed to be a genuinely novel finding.

Subsequently, a more detailed literature search was conducted in an attempt to provide a physical explanation of this phenomenon. This revealed one reference [50], which describes different Surface Wave (SW) characteristics for propagation in orthogonal directions at a dielectric interface. Initially, it was anticipated that this mechanism might be a potential physical explanation of the novel on-body depolarisation effect observed in a common plane.

However, upon further consideration it is now thought that this SW mechanism will give rise to different propagation in *orthogonal* planes, rather than different propagation for orthogonal polarisations in a *common* (azimuthal) plane. Consequently, it is no longer believed to be a candidate for the physical explanation of the observed on-body depolarisation effect.

Subsequently, the author conducted an analysis, based on the application of Geometric Optics at the air/body interface, which explained the observed depolarisation effect to good accuracy. This analysis is reported in full in Chapter 4 here, and is hoped will form the basis of a future IEEE AWPL publication.

2.7 Existing Literature on Multi-Element Antenna Schemes

The development of multi-element antenna schemes was originally driven by Third Generation (3G) cellular mobile wireless telephony; initially to provide diversity to mitigate fading, but more recently to increase/improve bandwidth efficiency in order to provide more capacity within the given channel bandwidths. However, the same general principles will also apply to the on-body wireless *sensor* links considered here.

Reference [51] describes diversity types, all involving multi-element antennas, to mitigate deep multipath fading. These include:

i) Spatial diversity,

ii) Polarisation diversity, and

iii) Pattern diversity.

Spatial diversity exploits the observation that fading in a multipath environment is *localised* to specific, relatively small, regions in space where the phases and amplitudes of the multiple received versions of the signals conspire to combine in a predominantly destructive fashion. So, provided two *reasonably separated* antenna elements are implemented, a destructive combination at both antenna elements simultaneously is much less likely than at either of the individual elements in isolation.

Polarisation diversity exploits the fact that orthogonally polarised transmit signals are reflected from objects in the environment with different relative amplitudes and phases. An extreme case of this is for Vertically Polarised (VP) and Horizontally Polarised (HP) signals at the Brewster angle near a dielectric interface. Thus, a destructive combination of multiple signals for one polarisation is unlikely to simultaneously give rise to an equally destructive combination of signals for its orthogonally polarised equivalent.

Pattern diversity relies on having two (or more) antenna elements with significantly different patterns and there being a distribution in arrival directions of different multipath signals within these patterns. A destructive combination of multipath components for one antenna pattern is unlikely to be replicated at a nearby antenna having a different antenna response to the same signals arriving from (almost) the same directions.

Finally several references, including [52] and [53], indicate that a combination or two or more diversity types is likely to be more effective than a single scheme in isolation. This is because the individual types are largely independent, so that it is far less likely that a deep fade will occur simultaneously for a combination of types. In this regard, the current author notes that two (otherwise identical) antenna elements, which are oriented to respond to orthogonally polarised components of the same multipath combination, are likely to have different patterns, unless the basic element pattern is truly isotropic. Thus, an antenna designed to provide polarisation diversity is also likely to have an inherent element of pattern diversity associated with it.

References [54] & [55] (and also [23] & [25]) include descriptions of three different associated processing/combining schemes used to realise diversity afforded by the provision of multiple antennas. These use the signals from each of the multiple elements, with its own associated receiver, to derive a more optimum signal with higher SNR from which the information can then be more reliably extracted. Such combining schemes include Selection Combining (SC), Maximum Ratio Combining (MRC) and Equal Ratio Combining (ERC):-

i) Selection Combining (SC). This is the simplest scheme, and has an RF switch which switches to the branch having the strongest signal (plus noise) level.

ii) Maximum Ratio Combining (MRC). Here, the signals from the individual branches are weighted, according to their individual SNR's, before being co-phased and then summed. This is the most complex scheme to implement.

iii) Equal Ratio Combining (ERC). This scheme is similar to MRC above, except that the weightings are all set to unity, before the co-phasing and summing. The resulting performance is only slightly inferior to the MRC scheme, but it is simpler to implement.

Finally, reference [56] describes a further diversity scheme, known as Feedback Combining, in which signals received at multiple antennas are sequentially switched to a *single* common receiver until one is found where the signal exceeds a certain predetermined threshold. The switch remains connected to this antenna until such time as the signal falls below the threshold when rescanning is resumed. The performance of this Feedback Combining scheme is only slightly inferior to the Selection Combining scheme, but the single receiver common to all the antennas leads to less implementation complexity.

Reference [56] states that diversity techniques are a relatively low cost but powerful means to improve wireless link performances in multipath rich environments. Also, unlike equalisation techniques, which overcome multipath fading by compensating for differential multipath delays, diversity techniques incur no data overhead penalty since they do not involve training sequences added to the basic information-bearing data.

Diversity relies on the random nature of wireless propagation and finds largely *un*correlated alternative signal paths to choose from for communication. So that, although one path may undergo a combination of signals leading to a deep fade, another may experience a different combination giving a strong signal. Hence, *instantaneous* and *average* SNRs can be improved by 20 to 30dB.

More theoretical studies on the reduction in communication link outages achieved by using different Multiple-Input Multiple-Output (MIMO) schemes have been conducted by many authors. For example, reference [56] considers M independent Rayleigh fading channels/branches, giving rise to deep and rapid amplitude fluctuations, with each channel/branch having the *same* average SNR = Γ.

Here, the probability that the *instantaneous* SNR in any individual Rayleigh fading channel will fall below a certain predetermined threshold value (γ) associated with an acceptable Bit Error Rate (BER) for the overall system is:

$$P\,(\gamma_1 \leq \gamma) = (1 - \exp(-\gamma/\Gamma)) \tag{2.3}$$

Hence, the probability that all M channels/branches will fall below the threshold, giving an overall system link outage, is:

$$P\,(\gamma_1,\gamma_2,\gamma_3 \ldots \gamma_M \leq \gamma) = (1 - \exp(-\gamma/\Gamma))^M \tag{2.4}$$

The significant improvement/reduction in link outage afforded by diversity techniques can be seen by evaluating equation (2.4) above for different numbers of branches (M). For example, if the instantaneous channel SNR (Γ) is 20dB, and the SNR threshold (γ) is 10dB for acceptable BER performance, then (γ/Γ) = 0.1, giving:

$$P\,(\gamma_1,\gamma_2,\gamma_3 \ldots \gamma_M \leq \gamma) = (1 - \exp(-0.1))^M \tag{2.5}$$

Thus, for a basic SISO link *without* diversity (i.e. M = 1)

$$P(\gamma_1, \gamma_2, \gamma_3 \ldots \gamma_M \leq \gamma) = (1 - \exp(-0.1)) = 0.095 \text{ (i.e. < 10\% outage)}$$

With simple diversity, having M = 2 branches:

$$P(\gamma_1, \gamma_2, \gamma_3 \ldots \gamma_M \leq \gamma) = (1 - \exp(-0.1))^2 = 0.0090 \text{ (i.e. < 1\% outage)}$$

With more complex diversity, having M = 4 branches:

$$P(\gamma_1, \gamma_2, \gamma_3 \ldots \gamma_M \leq \gamma) = (1 - \exp(-0.1))^4 = 0.000082 \text{ (i.e. < 0.01\% outage).}$$

Thus, for $(\gamma/\Gamma) = 0.1$, even a simple 2-branch diversity scheme gives a valuable 10-fold reduction in system outage from 10% in the absence of diversity to 1% with diversity. The 1000-fold improvement afforded by the 4-branch diversity scheme is even more marked, but can only be realised at the cost of significantly increased complexity.

It is noted that the analysis above makes no reference to the type of diversity scheme involved (e.g. spatial, polarisation or pattern diversity), but is likely to be generic to all diversity types. Also, it does not specify the environment in which the antennas are located. Instead, it merely assumes that the M branches involved are *independent*. However, the extent to which this is true will depend strongly on the antennas' environment. So, the correlation between signals in the individual channels/branches in the specific environment of their application is of key importance if the diversity scheme is to yield the outage improvements calculated above. As a result, the values above represent the *ideal* improvements, which will be degraded in practice according to the actual correlation present between the channels/branches.

Reference [53] is useful, as it gives some typical performance improvements experienced in practice with real systems. For instance, it states that, in practice, for *spatial* diversity with Maximal Ratio Combining (MRC), inter element spacings (d) of:

$$0.17\lambda_0 \leq d \leq 0.38\lambda_0$$

have been used. In particular, typically 1.5dB diversity gain is realised at the $0.17\lambda_0$ minimum inter element separation and 3dB at $0.38\lambda_0$. As will be seen later in section 3.9, the present author has modeled the effect of coupling (and hence correlation present) between two adjacent 'Rufa'™ elements in a twin element antenna on their inter-element spacing over a similar range of:

$$0.165\lambda_0 \leq d \leq 0.50\lambda_0$$

This was carried out for the twin-element antenna located both on-body and off-body to determine the effect that the proximity of the body has on the independence of the two channels/branches involved for the (1×2) SIMO *spatial* diversity scheme modeled here.

As regards, *polarisation* diversity, reference [53] states that the two antenna elements should be orthogonally polarised, so that two identical elements must be physically rotated by 90° with respect to each other. It also states that the distance between antennas is not critical here. Instead, it is more important that the cross-polar component of the individual antenna patterns be low, so that the degree to which the signals arriving at the orthogonally polarised antennas signals are decorrelated is maintained. Thus, a polarisation diversity scheme having two co-located orthogonally polarised on-body transmit antennas might only be marginally *bigger* than an alternative scheme with only a single on-body transmit antenna and therefore no diversity-gain.

Reference [53] also mentions that for *pattern* diversity (also referred to as beam diversity) the distance between the antenna elements is not so critical. Rather, the correlation between the radiation patterns of the elements is much more important here.

As mentioned earlier, reference [53] also mentions that no individual diversity type offers a perfect diversity solution. Instead, a combination of several types is usually employed in practice. The most important factor is the inherent decorrelation due to the different propagation channels/branches. Thereafter, any coupling introduced by the antennas will degrade this decorrelation, so it is important that coupling between elements in the multi element antenna is kept low to limit such degradation.

In this regard, reference [53] indicates that typical inter-element coupling should be less than -15dB, so that only 2.5% of signal power from one antenna element is transmitted from one antenna element to its nearest neighbour. In this regard, three inter-element coupling mechanisms are mentioned:

i) current coupling,

ii) free-space coupling via the elements' near-field, and

iii) Surface-Wave coupling in which electromagnetic energy is transported between the antenna ground-plane and air interface dielectric.

Taking steps to minimise these coupling mechanisms would have the following benefits:

i) evidently, it reduces the degrading effect on diversity improvement,

ii) it may allow antennas to be more closely spaced for a given level of diversity degradation; thereby allowing potential antenna miniaturisation, and

iii) finally, it may provide increased flexibility when trying to distribute the various components including antennas within a confined space.

However, if these individual benefits are exploited to the full, then it is likely that they will be mutually exclusive.

Finally, regarding the use of multi-element antennas to provide diversity, additional useful references consulted include [56], [57] and [58].

2.8 Candidate Wireless Link Architectures and Selection for the Proposed Study

2.8.1 Introduction

There are many different wireless link architectures that could be considered for wireless transmission of data from the on-body sensor to an off-body Access Point in Telecare/Telemedicine applications.

Therefore, this chapter first considers the most basic architectural consideration; namely network topology. Of particular interest in the present Telecare/Telemedicine application is the choice between a complex multi-node networked scheme and a much simpler scheme having dedicated individual links between each pair of on-body sensor and off-body Access Point nodes of interest (as indicated earlier in Figure 1.1).

Having selected the simpler non-networked option, with dedicated links between each on-body sensor and off-body Access Point node-pair, as the more appropriate scheme here, the different multi antenna architectures that this scheme might employ are then considered to arrive at the final candidate architecture for more detailed study here.

2.8.2 Networked Scheme versus Multiple Dedicated Links

Many extensive wireless sensor networks (WSN) [60] and [61] exist which take advantage of the presence of their multiple sensor nodes to exploit relaying of their sensor information in multiple shorter hops between sensor node-pairs having particularly opportune propagation characteristics, until it finally arrives at the desired destination node. Therefore, this mode of operation constitutes a networked scheme.

Neighbouring nodes in such a networked scheme are more likely to be in near Line of Sight (LOS) of each other, which makes them less likely to experience poor propagation that might otherwise be the case for the direct (possibly non LOS (NLOS)) route between the original source and final destination nodes.

For example, this could circumvent the potential propagation difficulty otherwise involved when the dispositions of the nodes are such that the body happens to be located directly between a particular on-body sensor node and associated Access Point node between which communication is required.

This multiple short hopping process is specified for the peer-to-peer mode in the IEEE 802.15.4 standard, as outlined in [8] and detailed in [9], which enables the most advantageous route to be exploited, in terms of favourable propagation.

Disadvantages of this *networked* approach include:

i) It *relies* on there being at least two on-body sensor nodes or two Access Point nodes present. Evidently these nodes must also be capable of operating in a relay capacity mode.

ii) This networked approach is a very much more complex scheme, involving a combination of different propagation means (both Radiation and Surface Wave between neighbouring on-body nodes) at the PHY layer. However, at the higher layers, where the structure of the ad-hoc network is established, hardware devices already exist constructed to implement standard protocols.

Features of the alternative *non*-networked approach, comprising a multiplicity of dedicated non-relaying, links between each on-body/off-body node-pair of interest, include:

i) It does *not* require the presence of *multiple* on-body sensor nodes and there is no need for them to be capable of acting in peer-to-peer relay mode,
ii) It is a very much simpler approach at both the PHY and higher layers,
iii) However, plainly it cannot take advantage of the more optimum route that might otherwise be available in its equivalent networked counterpart.

Regarding the choice between a networked and non-networked approach, it is noted that the number of nodes associated with an individual client/patient in the Telecare/Telemedicine applications here is likely to be limited in their initial guise. Indeed, for the majority of patient/clients, whose needs are relatively basic, a single on-body sensor node may well suffice.

Therefore, on these grounds it would be unwise to assume that an adequate number of nodes will be present (and available) in these applications to *guarantee* viable operation on a networked basis.

Hence, at this stage, only dedicated single hop links between each on-body sensor node and its off-body Access Point node were considered further. As a result, the wireless links between these node-pairs must be designed to ensure that they *can* communicate adequately.

However, should multiple on-body nodes eventually become the norm, migration from the proposed non-networked to a networked scheme could occur by adopting the networks and protocols emerging for more extensive WSNs. Evidently, this would then allow the considerable advantage of peer to peer inter node communication to be exploited.

2.8.3 Candidate Architectures for a Non-Networked Scheme

Four candidate link architectures, involving single dedicated links between source and destination nodes, having different numbers of antennas were considered as described in reference [23].

These are given in order of increasing complexity below and addressed in turn in the sub-sections following:

i. a basic Single Input Single Output (SISO) antenna architecture,
ii. an intermediate Multiple Input Single Output (MISO) antenna architecture,
iii. an intermediate Single Input Multiple Output (SIMO) antenna architecture, and
iv. a complex Multiple Input Multiple Output (MIMO) antenna architecture.

Although an uplink for transmissions of sensor data from each on-body wireless-equipped sensor node to the off-body node at the Access Point (AP) is of primary concern here, an associated downlink, involving information flow in the reverse direction, is also likely to be involved.

For example, such a downlink could be used to request retransmissions of uplinked sensor data which had been found to be in error, by means of error detection encoding, upon reception at the off-body Access Point (AP). Alternatively, in response to received sensor data indicating a particular patient need, the downlink could be used to command an on-body device to administer an appropriate level of medication in a timely fashion. For example, such a scheme would be appropriate for diabetic patients to detect and take autonomous remedial measures to address high blood/sugar levels in a real-time manner.

Suffice to say, that the fundamental principle of reciprocity at the Physical Layer (PHY) can be invoked here, so that investigations primarily directed toward the uplink here will be equally applicable on the equivalent downlink.

2.8.3.1 Basic Single Input Single Output (SISO) Antenna Configuration

As illustrated in Figure 2.1, this basic SISO scheme comprises a single element antenna located on the patient’s body and a single element antenna at the off-body Access Point

(AP). Although unviable here, this most basic scheme serves as a useful *reference* case against which the performance of more sophisticated schemes can be compared.

It will be shown later in Chapter 5, this basic SISO scheme is unviable in the present application, as it affords no protection against the deepest (20dB) multipath fading typically experienced in the multipath-rich *indoor* Telecare/Telemedicine environment here. Consequently, it would give rise to loss of data for the duration of such fades (which for a motionless comatose client/patient *might* be indefinitely).

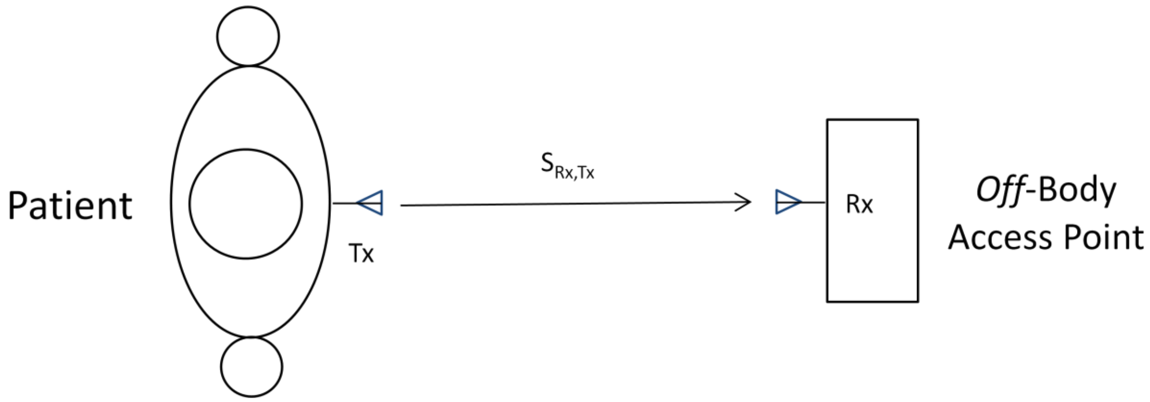

Figure 2.1: Basic Single Input Single Output (SISO) Data Link Architecture

Nonetheless it is included in the present study to serve as a reference against which the performance of more sophisticated architectures can be assessed

2.8.3.2 Multiple Input Single Output (MISO) Antenna Configuration

As illustrated in Figure 2.2, this MISO scheme comprises a multi-element antenna on the patient’s body and a single element antenna at the off-body Access Point (AP).

In practice, due to the requirement for minimum size at the on-body sensor node, a maximum of two on-body elements would be possible here as shown in Figure 2.2.

Nonetheless, even two such *on*-body elements here, should allow on-body spatial diversity, which, in principle, might be sufficient to mitigate the effect of deep fading.

However, for reasons of compactness for user acceptability, the separation between the two *on*-body elements antenna will be limited here for operation within the ISM band where $\lambda_0 \approx 120$mm, giving $0.5\lambda_0 \approx 60$mm and $0.2\lambda_0 \approx 24$mm.

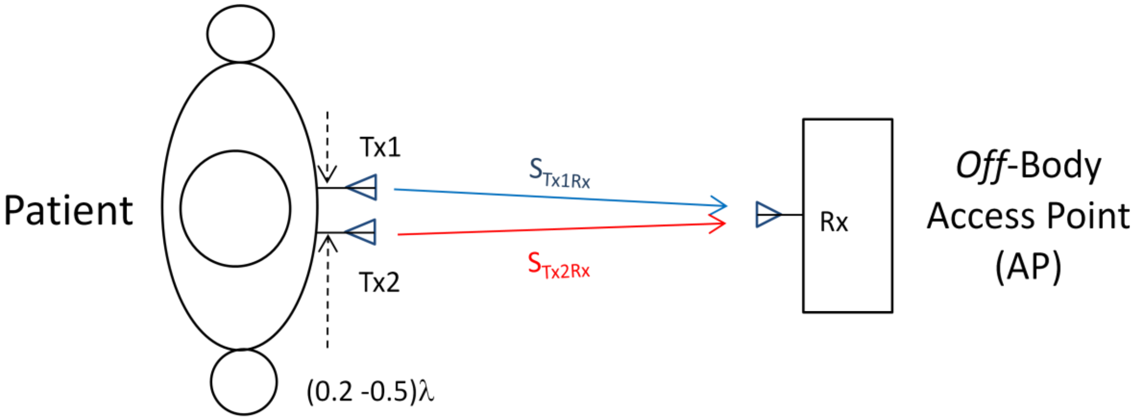

Figure 2.2: Multiple Input Single Output (MISO) Data Link Architecture

As a result, this would tend to limit the extent to which deep fading might be mitigated to a level that might not be useful in practice. This MISO architecture would also require diversity processing, of the types described previously in section 2.7 here, at the more numerous on-body nodes leading to a more complex overall system.

2.8.3.3 Single Input Multiple Output (SIMO) Antenna Configuration

As illustrated in Figure 2.3, this SIMO architecture comprises a single element antenna located on the patient’s body and a multi-element antenna at the off-body Access Point (AP).

Here, in contrast to its equivalent MISO scheme, the two elements in this SIMO scheme are located *off*-body, where compactness is less of a constraint, so that their separation can be larger. For example, at 2.4GHz, 1.0λ (~120mm) separation between the off-body antennas would be perfectly acceptable. As will be shown later in chapter 5, this affords typically 9dB spatial diversity gain that is extremely useful to mitigate all but the most extreme (and rare) fading.

A further practical advantage of this SIMO (as opposed to MISO) architecture is that the complexity of the twin element antenna and associated processing is located at the less numerous off-body Access Point(s), whilst the more numerous on-body nodes have a single element antenna, making them much simpler. As a result, the overall system complexity (and hence cost) of this SIMO configuration will be less than its MISO equivalent.

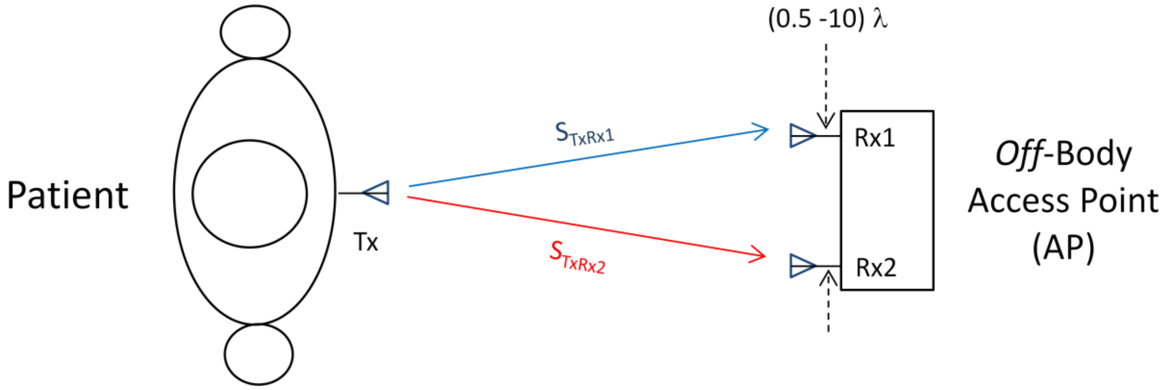

Figure 2.3: Single Input Multiple Output (SIMO) Data Link Architecture

2.8.3.4 Multiple Input Multiple Output (MIMO) Antenna Configuration

As illustrated in Figure 2.4, this scheme comprises a multi element antenna on the patient's body as well as a multi element antenna at the off-body Access Point (AP). As mentioned in reference [23], such a MIMO scheme can enhance link capacity here without requiring any increase in its RF spectral occupancy.

This could be useful if, as a result of successful exploitation of links employing a simpler SIMO scheme, a modest increase in the original data-rate, which would otherwise overcrowd the already congested ISM band at 2.4GHz, was later found to be required. Such a requirement is in keeping with the trend of increased data rates already experienced in successful wireless mobile communications (including 4G cellular systems currently being deployed).

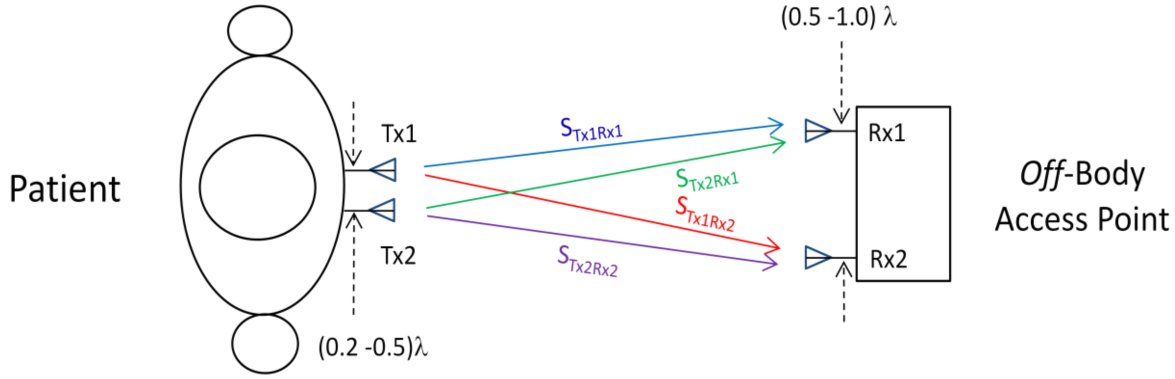

Figure 2.4: Multiple Input Multiple Output (MIMO) Data Link Architecture

However, as discussed earlier, because of stringent space constraints here, two elements at most are permissible on-body. Now, the potential MIMO capacity enhancement is determined by the minimum of the number of antenna elements at either ends of the link [63]. As a result, therefore, since a maximum of only two *on*-body antenna elements are permissible anyway at the space constrained *on*-body end of the link in the present application, there would be little point in increasing the number of *off*-body antenna elements beyond two. Thus, for possible next generation on-body sensor applications, only the simplest (2x2) element MIMO scheme, as shown in Figure 2.4, is likely to be feasible. Potentially, this architecture *could* double the basic link capacity, should this be required.

However, in practice, the capacity enhancement actually realised will depend on whether sufficient decorrelation exists between signals at these twin element antennas, so that the potential capacity doubling will only be achieved for reasonably *un*correlated signals.

Further, in this regard, any significant mutual coupling between these elements will increase correlation, thereby degrading decorrelation, otherwise present between the two spatially separated elements. It is, therefore, particularly important to investigate the mutual coupling between element pairs at the *on*-body end of the link, where these need to be more closely spaced. In this regard, interesting simulations and measurements of mutual coupling between spatially separated on-body element-pairs are reported later in section 3.9 here.

Additional references consulted regarding MIMO techniques include [64] and [65]. These describe the effects of RF channel characteristics on MIMO performance and how to simulate and emulate them.

2.8.4 Antenna Configuration Adopted for the Proposed Study

In the near-term, this study is looking to *multi*-element antenna architectures primarily to mitigate fading by means of diversity. In the absence of such diversity techniques, the basic SISO scheme would give *un*acceptable performance on account of deep (20dB) multipath fading, which could only be mitigated by undesirable large increases in transmit power. Doing this would greatly reduce lifetimes of batteries necessary to power these mobile *on*-body wireless sensor nodes.

Since diversity techniques only require a multi-element antenna at one end of the link, it makes sense from both a low-cost and user convenience point of view to locate this multi-element antenna at the less numerous and less space constrained off-body Access Points (rather than the more numerous and highly compact on-body nodes). Hence, a SIMO architecture is proposed as best suited to the Telecare/Telemedicine applications considered here.

A natural evolution for next generation applications might involve a more complex (2x2) MIMO architecture, having two on-body antenna elements as well as the two off-body antenna elements. This scheme could potentially double the current SIMO link capacity, provided there is sufficient decorrelation between signals in the various branches within this architecture.

Finally, a further justification of adopting a SIMO rather than MISO scheme is that, in almost all applications, diversity decisions are made at the receive end of the link and are unknown to the transmit end. Thus, for the application here, where on-body wireless-equipped sensors are primarily transmitting their information to Access Points (APs) for remote monitoring, the multiple antennas and diversity decisions will be required at these off-body APs. As a result, the more numerous on-body wireless sensor nodes will be simpler and likely to be smaller. Therefore, besides the advantage of more compact on-body devices, this arrangement also has the key advantage of a lower overall system complexity and hence cost.

In conclusion, therefore, a non-networked scheme, with individual links having a SIMO architecture, involving an *on*-body wireless sensor node with a *single* element antenna and an *off*-body wireless node with *two* antenna elements, was considered to be the most appropriate choice for further study here.

2.9 Functional Outline of Key Software Packages Used Here

Apart from relatively straightforward user written MATLAB and EXCEL programme to aid analysis and plots, this study also involved extensive use of the more sophisticated CST (Computer Software Technology) MICROWAVE STUDIO® and Remcom's Wireless InSite (WI) software packages.

Accordingly, an outline of the basic functioning of these two software packages is included below.

2.9.1 Functional Outline of CST Software Package

A key part of the study here has involved the use of the CST (Computer Software Technology) MICROWAVE STUDIO® software package to determine the RF performance of the 'Rufa' candidate COTS antenna in its immediate surroundings. The close proximity of human body is of particular interest here.

Two references are particularly relevant. Reference [66] addresses the question 'What is CST MICROWAVE STUDIO®?' in more general non-mathematical terms. To complement this, reference [67] provides a more mathematical description of the Finite Element Method (FEM) included within this package and used in the present application. Other useful references on this topic include [68], [69] and [70].

Extensive experience of many users, including those at QMUL, has shown that CST MICROWAVE STUDIO® is a comprehensive software tool that is considered to be relatively user-friendly.

Reference [66] describes CST MICROWAVE STUDIO® as a 'powerful software tool for electromagnetic analysis in the high frequency range' (such as a few GHz in the present application). It provides an effective 3-D graphics front end to generate an accurate mathematical representation of the physical structure whose RF characteristics are to be determined. Alternatively, it also allows the antenna geometry to be imported from a CAD file, although this facility was not used here.

It includes a wide variety of solver methods, operating in the temporal or frequency domains, with different mesh grid geometries. This allows it to operate in a wide variety of applications. However, to best suit the narrowband, electrically small ($<\lambda$) and fairly detailed antenna and its immediate surroundings of interest here, modeling in the frequency domain, using the Finite Element Method (FEM) with tetrahedral mesh grid geometries, was used.

Reference [67] describes the five stages within the FEM process used here, which include:

i) Segmentation or Meshing Geometry. This divides the total system under investigation into a large number (N-1) of adjoining smaller elements, which combine at N meeting points (nodes) to give a close approximation to the total structure. Commonly used finite element types (and also implemented in CST) include tetrahedrons (pyramidal shapes, having 4 sides) and hexahedrons (brick shapes, with 6 sides). These individual elements must only contain a homogenous material (i.e. elements cannot cross boundaries between material types having different RF characteristics)

ii) Derivation of matrices, describing Maxwell's Equations, for individual elements within the total structure.

iii) Assembly of all these individual element matrices into a system matrix, which describes the total system.

iv) Solution of this system matrix to give the approximate total field-potential distribution (ϕ) and currents flowing on the conducting portions of the device. Reference [68] indicates that formulation in the frequency domain typically comprises a large system of linear equations, and a matrix inversion technique is commonly used to obtain the solution at a specific frequency.

v) Post-processing of this field-potential distribution (ϕ) and currents flowing on the conducting portions to derive the RF properties, such as S-parameters, and far-field patterns of the device.

The side-lengths of the individual tetrahedral elements, and hence their specific geometries, used within the mesh structure are optimised in an iterative fashion, until:

a) The combined mesh structure accurately reflects the geometry of the total structure.

b) The individual element aspect-ratios are not too extreme, so that accurate solutions can be obtained relatively rapidly; in particular, long and thin tetrahedral are to be avoided in this respect, and finally

c) Changes (ΔS) in the S-parameters in the solution, from one iteration to the next, consistently fall below a user-specified threshold level i.e. the solution has converged.

In the FEM used here, different FEM simulations are performed at preselected spot-frequencies covering the band of interest. Interpolation between these frequencies is used to identify regions where the solution changes in a particularly rapid fashion and consequently whether further solutions at additional frequencies are required to prevent potential under-sampling.

Reference [66] indicates that the CST software package also provides the facility to generate high-quality plots of the RF parameters, including far-field patterns, for documentation purposes. This data can also be exported in data file form for subsequent use by other programmes as desired. In this regard, it is noted here that the CST simulated 3-D pattern data of the candidate ‘Rufa’ antenna when used on-body was exported as a data-file for subsequent use in the Wireless InSite (WI) system model. In this case, for this purpose it was necessary to modify the exported data to remove its associated header data, to convert it into the format required by WI, before data transfer was performed.

2.9.2 Functional Outline of Wireless InSite Software Package

Another key aspect of the study here has been the use of Remcom’s Wireless InSite software package, which uses ray tracing techniques to simulate the overall *system*, to derive *system* performance aspects; in particular *diversity gain*.

A software approach, rather than extensive measurements, was taken for this, as this approach is more *systematic*, allowing the effect of varying individual parameters to be investigated in isolation. This provides some physical insight into the effects of the many individual parameters involved in the overall system performance.

Although an extensive series of measurements would have enabled the *overall* system performance to be derived with increased confidence, such an approach provides little insight into the functioning of the individual physical mechanisms involved, and so was not undertaken at this stage.

Therefore, since this Wireless InSite (WI) software tool plays such an important part in this study, it was thought appropriate to include a very brief outline of the Shooting Bouncing Ray (SBR) technique used within it.

The basic steps involved are described in detail in reference [71] and summarised in a webinar based on this in [72]. These include:

i) The user inputs physical details of the environment to be modeled, including dimensions and materials of objects located within it,

ii) Unless generic internally-specified antenna types are being used, the user also inputs details of the antenna type(s) being considered, in particular the gains in their 3-D patterns,

iii) WI then determines geometrical ray paths using a fast and robust ray tracing procedure (SBR). This is based on the physics of optical reflection and refraction,

iv) WI stores the geometrical paths obtained from the SBR ray-tracing procedure,

v) WI constructs the geometrical optics and edge-diffracted paths from the stored geometrical path database,

vi) WI evaluates E-fields using the Uniform Theory of Diffraction (UTD) and material-dependent reflection and transmission characteristics

vii) WI combines these E-fields with antenna pattern gain to derive path loss, delay, delay spread, angle of arrival, coverage areas, etc.

It is noted that reference [71] concerns propagation in an urban environment. However, upon contacting Remcom, it was determined that the basic SBR technique employed in Wireless InSite is used for all environment types, including the indoor environment studied here.

Further details concerning the precise mechanisms to implement these SBR techniques with maximum computational efficiency are, not unnaturally, proprietary and could not be disclosed. However, these are not particularly relevant here.

2.10 Summary

The initial (and ongoing) survey of published literature, including more commercially orientated technical publications, indicated that in the *near*-term a viable wireless communication link, to transport low data-rate sensor information between mobile on-body sensor node(s) and fixed off-body Access Points *might* be realised using existing COTS technology including the antennas. Link viability here involves a judicious compromise between generally conflicting considerations, including:

i) overall system affordability and

ii) user acceptability of on-body sensor nodes, as well as

iii) adequate link performance for the key medical information being conveyed.

However, the survey also showed that the use of such unshielded COTS antenna technology in close proximity to dielectric objects, such as the human body, poses considerable challenges; in particular, the nearby proximity of the body causes a drastic (typically 13dB) reduction in antenna efficiency.

Furthermore, published literature on propagation in a multipath-rich environment, such as the indoor environment envisaged in the present Telecare/Telemedicine application, indicated that severe (typically up to 20dB) multipath induced fading could be expected on occasions.

Clearly, the combined degradation due to this fading and the reduction in on-body antenna efficiency, could be offset by the simple means of increasing on-body transmit powers to restore a reasonable link performance. However, doing so would severely reduce the battery lifetimes in these battery powered on-body nodes. Thus, this basic Single Input Single Output (SISO) link architecture, although useful here as a baseline solution against which to compare other solutions, cannot be used in practice.

Fortunately, however, the survey also indicated that various candidate *multi* antenna architectures are available, which can provide sufficient diversity gain to partially mitigate the fading. Use of such a technique would allow much lower transmit powers to be used on-body, with more reasonable battery lifetimes and therefore less frequent replacement. After due consideration, the Single Input Multiple Output (SIMO) multi antenna candidate architecture, having a single antenna on-body and multiple output antennas at the off-body Access Point, was chosen as being best suited for the present application. This choice gives rise to the smallest and simplest on-body node, with attendant advantages of user acceptability and system provider affordability.

From the survey of the IEEE 802.15.4 standard for Wireless Personal Area Networks (WPANs) it was concluded that, in the *near*-term, a solution with dedicated links between sensor nodes and Access Point nodes was probably best suited to this stage. This simpler solution ensures that a reliable link can be assured for the least complex, but initially probably more numerous, cases where only a single wireless sensor node is being used.

However, the peer-to-peer mode in the IEEE 802.15.4 standard, providing relaying between adjacent wireless sensor nodes with its potential propagation advantages, could be exploited in future variants if and when multiple on-body sensor nodes are available for use in this capacity.

Finally, for *longer*-term application, more recent references indicate the development of artificial planar materials, having unusual reflection characteristics. It is suggested that these might be used as shields for (otherwise unshielded) COTS antennas, by locating thin sheets of these materials between the antennas and the body. The unusual reflection characteristics of these artificial planar materials would allow genuinely low profile on-body antennas; a feature which is precluded if conventional Perfect Electrical Conductor (PEC) shields are employed.

This concept, considered further in section 2.3.2 here, was greeted with considerable enthusiasm by an established antenna manufacturer, who is interested in developing on-body antennas for Telecare/Telemedicine applications, and a possible liaison to further explore this possibility has been pursued.

Chapter 3

Effect of Using ‘Rufa’ COTS Antenna in Close Proximity to Human Body

3.1 Introduction

One of the main aims of this study was to devise a *viable* system solution for use in the Telecare/Telemedicine application outlined earlier. Thus, to fulfill this aim, it was decided to determine whether it might be possible to leverage-off COTS technology, by using an existing Commercial off the Shelf (COTS) antenna, to exploit its small-size and low-cost attributes.

The conventional way to shield an (otherwise unshielded) antenna from the effect of a nearby lossy dielectric object, for example a human-body, is to locate a highly conductive surface between them at a distance of ($\lambda/4$) from the antenna. Unfortunately, at 2.4GHz where ($\lambda/4$) $\approx$ 30mm, this measure would drastically compromise the inherently low-profile nature of this COTS antenna. Therefore, because they cannot be shielded by conventional means, such antennas will inevitably suffer from detuning and loss of efficiency when used in close proximity to the human body. Evidently, if affordability and size were of little consequence here, then a larger, custom-built antenna with shielding would have been a better choice on purely technical grounds. However, small size and affordability are arguably the most essential requirements to be satisfied to ensure commercial viability of systems in the Telecare/Telemedical applications envisaged here.

Fortunately, provided certain remedial measures are taken, this chapter and system design considerations given later in chapter 5 will show that the detuning and loss of efficiency of existing unshielded COTS antennas can be reduced or mitigated to an extent that still permits adequate *system* performance.

This chapter starts, in sections 3.2 and 3.3, by outlining key aspects of the candidate COTS antenna, primarily designed for free-space use, which was selected for use on-body here. It then proceeds to describe measurements and simulations to determine the effect that a nearby human body, has on these aspects for a *single* candidate COTS antenna. These confirm some *anticipated* implications, but also uncovered an intriguing *un*anticipated effect, which has not been previously reported.

Sections 3.4 to 3.6 summarise the key effects (both *anticipated* and *un*anticipated) when a *single* candidate COTS antenna assembly is located in close proximity to the human body.

Section 3.7 describes the required format of the CST-simulated antenna pattern data for use within the subsequent Wireless Insite system simulations, described later in Chapter 5.

Section 3.8 then describes a brief investigation to determine how far the overall size of this already small antenna assembly might be further reduced to make it even more compatible with minimum size requirements for proposed onbody use.

Finally, section 3.9 considers another *un*anticipated effect observed when a *pair* of these COTS antennas is used closely spaced and located in close proximity to the human body.

3.2 Candidate COTS Antenna Used Here

The candidate COTS antenna reported here is a ‘Rufa’ ™ Antenna (part no. 5887) manufactured by ‘Antenova’. Its physical details, and RF performance in its originally intended free-space use, are given in its technical specification sheet [21] and a photograph of the complete unit is shown in Figure 3.1 overleaf. This includes a modified feed arrangement in which the original top-mounted SMA edge connector was replaced by a semi-rigid cable terminating in a female SMA connector (the PCB pads for the original SMA edge connector can also be seen here).

This ‘inverted-L’ type antenna, operating in the 2.4GHz band designated for Industrial, Scientific and Medical (ISM) band use, is mounted on a dielectric chip and measures only (15mm x 5mm x 1mm). This is to reduce its physical size for a given electrical size, and its size in relation to the SMA connector here indicates just how small this basic antenna *chip* is.

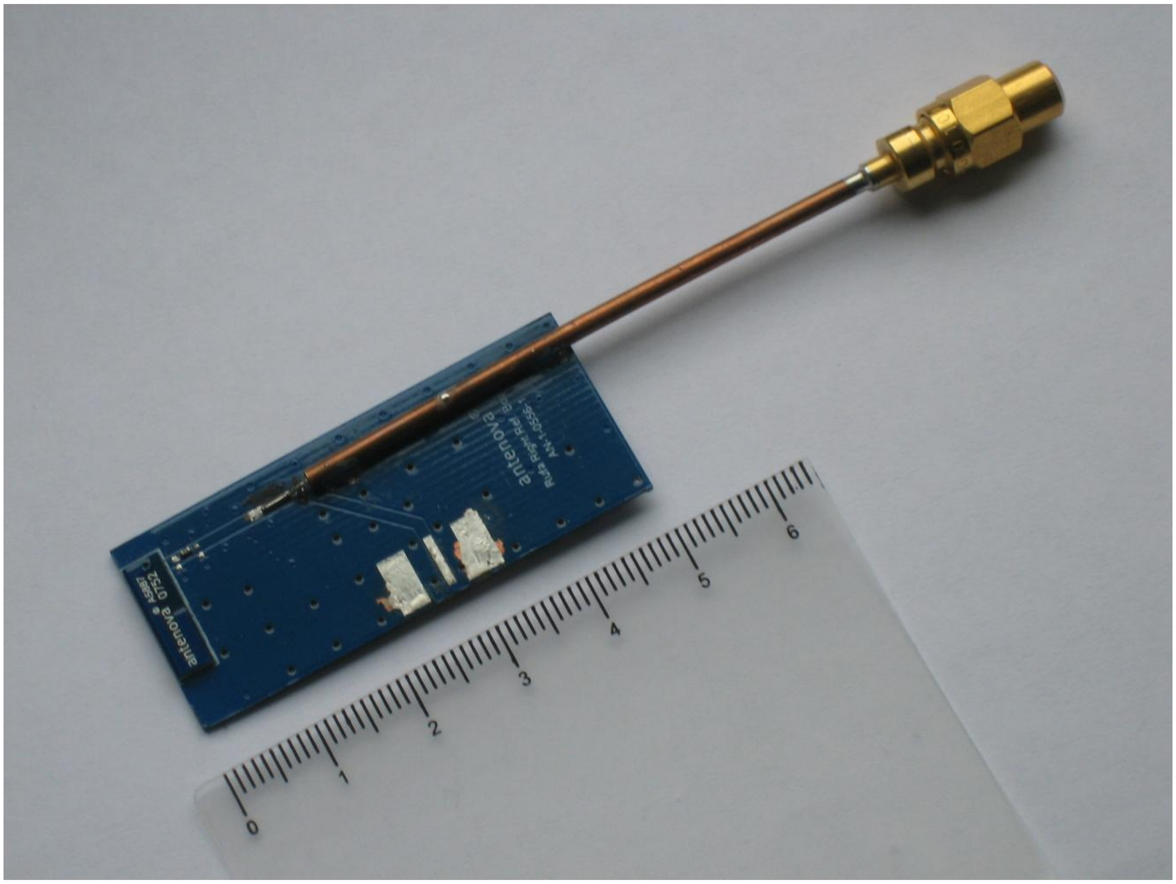

Figure 3.1: Photograph of an Antenova ‘Rufa’ COTS Antenna Assembly with modified feed comprising a semi-rigid cable terminating in a female SMA connector

However, to realise useful performance, this chip component must be used in conjunction with an associated Evaluation Board. This is a Printed Circuit Board (PCB), having a partial ground-plane (GND), which gives a much larger overall antenna size of (50mm x 21mm x 2mm). It is noted that, being partial, this ground-plane does not extend directly under the antenna chip itself, which remains largely unshielded from the influence of the nearby body in the proposed application.

Subject to certain restrictions in the immediate vicinity of the chip antenna, most of the area of this associated PCB with GND plane is vacant and can be used to mount additional components without adversely affecting the antenna's RF performance. Such components would include the components require to realise a complete wireless on-body sensor node; such as the sensor itself, an RF front-end Module (FEM) and associated digital circuitry.

In addition, if necessary for further miniaturisation, simulations presented in section 3.8 here indicate that the standard (50mm x 21mm) area of this associated PCB with GND plane can be halved, to (25mm x 21mm), without significantly degrading the COTS 'Rufa' antenna's RF performance. In a medical context, it is noted that this reduced area is significantly smaller than the contact area currently required to attach standard ECG probes to the body (42 mm diameter).

3.3 Investigating this Candidate COTS Antenna

Two samples of this 'Rufa' COTS antenna (part no. 5887) mounted on their associated evaluation boards were obtained for assessment. Initial investigative *measurements*, were conducted to characterise key RF performance parameters when located in free-space and on-body. These confirmed the anticipated detuning effect of the body.

However, experimentation during this preliminary measurement phase revealed that the extent of this detuning could be constrained to an acceptable level if the antenna was not touching the body *directly* but, instead, is located in close proximity to the body with a thin intervening air-gap. Because it is so thin (typically a few millimeters), the inclusion of this air-gap will not detract significantly from the antenna's existing low-profile format, as required for on-body use here.

The findings of these initial measurements were then further investigated by subsequent CST simulations. Patterns derived during these CST *simulations* also revealed, as anticipated, that the COTS antenna becomes very inefficient when in close proximity to the human body, being (~3%) on-body compared to (~70%) in free-space.

Results for these *anticipated* detuning and efficiency reduction effects are described in more detail in section 3.4 below.

However, of particular interest for the present study was that, during the course of these confirmatory investigations, two *un*anticipated effects of relocating the candidate antenna from its intended free-space environment to be on-body were discovered, namely:

i) when relocated to be on-body, the antenna patterns (which are reasonably polarised in free-space) become almost completely depolarised, and
ii) when on-body, the mutual coupling between a *pair* of these antennas is significantly reduced for a given inter-element separation when compared to that experienced in free-space.

Results of both measurements and simulations to quantify these *un*anticipated effects are described in more detail in sections 3.5 plus 3.6 and section 3.9 respectively. Representative onbody patterns are of particular significance, since these are needed for importing into the subsequent Wireless Insite simulations, described in Chapter 5, which quantify the effect on the *overall system* performance of the indoor Telecare/Telemedicine link here.

Finally, as described in section 3.8, the extent to which the existing PCB associated with this candidate antenna can be reduced, whilst still maintaining adequate RF performance, was investigated. This indicates the likely overall size to which the wireless sensor node might potentially be reduced, which might be useful for the present onbody applications.

3.4 *Anticipated* Effects of Human Body in Close Proximity to Unshielded Antenna

These were conducted to quantify the anticipated effects of the nearby body on the COTS ‘Rufa’ antenna and include its detuning effect and the reduction in its efficiency.

3.4.1 On-Body *Detuning* Effect

The dielectric nature of the body in close proximity to the candidate COTS antenna will increase its electrical size and hence lower its natural free-space resonant frequency.

If too extreme, this detuning would reduce the antenna’s resonant frequency to be below that designated for the 2.4GHz ISM-band, thereby rendering it unusable in the present on-body context. Therefore, preliminary *measurements* were made of the overall candidate antenna located at various points on the body to assess the likely extent of this effect.

3.4.1.1 Preliminary *Measurements* of On-body Detuning Effect

Measurements of S11 on this ‘Rufa’ antenna chip mounted on its associated Evaluation Board were conducted using an HP8720ES Vector Network Analyser (VNA). Figure 3.2 overleaf shows *measured* S11 versus frequency for this ‘Rufa’ antenna assembly for three different scenarios:

i) when located off-body (i.e. in free-space),

ii) when its evaluation board is located *directly* on skin on the author’s left-hand wrist and

iii) when located on the author’s left-hand wrist, but with one intervening cotton-wool pad of about 1mm thickness

The associated table 3.1 (also overleaf) lists key parameters derived from these S11 curves for these three scenarios.

In order to cover the complete 2.4GHz ISM-band allocation, the antenna element must have $f^{-10dB}_{lower} \leq 2.4000$GHz and $f^{-10dB}_{upper} \geq 2.4835$GHz. This corresponds to a centre frequency of $f_c = 2.4418$GHz with a -10dB bandwidth of $\Delta f^{-10dB} = 84$MHz.

Table 3.1 shows that when located *off*-body (blue curve in Figure 3.2) this ‘Rufa’ antenna assembly provides coverage from f^{-10dB}_{lower} = 2.384GHz to f^{-10dB}_{upper} = 2.549GHz, giving

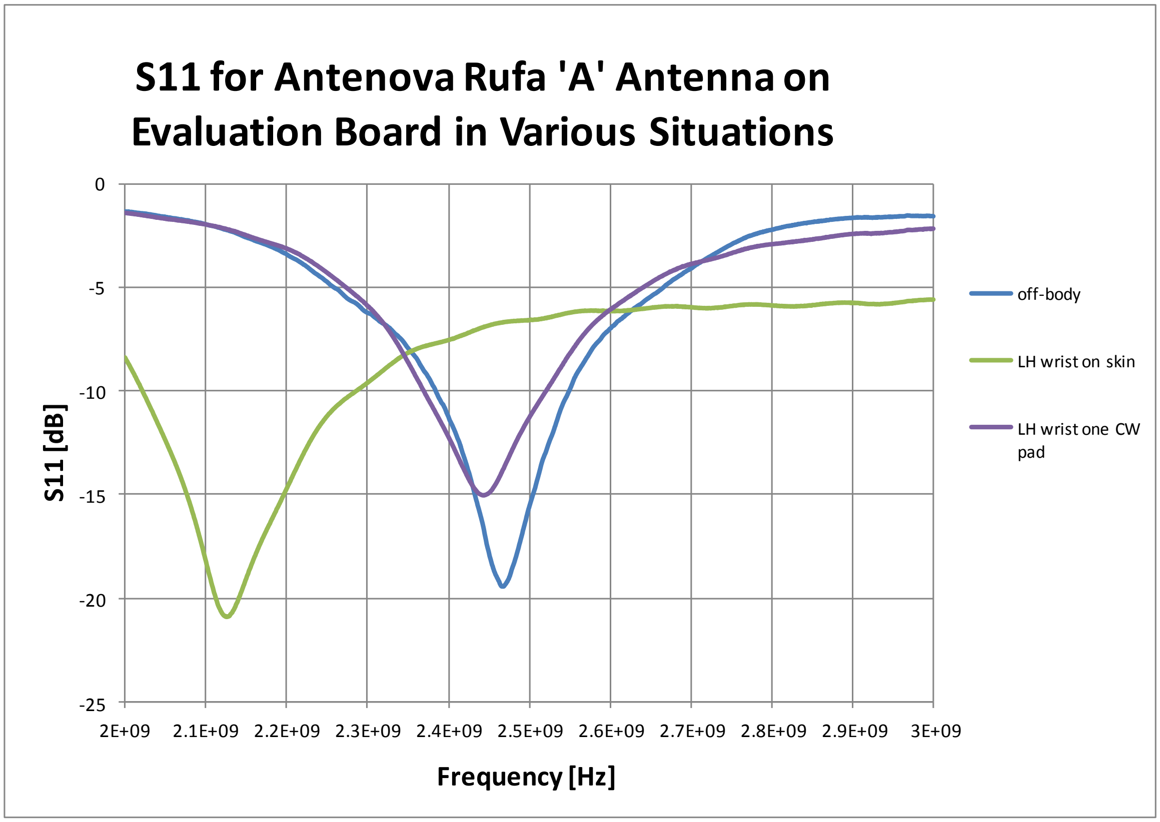

Figure 3.2: *Measured* S11 versus frequency for Antenova’s ‘Rufa’ COTS Antenna Assembly for Three Different Scenarios

165MHz at the -10dB level. Thus, in this *free-space* scenario, the ‘Rufa’ antenna assembly provides *more than adequate* coverage for the complete 2.4GHz ISM band. Table 3.1 also shows that when the antenna assembly was located *directly* on the author’s left-hand wrist (green curve in Figure 3.2) the proximity of the body significantly reduces its resonant frequency, so that it no longer covers the required 2.4000GHz to 2.4835GHz range for the ISM band. This initial result would have proven this COTS ‘Rufa’ antenna to be useless for the *on*-body application envisaged here.

Fortunately, however, another scenario (purple curve in Figure 3.2) was also investigated. This is the same as in the previous scenario (green curve) except that one intervening cotton-wool pad, of about 1mm thickness, is now included between the author’s wrist and the antenna assembly. This minor modification largely restores the antenna's original resonant

'Rufa' Antenna Location	f^{-10dB}_{lower}	f^{-10dB}_{upper}	f_c	Δf^{-10dB}
	[GHz]	[GHz]	[GHz]	[MHz]
Off-body/Free Space	2.384	2.549	2.467	165
LH wrist directly on skin	2.022	2.287	2.155	265
LH wrist with one intervening cotton-wool pad	2.370	2.521	2.446	151
ISM band allocation	2.400	2.484	2.442	84

Table 3.1: Key *Measured* S11 Parameters Extracted from those in Figure 3.2 for Antenova's 'Rufa' COTS Antenna Located in Free Space and Two Different On-Body Scenarios

frequency, so that it now covers the band from f^{-10dB}_{lower} = 2.370GHz to f^{-10dB}_{upper} = 2.521GHz, which corresponds to a centre frequency of f_c = 2.446GHz and a -10dB bandwidth of Δf^{-10dB} = 151MHz. Although slightly less than the 185MHz measured in free-space, this frequency span is still sufficient to ensure that the 'Rufa' COTS antenna still covers the 2.4000GHz to 2.4835GHz range required for the ISM-band.

It is noted that this minor modification to provide a small air-gap between the body and the antenna to restore its RF performance, will only slightly increase the height of such a wireless on-body sensor. Further, it is also possible that, should they need to be reusable to further minimise cost, then such on-body sensors are unlikely to be allowed in *direct* contact with the body anyway for hygiene reasons. Regardless of the reason, the small air-gap required will not significantly detract from the low profile requirement for such wireless equipped on-body sensors.

In conclusion, therefore, these preliminary *measurements* show that detuning can be reduced to acceptable level by locating this antenna to be slightly off-body and, as a result, the use of the 'Rufa' COTS antenna here still remains a viable potential candidate for this on-body application.

3.4.1.2 In Depth *Simulations*

These encouraging preliminary *measured* results motivated the development of an equivalent CST *simulation* model of this antenna assembly. This was initially modeled in *free-space* to provide a reference case.

This *simulation* approach was adopted as the most appropriate at this stage for two reasons:

i) it provides a systematic means to investigate the dependence of S11 as the size of the body and the separation between the antenna assembly and the body are varied, and

ii) other, equally important, far field RF parameters, including antenna patterns and efficiencies, can be more readily investigated for the antenna in proximity to the body. In this respect, it is noted that the antenna's specification sheet only quotes far-field parameters in free-space conditions.

Thus, detailed internal dimensions of the 'Rufa' antenna, and its associated Evaluation Board were obtained from Antenova to enable it to be accurately modeled. The CST model of this overall assembly and internal structure of metallic components within the antenna chip itself are shown overleaf in Figures 3.3 and 3.4. These depict this antenna in the absence of a nearby human body i.e. in its intended free-space (reference) environment. The strip-line feed arrangement in this model is not identical to that in the photograph of the actual antenna shown in Figure 3.1, whose input/output is to the long side of the board via an SMA RF connector. However, this slight difference is not expected to significantly affect the results reported here. Further, should multiple closely spaced elements be required on body, such 'side' exits would be precluded on grounds of compactness.

Finally, for compatibility with the 'Rufa' antenna hardware sample, the Evaluation Board assumed in the *simulations* here is a double-sided Printed Circuit Board (PCB) of

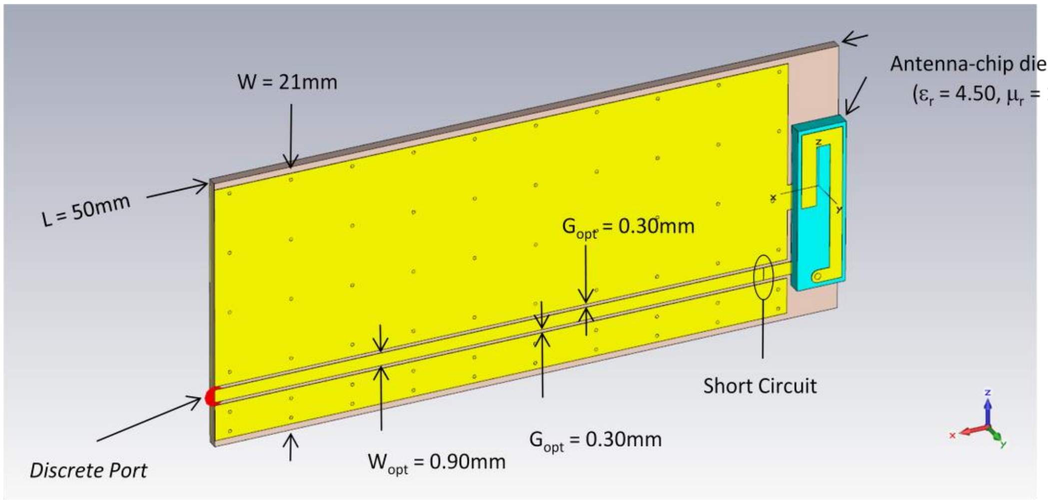

C:\programme files\cst studio suite 2009\wdw_cst_designs\antenova_rufa_antenna\trial14_sc_feed-line_discrete-port.cst

Figure 3.3: CST *Simulation* Model of Antenova's 'Rufa' COTS Antenna Assembly in *Free-Space* scenario

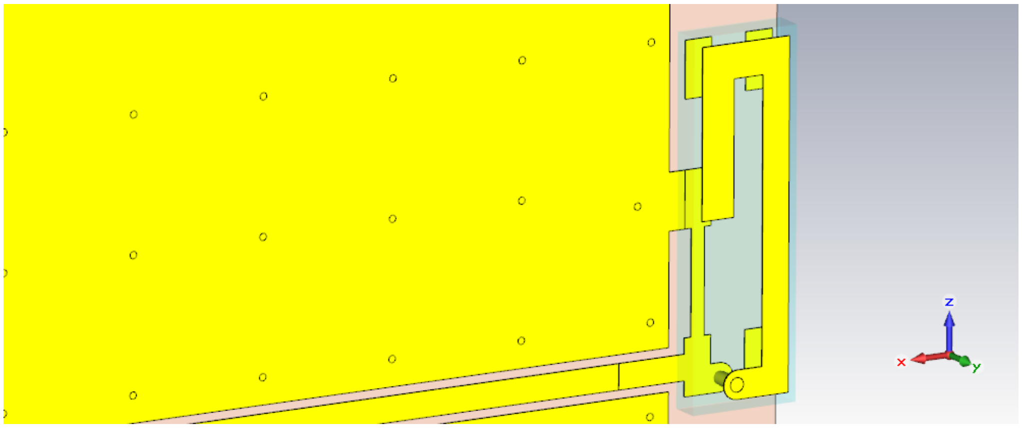

Figure 3.4: Showing More Detail of the Metallic Components within the Antenna Chip (in Yellow)

inexpensive 'FR4' material ($\varepsilon_r = 2.7$, $\mu_r = 1.0$, $\tan\delta = 0.025$). As can be seen in Figures 3.3 and 3.4, this has multiple vias connecting the two ground-planes on either side of the board.

3.4.1.2.1 *Free Space* Simulations - Initial Results

An initial simulated result is given in Figure 3.5 below for this 'Rufa' antenna assembly when in its reference *free-space* environment.

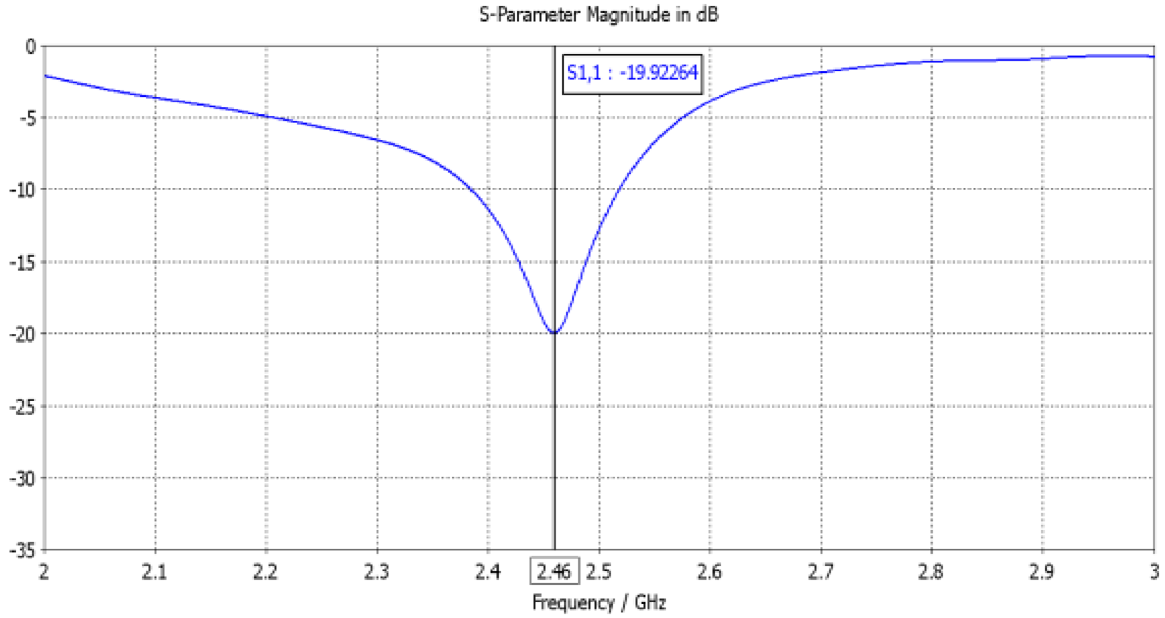

Figure 3.5: *Simulated* S11 versus frequency for Antenova's 'Rufa' COTS Antenna in FREE-SPACE Scenario.

This shows S11 versus frequency in the 2.0 to 3.0GHz band, and it can be seen that the *simulated* 'Rufa' antenna resonates at f_c = 2.460GHz in this free-space environment, with a null-depth of 20dB and a -10dB bandwidth of Δf_{-10dB} = 133MHz. This is in good agreement with the equivalent *measured* free-space parameters given earlier in Table 3.1 where f_c = 2.467GHz, the null-depth was 19.5dB and Δf_{-10dB} = 165MHz.

Finally, Figure 3.6 above shows a Smith-Chart of the simulated complex impedance (Z) of the antenna assembly in *free-space* at the centre-frequency of f_c = 2.4482GHz, giving a complex impedance of Z = (42+11j)Ω. This is fairly close to the nominal 50Ω quoted in Antenova's Specification [21]. The inductive part of Z here could be partially offset by replacing the short-circuit (in the vicinity of the antenna chip end of the transmission line) in the current simulations with a small capacitive matching element. It is noted that, in

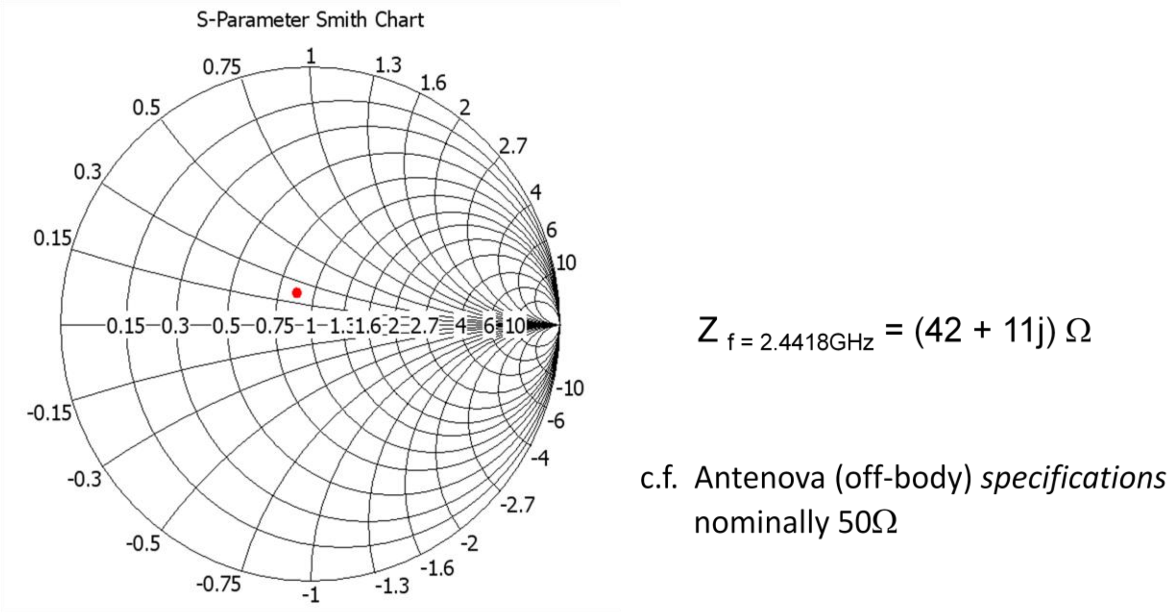

Figure 3.6: Smith-Chart of *Simulated* Impedance (Z) at f_c = 2.4482GHz for Antenova's 'Rufa' COTS Antenna in FREE-SPACE Scenario

fact, a small SMD matching capacitor is included, presumably for this purpose, at this location in the sample Antenova antenna supplied.

3.4.1.2.2 *On-Body* Simulations - Initial Results

To perform equivalent simulations for the *on-body* case, it is necessary to include a 'phantom' in the simulation model, to represent the RF characteristics of the nearby body tissues. These nearby tissues were emulated in the simulation by means of a three-layer dielectric sandwich, as suggested in [73]. The thicknesses (t), dielectric constants (ε_r) and conductivities (σ_r), of the three layers (skin, muscle and fat), along with the COTS antenna in close proximity, are shown in Figure 3.7.

In addition to the thicknesses of the three layers in the dielectric sandwich representing the nearby body tissues, it was also necessary to choose a representative *area*. This was initially performed by observing the effect on the antenna antenna's S-parameter characteristics of gradually increasing the area of this sandwich until such time as further increases were observed to have little significant effect on S11 for the antenna.

This S-parameter convergence criteria was found to be met when the length (L) and width (W) of the dielectric sandwich becomes about three times those of the antenna's Evaluation Board, giving (L x W x T) = (150mm x 63mm x 37mm), as shown. (Note: this preliminary sandwich size is also shown in Figure 3.7 here, as this permits the finer details to be seen more clearly than would be the case if the eventually adopted larger size dielectric sandwich, was shown).

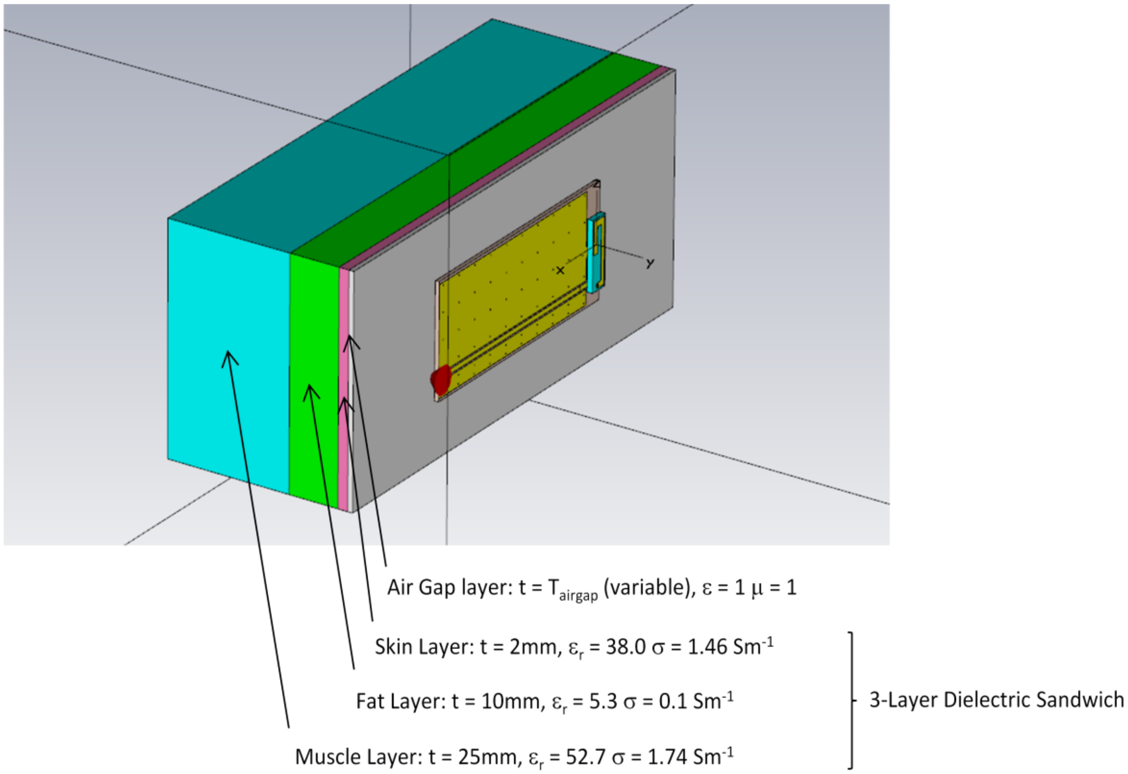

Figure 3.7 CST Simulation Model of Antenova's 'Rufa' COTS Antenna Located at a Variable Distance above the Representative Body in ONBODY Environment

However, subsequent further investigations found that, although this dielectric sandwich size was perfectly adequate from an S-parameter convergence point of view, it was too small to provide patterns which were representative of those measured on-body.

Now, adequately representative patterns were required for inclusion within subsequent Wireless Insite overall system modeling of the Body Centric Laboratory environment. In particular, to satisfactorily emulate the blockage experienced in Non Line of Sight (NLOS) conditions due to the intervening location of the body, it was found necessary to increase the dielectric sandwich size to (L x W x T) = (300mm x 200mm x 37mm). This larger size is about 60x the area of the antenna's Evaluation Board with (L x W) = (50mm x 21mm).

An initial simulation result for the 'Rufa' antenna chip mounted on its Evaluation Board at a typical 1mm above this more representative *much larger* sized three-layer dielectric sandwich is given below in Figure 3.8.

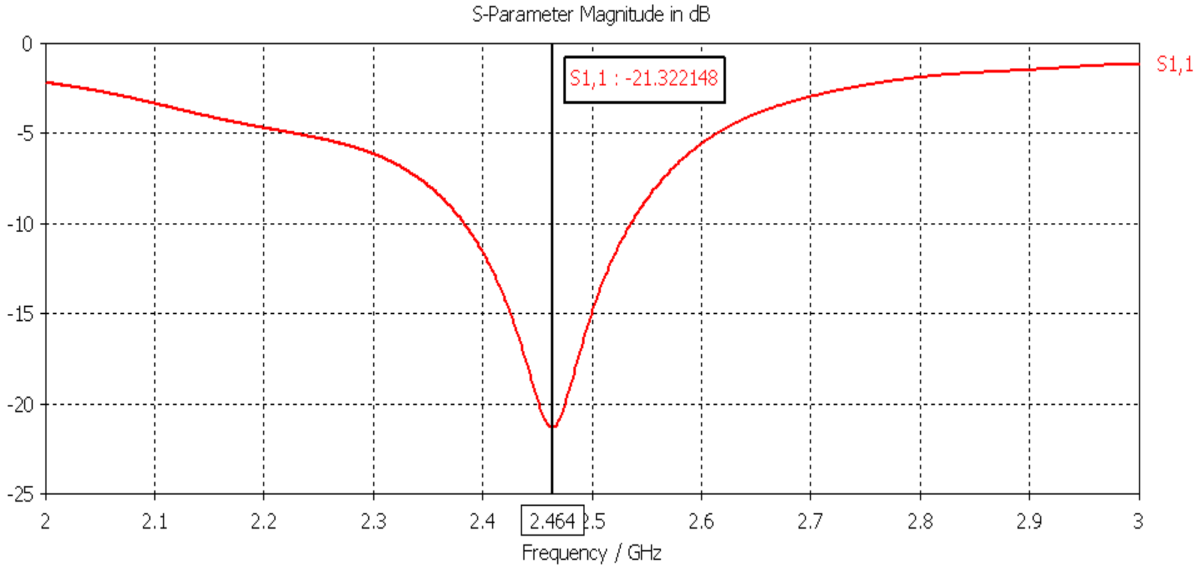

Figure 3.8: *Simulated* S11 versus frequency for Antenova's 'Rufa' COTS Antenna Located 1mm above the Larger Dielectric Sandwich Representing the Body in this ONBODY Environment (f_c=2.464GHz, Δf_{-10dB} = 152MHz)

This shows S11 versus frequency over a 2.0 to 3.0GHz band, which includes that designated for the ISM band.

This *simulated* S11 result in Figure 3.8 agrees well with the *measured* result given in Figure 3.2 earlier for the antenna assembly when located on the author's left-hand wrist with an intervening layer of cotton-wool padding (purple curve). In particular, the simulated centre-frequency and -10dB bandwidth here (2.464GHz and 152MHz respectively) are in excellent agreement with those *measured* (2.446GHz and 151MHz, as given earlier in Table 3.1). Further, both simulated and measured results indicate ample coverage of the complete 2.4GHz ISM band from 2.4000 to 2.4835GHz at the -10dB level.

3.4.2 Effect of Human Body on Antenna Directivity and Efficiency

CST *simulations* of 3-D antenna directivity patterns with associated efficiency were made for this COTS 'Rufa' antenna for both the Free Space and On-body cases. These allowed the effect of the nearby body on the *pattern* characteristics of the COTS 'Rufa' antenna to be predicted. Appropriate cuts in these 3-D simulated patterns to give 2-D polar patterns in the azimuthal plane were also determined to allow comparison with equivalent 2-D *measured* antenna *gain* patterns, as shown later in section 3.5.

3.4.2.1 *Free Space* Antenna Directivity and Efficiency

The *simulated* 3D total power pattern in *free-space*, shown here in Figure 3.9 overleaf, exhibit satisfactory agreement with those given in Antenova's spec sheet. These are largely omnidirectional in the elevation plane (Z-Y, where $\theta=[0,\pi]$) and generally omnidirectional in the azimuthal plane (X-Y, where $\phi = [0, 2\pi]$) but with a shallow null along the X-axis in the direction of the ground-plane of the 'Rufa' Evaluation Board. Further, the total efficiency (including both radiation and ohmic losses) is about 62%, which is in reasonable agreement with the 75% free-space value specified by Antenova.

Antenova have also confirmed that the dominant polarisation vector is along the X-axis i.e. aligned with the long side of the evaluation board. Hence, as simulated here, the antenna element is oriented such that it gives a far-field vector which in the azimuthal plane is predominantly horizontally polarised (H-pol).

Finally, to allow comparison with measurements, to be reported later in section 3.5, *simulated* 2-D cuts in the azimuthal plane of the simulated 3-D free-space pattern in Figure 3.9 were also made. These are deferred until are shown later as Figures 3.19a and 3.20a where, to suit requirements for exporting into the Wireless Insite SW package, the individual Co-polar and X-polar components, rather than their combined total power, are plotted.

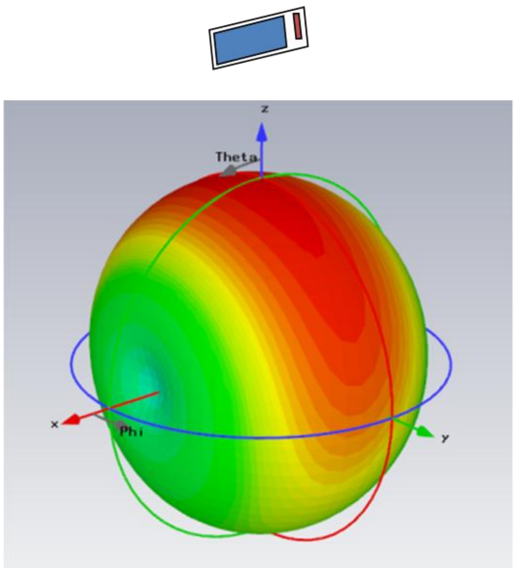

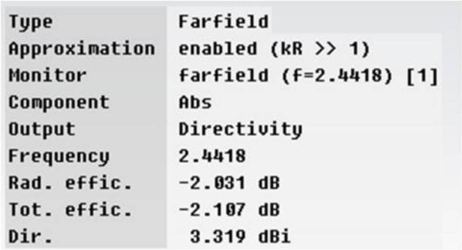

Type	Farfield
Approximation	enabled (kR >> 1)
Monitor	farfield (f=2.4418) [1]
Component	Abs
Output	Directivity
Frequency	2.4418
Rad. effic.	-2.031 dB
Tot. effic.	-2.107 dB
Dir.	3.319 dBi

Total efficiency = 100*(10^(-2.107/10)) ≈ 62%

Figure 3.9: *Simulated* 3D Far-Field (Total Power) Pattern at f_c = 2.4482GHz for Antenova's 'Rufa' COTS Antenna in FREE SPACE

3.4.2.2 *On-Body* Directive and Efficiency

Figure 3.10, overleaf, is the corresponding pattern obtained when the 3-layer dielectric sandwich, representing the human body in close proximity, is included. It is noted that the axes in Figure 3.10 here have been rotated by 90° with respect to those for the largely omnidirectional Free-Space patterns, given in Figure 3.9, to show the more representative blockage, caused by the presence of the body located on the –y-axis, more clearly.

Also, particularly significant in the far-field pattern parameters, given in Figure 3.10, is the severe reduction in the total efficiency of the antenna to 1.5% for this *on-body* scenario from the 62% value in its original *free-space* environment. However, this is to be expected of any non-directional antenna, due to energy loss by heating of the nearby body tissues, and is not unique to this particular 'Rufa' design.

Also particularly significant in the far-field pattern parameters, given in Figure 3.10, is the severe reduction in the total efficiency of the antenna to 1.5% for this *on-body* scenario from the 62% value in its original *free-space* environment. However, this is to be expected of any non-directional antenna, due to energy loss by heating of the nearby body tissues, and is not unique to this particular 'Rufa' design.

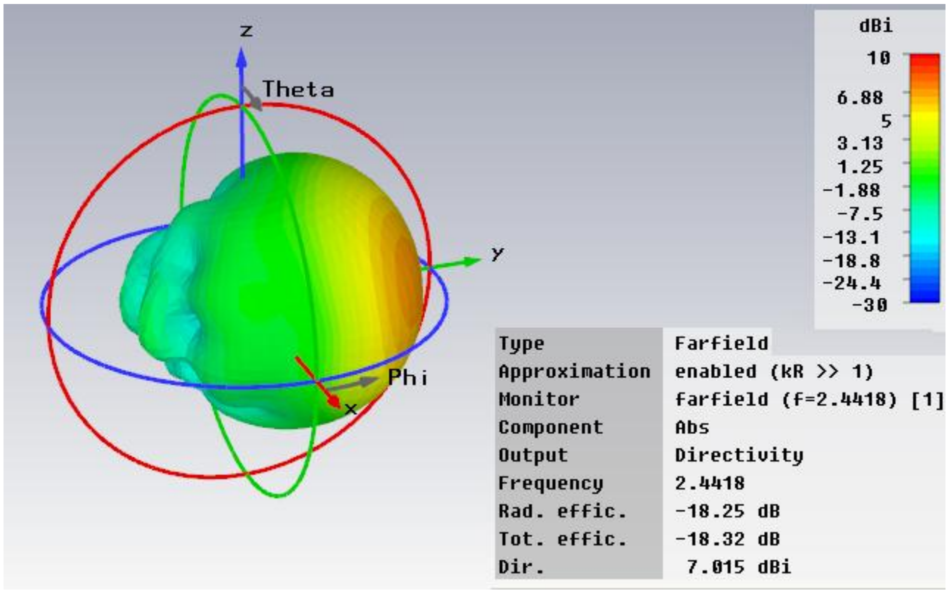

Type	Farfield
Approximation	enabled (kR >> 1)
Monitor	farfield (f=2.4418) [1]
Component	Abs
Output	Directivity
Frequency	2.4418
Rad. effic.	-18.25 dB
Tot. effic.	-18.32 dB
Dir.	7.015 dBi

Total Efficiency = 100 * (10^(-18.32/10) = 1.5%

Figure 3.10: *Simulated* 3-D Far-field Patterns at f_c = 2.4482GHz in ON BODY Environment for Antenova's 'Rufa' COTS Antenna Located 1mm above the *Larger more Representative* Body

Finally, for completeness, Figure 3.11 overleaf shows the simulated impedance of the on-body antenna assembly at f_c = 2.4482GHz centre frequency, showing that its complex impedance is now Z = (39 – 1j)Ω. This is marginally different from the nominal 50Ω *free-space* value quoted in Antenova's Specification.

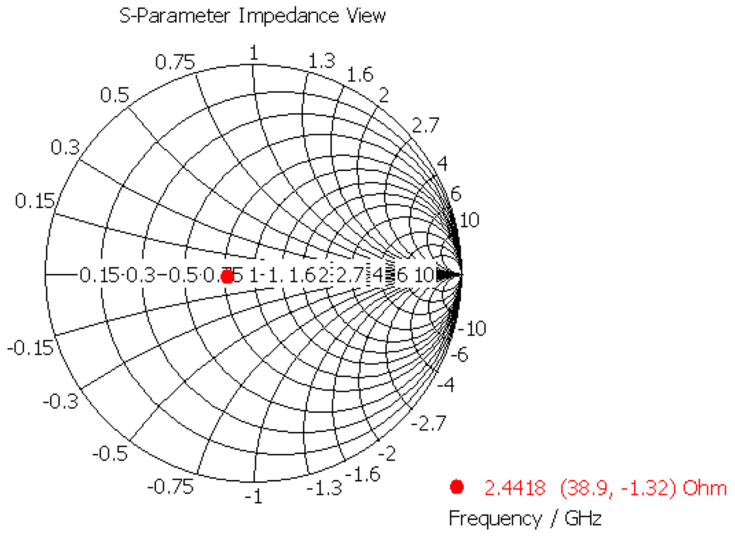

Figure 3.11: *Simulated* Impedance at f_c = 2.4482GHz in ON BODY Environment for Antenova's 'Rufa' COTS Antenna Located 1mm above the Larger more Representative Body

3.5 *Un*anticipated Effects of Human Body in Close Proximity to Unshielded Antenna

Whilst confirming the *anticipated* effects of detuning and reduction in efficiency when the unshielded antenna is used in close proximity to the human body, two interesting *un*anticipated effects were also discovered, namely:

i) that the (otherwise) reasonably polarised Free Space patterns of this COTS antenna became almost completely depolarised when it is relocated to be in close proximity to the body, and

ii) when a *pair* of such antennas having a common polarisation are located closely spaced on a common body, mutual coupling between them is much reduced in comparison to that experienced in free-space conditions.

The depolarisation effect, because it primarily concerns a *single* on-body antenna in isolation, is considered first in sub-section 3.5.1, following.

However, to avoid possible confusion, because the mutual coupling reduction effect concerns a *pair* of on-body antennas, discussion on this topic is deferred until section 3.8 when considerations of the single antenna are complete.

3.5.1 Effect of Human Body on Antenna Polarisation

The depolarising effect of the body on the 'Rufa' antenna was first observed in CST simulations of the Rufa antenna when located in close proximity to the body.

However, this simulated observation was subsequently verified by means of anechoic chamber pattern measurements, with the Rufa located on the author's chest (with intervening clothing of 2 to 3mm thickness). These measurements confirm that the depolarisation effect observed in the simulations is not an artefact, but is indeed genuine.

3.5.1.1 On-Body Depolarisation Effect – CST *Simulation* Technique

CST Simulations were conducted with the accurate model of the Rufa antenna when located in close proximity to an approximate model of the body. Again, the approximate model of the body used here was the more representative much larger planar 3-layer dielectric sandwich with (L x W x T) = (300mm x 200mm x 37mm).

Now however, rather than plotting the *total* 3-D far-field pattern given originally in Figures 3.9 and 3.10, its individual co-polar and x-polar components on a 2-D cut in the azimuthal plane are plotted here to derive the average co/x-polar ratio in this plane.

Different separations of the Rufa antenna from the body were investigated, with separations of 1mm and 3mm being reported here in sub-section 3.5.1.3.

For comparison purposes, *Free-Space* pattern simulations with*out* the dielectric sandwich are also included for this 'Rufa' antenna.

3.5.1.2 On-Body Depolarisation Effect – *Measurement* Technique

2-D Azimuthal co-polar and x-pol patterns of the COTS Rufa antenna were measured, as illustrated in Figure 3.12 below, in an anechoic chamber using a turntable capable of rotating in azimuth only. The longer edge of the antenna's associated PCB was now vertical, so that the antenna's (Free Space) electric field was also predominantly vertically polarised.

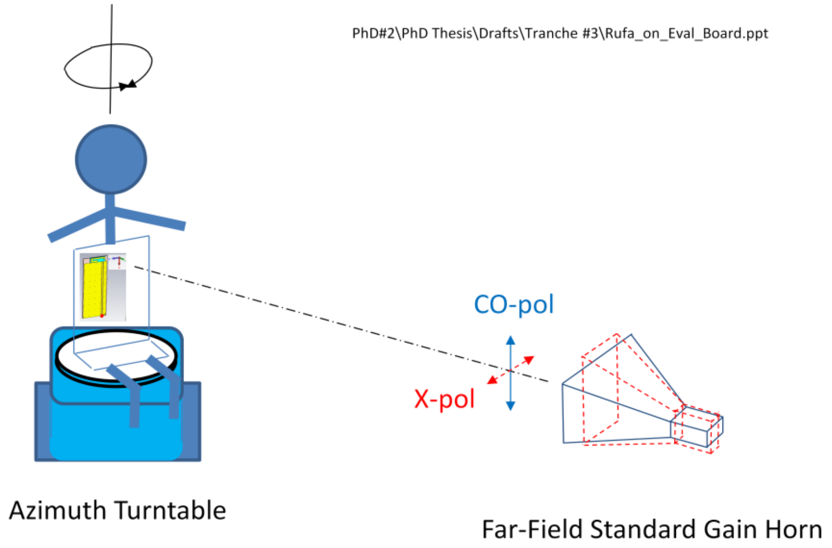

Figure 3.12: Experimental Set-up for Pattern *Measurements* of Antenova's 'Rufa' COTS Antenna Assembly in QMUL's Anechoic Chamber

On-body pattern measurements were made with this 'Rufa' antenna taped to the author's chest whilst seated and wearing 3 thin layers of intervening clothing that were estimated to be 2 to 3mm thickness in total.

For comparison purposes, *Free-Space* pattern measurements were also made with this Rufa antenna assembly taped to a foam polystyrene block that consists largely of air.

In both the Free Space and on-body cases, a vertically polarised standard horn transmit antenna was used in the far-field to allow the 'Rufa' antenna's CO-polar azimuthal pattern to be measured. Subsequently, in the conventional manner, to measure the Rufa antenna's X-pol patterns the standard far-field horn was then rotated by 90° (to provide horizontal polarisation) with the Rufa antenna's orientation remaining vertical.

3.5.1.3 On-Body Depolarisation Effect – Simulated and Measured Results

Figure 3.13 below shows the *free space* co-polar and x-polar azimuthal 2-D polar patterns for the 'Rufa' antenna and includes both *simulations* and *measurements* on a common plot.

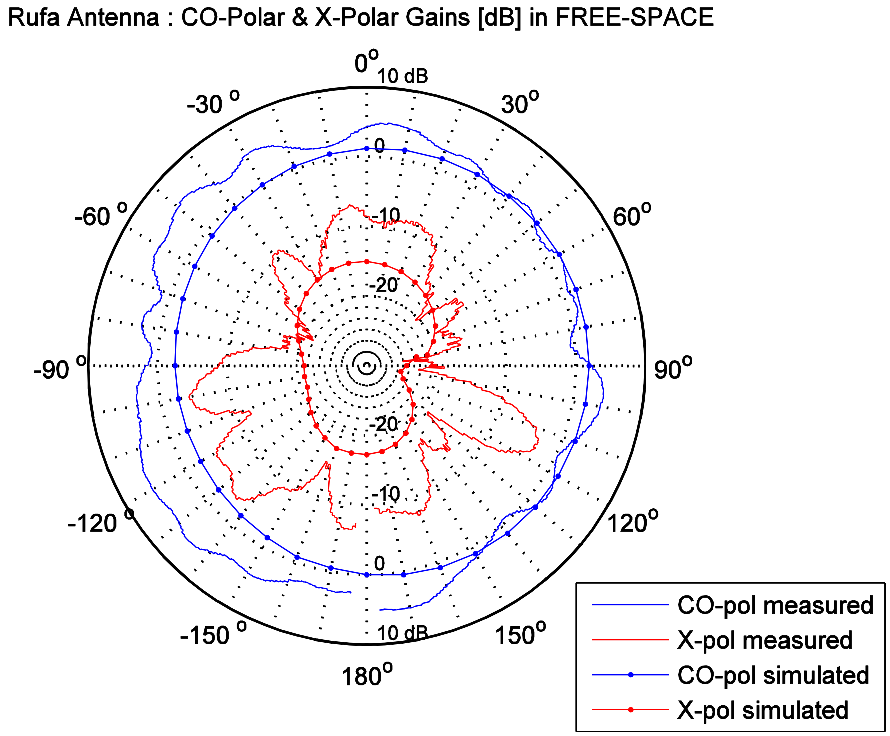

Measured: (Av CO-pol Gain)/(Av X-pol Gain) = (3.27 - (-9.28) ≈ 13dB
Simulated: (Av CO-pol Gain)/(Av X-pol Gain) = (0.48 - (-18.21) ≈ 19dB

Fig 3.13: Simulated and Measured CO-pol and X-pol Azimuthal Gains for V-pol orientated ‘Rufa’ Antenna in FREE SPACE

Figure 3.14 below shows the corresponding simulated and measured patterns when the ‘Rufa’ antenna is relocated to be *on-body* with T_{airgap} = 2mm separation between this antenna and the author’s chest.

The average powers (over the full 360° azimuthal sector involved in these patterns) were calculated and are included both these figures. Plainly, to derive these, the individual powers in dB had first to be converted to linear powers, before averaging, which then had to be reconverted back to dB form.

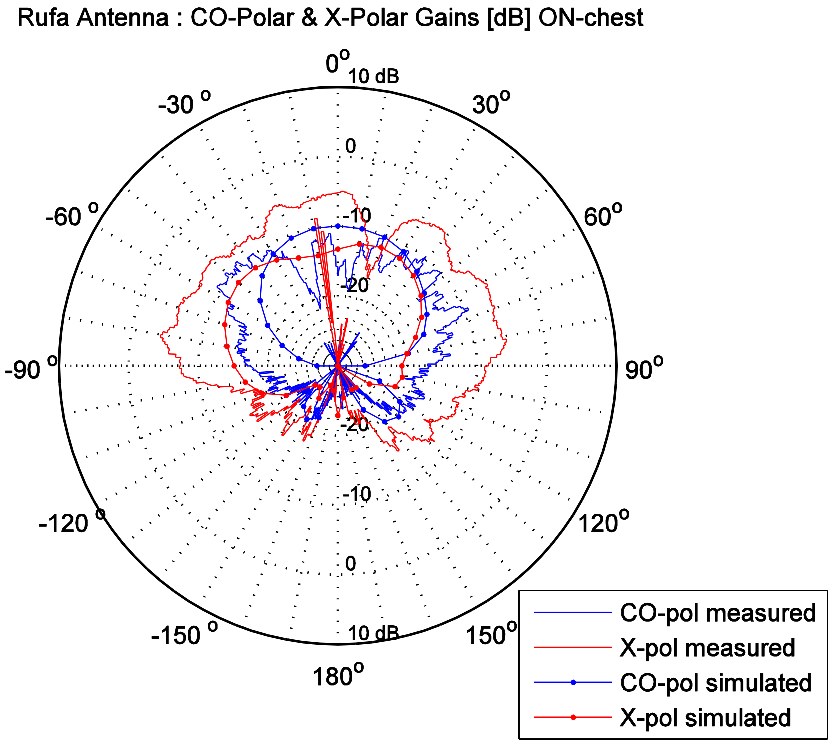

Measured: (Av CO-pol Gain)/(Av X-pol Gain) = (-15.09 - (-9.04) ≈ -6dB
Simulated: (Av CO-pol Gain)/(Av X-pol Gain) = (-15.75 - (-15.90) ≈ 0dB

Fig 3.14: Simulated and Measured CO-pol and X-pol Azimuthal Gains V-pol orientated ‘Rufa’ Antenna Located 2mm away from Body in ONBODY case

Table 3.2 below, shows a comparison of the effect of the body on the average CO/X-polar ratio on a cut in the azimuthal plane for both measurements and simulations.

Case	(Av. CO-pol dir)/(Av. X-pol dir) Ratio [dB]			
	Measured	Simulated		
	$T_{airgap} \approx 2mm$	T_{airgap}=1mm	T_{airgap} = 2mm	T_{airgap} = 3mm
(1) Free-Space	13	19		
(2) Onbody (LH chest)	-6	0	0	6
((1) – (2)) (effect of body)	19	19	19	13

Table 3.2: Measurements ($T_{airgap} \approx$ 2mm) and simulations (T_{airgap}=1, 2 & 3mm) for the average CO/X)-pol Ratio for Onbody and Free Space cases.

It can be seen that, in both simulations and measurements, significant (19dB) reduction in the ratio of average co-pol to average x-pol directivities occurs when the antenna is relocated from free-space to be in close proximity with an intervening small 2mm air gap.

The *simulated* results in Table 3.2 also show that the depolarising effect increases from 13dB to 19dB when the air gap between the antenna and the dielectric sandwich is reduced from 3mm to 1mm. As anticipated, this is a direct consequence of the closer body exerting increasing influence on the antenna.

3.6 Further Investigation of the Depolarisation Effect of the Body on the Antenna Patterns

Having established that the presence of the body in close proximity to the ‘Rufa’ antenna completely depolarises its (otherwise) quite reasonably polarised patterns, three questions immediately arise concerning this:

i) To what extent does the *size* of the dielectric sandwich representing the body influence this depolarisation effect?
ii) To what extent does the *proximity* of the dielectric sandwich to this antenna influence this depolarisation effect?
iii) Finally, whether the depolarisation effect is generic to *all* (unshielded) antenna types when used onbody, or whether the effect is specific to the candidate COTS ‘Rufa’ antenna investigated here?

3.6.1 Quantifying the Effect of the *Size* of the Dielectric Sandwich Representing the Body

The *size* of the dielectric sandwich is particularly relevant, as it determines whether this sandwich used to emulate the body in the CST simulations is sufficient to be adequately representative or not.

This was partly addressed earlier in sub-section 3.4.1.2.2, where it was found that a 3-layer skin, fat and muscle sandwich of overall size (L x W x T) = (150mm x 63mm x 37mm), whose area is about 9x that of the area of the ‘Rufa’ antenna’s ground-plane, was adequate to represent the effect of the body *as regards the S-parameter convergence criterion*.

However, as briefly mentioned earlier in sub-section 3.4.1.2.2, it subsequently became apparent that this area of dielectric sandwich was insufficient to give adequately representative *patterns* of those when the ‘Rufa’ antenna is located *on*-body. In particular, a sufficient level of blockage in the antenna pattern is required in the NLOS situation when the patient/client happens to be situated such that their body lies directly between the onbody antenna and its associated off-body Access Point (AP). Only then, are the patterns suitable for importing into the Wireless Insite simulations of the overall system in the Body Centric Laboratory.

Thus, the area of the dielectric sandwich used to emulate the body was iteratively increased, until the overall size became (L x W x T) = (300mm x 200mm x 37mm). This area is now about 57x that of the area of the ‘Rufa’ antenna’s ground-plane i.e. a roughly 6-fold increase over that used originally and is more consistent with the sizes of larger body parts (such as the chest) considered here.

For reasons of brevity here, detailed results for only the two most extreme dielectric sandwich sizes *simulated* are shown below in Figures 3.15a to 3.20a and Figures 3.15b to 3.20b, for (L x W x T) = (150mm x 63mm x 37mm) and (300mm x 200mm x 37mm) respectively.

In both cases, the same small intervening air gap of T_{airgap} = 2mm thickness between the antenna and the surface of the body is assumed. Also, Figures 3.17 to 3.20 are all at the same frequency f_c^{ISM}=2.4418GHz at the centre of the ISM-band.

Figure 3.16 shows the *simulated* S11 vs. frequency for the two dielectric sandwich sizes here. Figure 3.16b for the larger dielectric size agrees better (than Figure 3.16a for the smaller dielectric) with the equivalent measured parameter shown earlier in Figure 3.2 and derived parameters given in Table 3.1.

This is particularly true of the simulated and measured null-depths involved, and the shallower null-depth (~21dB) in Figure 3.16b is consistent with the slighter poorer

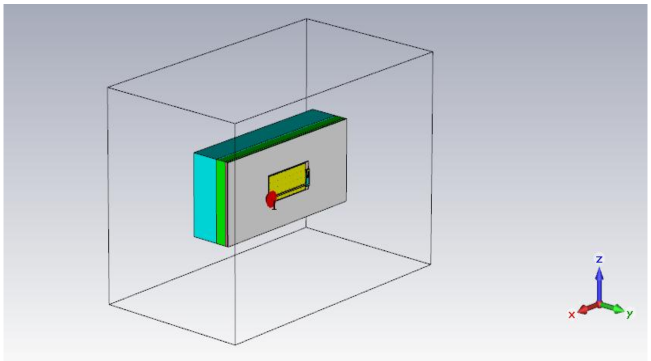

Figure 3.15a: (150mm x 63mm x 37mm)

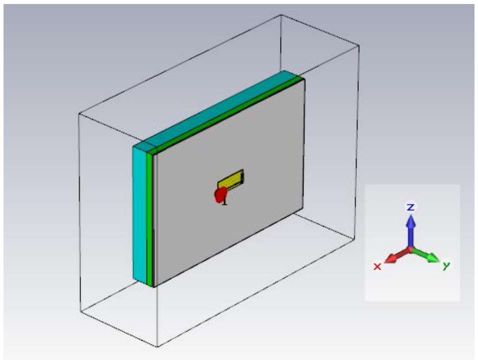

Figure 3.15b: (300mm x 200mm x 37mm)

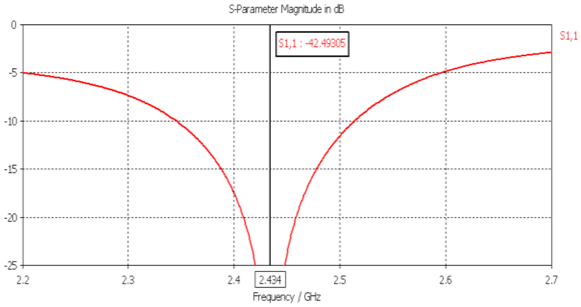

Figure 3.16a: S11 vs. frequency

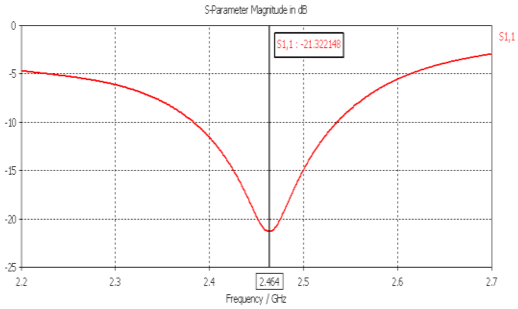

Figure 3.16b: S11 vs. frequency

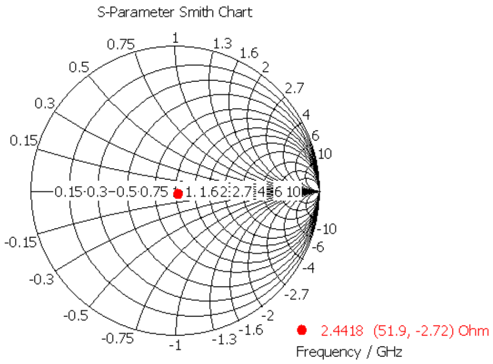

Figure 3.17a: Impedance (Smith Chart)

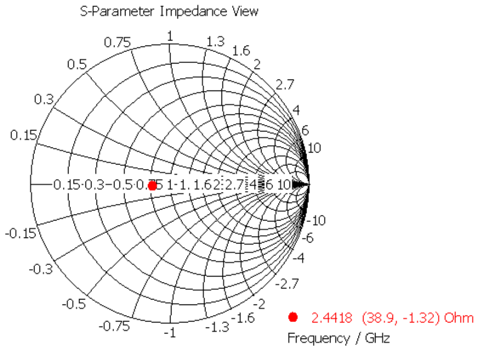

Figure 3.17b: Impedance (Smith Chart)

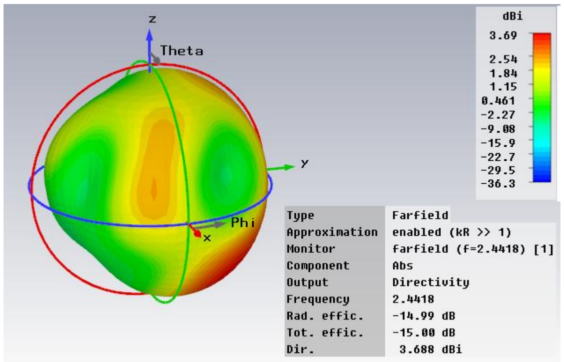

Type	Farfield
Approximation	enabled (kR >> 1)
Monitor	farfield (f=2.4418) [1]
Component	Abs
Output	Directivity
Frequency	2.4418
Rad. effic.	-14.99 dB
Tot. effic.	-15.00 dB
Dir.	3.688 dBi

Figure 3.18a: 3-D Absolute patterns

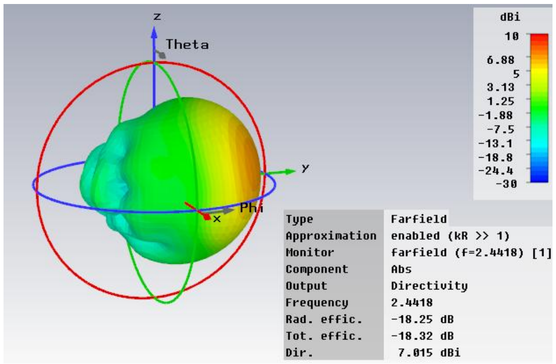

Type	Farfield
Approximation	enabled (kR >> 1)
Monitor	farfield (f=2.4418) [1]
Component	Abs
Output	Directivity
Frequency	2.4418
Rad. effic.	-18.25 dB
Tot. effic.	-18.32 dB
Dir.	7.015 dBi

Figure 3.18b: 3-D Absolute patterns

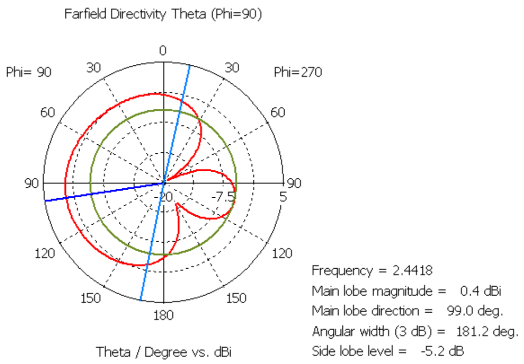

Figure 3.19a: 2-D CO-pol component

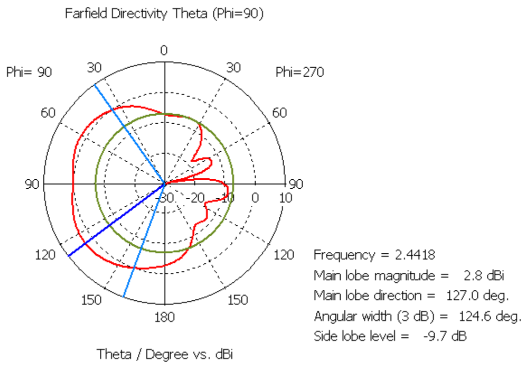

Figure 3.19b: 2-D CO-pol component

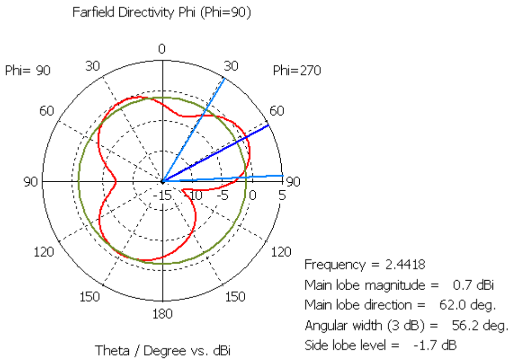

Figure 3.20a: 2-D X-pol component

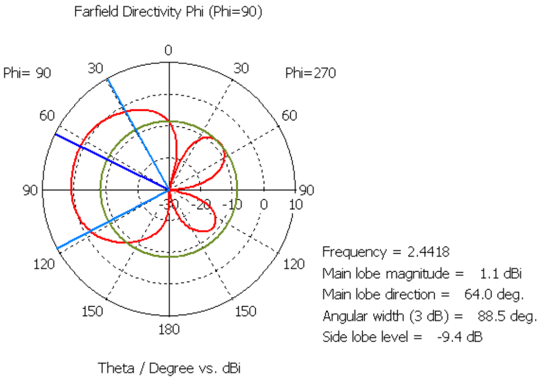

Figure 3.20b: 2-D X-pol component

impedance match ((38.9 – 1.32j)Ω), shown in Figure 3.17b, to the reference 50Ω system impedance.

Figure 3.18 shows the 3-D total power patterns. Evidently, owing to its increased body-blockage, the larger dielectric of Figure 3.18b is causing the directivity in the direction of the body (-y direction) to be suppressed with respect to that in Figure 3.18a. Also, in the direction away from the body (+y direction) the antenna assembly becomes more directional (~3dB). However, the *gain* of the assembly in the two cases remains very comparable because, as might be expected, the efficiency of the antenna assembly is ~3dB lower with the larger dielectric.

Figures 3.19 and Figure 3.20 show 2-D azimuthal cuts in the previous 3-D total power patterns. The individual co-polar and cross-polar components, which together comprise the total powers, are shown in Figure 3.19 and Figure 3.20 respectively. In particular, from Figures 3.19b and 3.20b (both for the larger dielectric) show that the co-polar and cross-polar components become very comparable when on-body. This is in accordance with the observed depolarisation effect of the body in close proximity to the antenna described earlier.

The main conclusion to be drawn from Figures 3.15 to 3.20 above is that the *size* of the dielectric sandwich, required to adequately emulate the effect of the nearby human trunk on the ‘Rufa’ antenna (especially its pattern characteristics with adequate blockage by the body in the –y-axis direction), should be (L x W x T) ≥ (300mm x 200mm x 37mm).

Although not shown here, equivalent sets of figures were also derived for two more intermediate sized dielectric sandwiches. Derived results for all the onbody simulations and measurements, as well as their equivalent free-space specifications, are reproduced in Table 3.3 overleaf for the candidate COTS ‘Rufa’ antenna investigated here. This more comprehensive summary allows behavioural trends to be deduced.

(PhD#2\Effect of dielectric sandwich size T=2mm (Thesis version 5).xls)

Case	Dielectric Sandwich Size Representing Body in Simulations	Parameters at Fc = 2.4418GHz (ISM-band)			Fres	-10dB Bandwidth
		CO-pol Directivity	Radiated Efficiency			
	[mm]	[dBi]	[dB]	[%]	[GHz]	[MHz]
Antenova Specifications	N/A (Free Space)	+2.1	-1.2	75	2.443	170
WDW Measurement (6th Sep 2010)	N/A (on author's chest with 3 intervening layers of clothing)	Not measured (instead, G = D *η measured using standard-gain horn in chamber)			2.468	165
WDW CST Simulations						
(20th Feb 2013)	(150 x 63 x 37)	-7.9	-14.03	4.0	2.507	131
(20th Feb 2013)	(200 x 84 x 37)	-3.8	-16.03	2.5	2.503	133
(20th Feb 2013)	(250 x 103 x 37)	+2.2	-16.21	2.4	2.504	134
(20th Feb 2013)	(300 x 200 x 37)	+2.7	-15.89	2.6	2.521	124

Table 3.3: Effect of Dielectric Sandwich Size for all four sizes Investigated with Intervening Air Gap Thickness T_{airgap} = 2mm

Provided a small intervening air-gap (~2mm) is maintained between the antenna and the body, Table 3.3 shows the following behavioural trends in response to different *sizes* of the dielectric sandwich representing the nearby body in the CST simulations:

i) The simulated onbody antenna's directivity gradually increases as the increasing dielectric sandwich size exerts more directive influence on the antenna in the forward direction; causing the width of the main beam to be reduced,

ii) The simulated antenna's onbody simulated efficiency gradually decreases as the increasing dielectric sandwich size absorbs more of the radiated energy, which it ultimately converts to heat,

iii) The simulated antenna's resonant frequency (F_{res}) is not significantly affected by the size of the dielectric sandwich over the range investigated here although, as expected, it *is* slightly lower than the Free-Space value,

iv) The simulated -10dB bandwidth of the onbody antenna assembly is not significantly affected by the dielectric sandwich size, and only marginally lower than that measured on the author's chest.

3.6.2 Quantifying the Effect of the Dielectric Sandwich *Proximity* to the Onbody Antenna

This body proximity issue was partly addressed in Table 3.2 earlier, which showed results of the depolarisation effect of the body on the 'Rufa' antenna patterns, in terms of its average CO/X-pol ratios, for various intervening air-gap thicknesses between the antenna and the dielectric sandwich (T_{airgap} = (1mm, 2mm and 3mm) here).

Figures 3.21 to 3.23 overleaf show the resulting *antenna patterns* for the two most extreme cases investigated with T_{airgap} = 1mm and T_{airgap} = 3mm; being cases 'a' and 'b' here respectively.

Figure 3.21 shows patterns of their absolute power, whilst figures 3.22 and 3.23 show the corresponding constituent CO-pol and X-pol components. Patterns for the intermediate case with T_{airgap} = 2mm are not shown here, since they were found to be intermediate between patterns for these two most extreme cases.

The absolute patterns Figure 3.21 show that there is no major difference between these two extreme proximity cases, although the patterns for the body in closer proximity (case 'a' having T_{airgap} = 1mm) are slightly more directional than those for case 'b' with T_{airgap} = 3mm). In addition, for the body in closer proximity (case 'a') has sidelobe levels which are ~4dB lower than case 'b'. Both these findings are to be expected since, as the body becomes closer to the antenna, the geometry involved gives rise to increased occlusion of the antenna by the body.

Comparison of Figure 3.22a with Figure 3.22b, and Figure 3.232a with Figure 3.23b, shows that the corresponding patterns of the different air-gaps are not qualitative different and are only marginally different in their quantitative effect.

In addition to observations on the effect of varying the air-gap thickness on the pattern characteristics just given, for completeness the effect on *other* significant RF antenna parameters of doing likewise is shown in Table 3.4 which follows shortly.

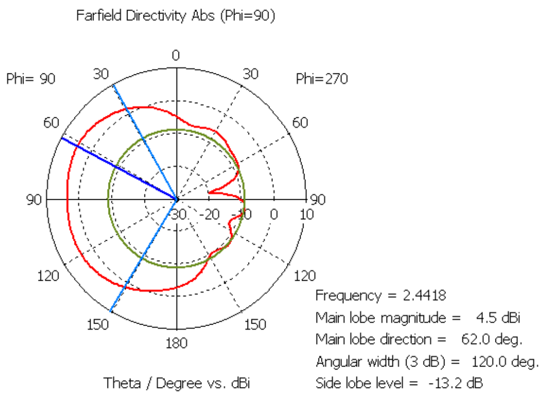

Figure 3.21a: 2-D Absolute patterns (T_{airgap} = 1mm)

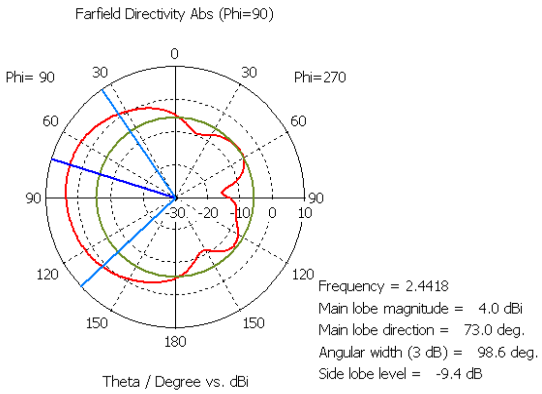

Figure 3.21b: 2-D Absolute patterns (T_{airgap} = 3mm)

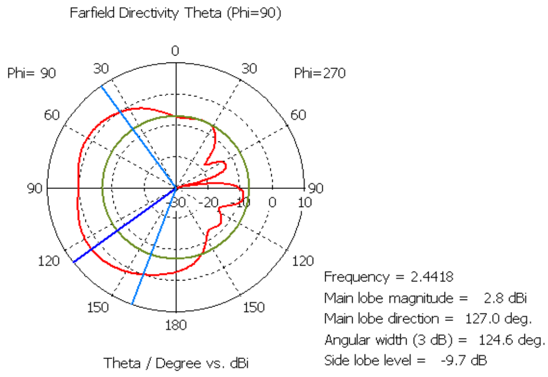

Figure 3.22a: 2-D CO-pol component

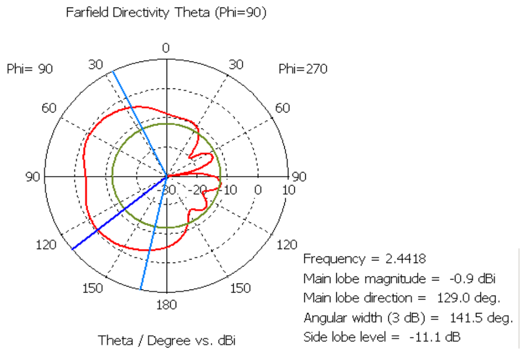

Figure 3.22b: 2-D CO-pol component

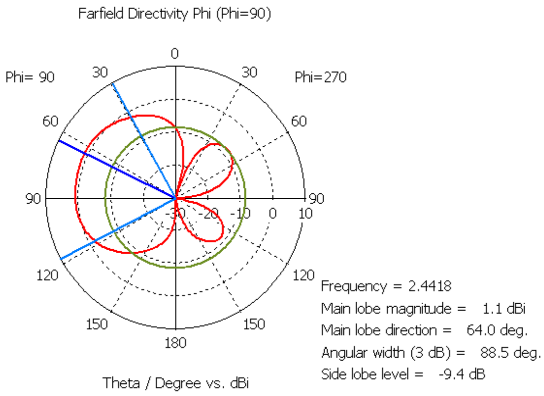

Figure 3.23a: 2-D X-pol component

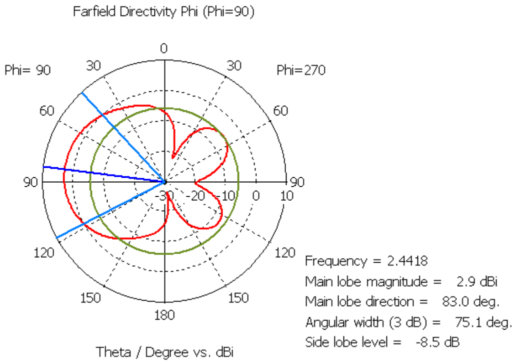

Figure 3.23b: 2-D X-pol component

(PhD#2\Effect of Body Proximity EXTRA HUMUNGOUS dielectric (Thesis version 5).xls

Case	Thickness of Air Gap [mm]	Parameters at Fc = 2.4418GHz (ISM-band) CO-pol Directivity [dBi]	Radiated Efficiency [dB]	[%]	Fres [GHz]	-10dB Bandwidth [MHz]
Antenova Specification	Not Applicable (Free-Space)	2.1	-1.2	75.0	2.443	170
WDW Measurement (6th Sep 2010)	2 to 3 (on-chest with 3 layers of clothing)	Measured G = D * η (using standard-gain horn)			2.468	165
WDW CST Simulations						
(18th Feb 2013)	1	+0.2	-18.25	1.5	2.464	152
(20th Feb 2013)	2	+2.7	-15.89	2.6	2.521	124
(16th Feb 2013)	3	-3.6	-15.89	2.6	2.521	125

Table 3.4: Derived Parameters for three Dielectric Sandwich Proximities Investigated with Dielectric Sandwich Sized (L x W x T) = (300mm x 200mm x 37mm) (i.e. large)

Table 3.4 shows that as the body gets closer to the 'Rufa' antenna (T_{airgap} decreasing), so that the antenna might be expected to experience increasing influence of the body, then the following trends in the antenna parameters can be observed:-

i) Its directivity initially increases significantly, from -3.6dBi at (T_{airgap} = 3mm) to +2.7dBi at (T_{airgap} = 2mm), but then reduces to +0.2dB at the closest approach (T_{airgap} = 1mm),
ii) its radiated efficiency decreases,
iii) its resonant frequency decreases, and finally
iv) its -10dB bandwidth increases slightly.

Trends ii), iii) and iv), and the *initial* trend in i), are in accordance with intuitive expectations, but the final trend in i) could be considered counter intuitive. However, the latter effect might be due to additional more complex propagation mechanism(s), such as surface-wave propagation, assuming increased significance at this closest distance.

In conclusion, therefore, the 'Rufa' antenna's behaviour when in close proximity with varying intervening air-gap thickness (T_{airgap}) is largely as expected.

3.6.3 Determining Whether Depolarising Effect is Specific to the Candidate 'Rufa' Antenna Investigated or Applicable to Other Antenna Types as well

Up to this stage, investigations of the effects of the human body in close proximity to the antenna on its RF parameters have only been reported for the candidate COTS 'Rufa' antenna.

However, it would also be of interest (to *system* engineers, in particular) to know whether the body's depolarising effect is specific to the 'Rufa' antenna, or whether it applies to other (small) onbody antennas. For example, an effect which (consistently) depolarises a receive antenna should make it less sensitive to polarisation misalignments between the antenna and the incoming electromagnetic fields which it is supposed to receive. Therefore, such an antenna might be expected to be more robust in terms of variations in its orientation and any propagation induced uncertainty in polarisation. So this result might be of generic significance for mobile applications in multipath-rich indoor environments.

A further incentive to investigate this was that a physical analysis, to be presented later in Chapter 4, had been conducted by the present author to investigate a possible underlying mechanism behind this depolarisation effect. This showed that an 'ideal' antenna type, specified only as giving two orthogonal linearly polarised components (CO & X-pol) at a given relative level, is also expected to experience a reduction in its CO/X-pol ratio when in close proximity to a dielectric object.

So, to resolve the question of whether or not the depolarisation effect of the nearby body is uniquely applicable to the 'Rufa' antenna used so far, a convenient CST model of a simple printed-monopole type antenna was found by way of an alternative.

Like the 'Rufa' antenna previously investigated, this printed-monopole type antenna is also designed to operate in the 2.4GHz ISM-band. As can best be seen in figure 3.24a, the antenna itself here comprises a standard FR4 dielectric printed circuit board of size (Width x Length x Thickness) = (80mm x 70mm x 1.6mm), which is partially coated on one side with a conductive Ground Plane of size (73mm x 43mm x 0.1mm). On the opposite side lies a conductive microstrip of size (3mm x 63mm x 0.1mm). This, protruding beyond the ground plane by (63 – 43) = 20mm on their common dielectric substrate, constitutes a (λ/4) monopole antenna in its most basic form.

Figure 3.24 shows the assembly here comprising the monopole antenna plus a dielectric material. It is noted that the monopole axis here and the polarisation vector of the 'Rufa' dipole investigated previously, are both aligned to the z-axis. This was deliberately arranged in order to enable direct comparison of their subsequent patterns on a like-for-like basis.

The CST simulation model and the resulting key RF parameters, including CO and X-pol antenna patterns, are shown in Figures 3.24 to 3.29 overleaf for two cases:

a) with a single dielectric *slab* (of optimum size (300mm x 200mm x 37mm)), whose RF parameters are representative of *Free-Space* ($\mu_r = \varepsilon_r = 1.000$ and $\sigma = 0.000\text{Sm}^{-1}$), and
b) with a dielectric *sandwich* of the same size, comprising 3-layers, whose RF parameters are the same as those given earlier in Figure 3.7, which was used earlier for *onbody* simulations of the 'Rufa' antenna.

These figures are presented in a manner that permits easy comparison between the two cases.

Like Figure 3.16 for the 'Rufa' antenna, Figure 3.25 for the monopole antenna, shows a plot of *simulated* S11 vs. frequency both in free-space and onbody. Initially, the model for the antenna in the immediate vicinity of the body gave a resonant frequency which was marginally *higher* than that for the free-space antenna. This was plainly unphysical and subsequent investigation revealed that this model had not fully converged. However, once the simulation convergence criteria were optimised and improved convergence obtained, the free-space result shown in 3.25a was observed. By comparison with the onbody result in Figure 3.25b, it is now evident that this result exhibits the physically correct *lowering* in frequency when in close proximity to the body.

Figures 3.26a and 3.26b respectively show the impedances for the free-space and onbody cases. Not surprisingly, these are slightly different, but both remain in reasonable agreement with the nominal 50Ω for this antenna design.

Figures 3.27a and 3.27b show the 3-D absolute patterns for the free-space and onbody cases respectively.

The free-space pattern in Figure 3.27a exhibits the expected null along the axis of the monopole in the +z direction and, although not visible here, it was confirmed that there is also an even deeper null in the –z direction. The asymmetry between the upper and lower hemispheres in Figure 3.27a is likely to be due to the asymmetry in the printed monopole structure on account of its ground-plane. Originally, the total efficiency was +1.1dB which is clearly unphysical. However, this value was gradually reduced to 0.36dB appearing in Figure 3.27a following incremental improvements in convergence criteria. It seems likely that this trend could be further pursued to give a physical value of ≤ 0.0dB.

More importantly here, however, is that the onbody pattern in Figure 3.27b shows a realistic blockage of the antenna’s free-space pattern by the dielectric sandwich representation of the body here (i.e. in the –y direction).

Finally, Figure 3.28 and 3.29 show 2-D cuts in the azimuthal plane for the constituent co-polar and x-polar components making up the absolute power patterns previous given in Figure 3.27. Once again (as for the ‘Rufa’ antenna) it is clearly evident that the co/x-polar ratio for the monopole in free-space (case a)) is much higher than onbody.

The key average CO and X-pol parameters for this printed monopole antenna were extracted from Figures 3.28 and 3.29 above and shown in Table 3.5 following. Also included here are the corresponding parameters, given earlier in Table 3.3, for the candidate ‘Rufa’ COTS antenna to allow direct comparison between the two antenna types. Finally, the last column in Table 3.5 gives the resulting Co/X-pol ratios for the two antenna types in both free-space and onbody conditions.

Comparison of the Co/X-pol onbody ratios to their free-space equivalents allows the effect of the nearby body on this ratio to be assessed for each antenna type. It can be seen that, for the ‘Rufa’ antenna, the presence of the nearby body causes a (+19 – 0) = 19dB reduction in the Co/X-pol ratio, whilst the printed monopole experiences a similar (+57 – 36) = 21dB reduction in the forward direction and (more in the backward direction).

Thus, the body in close proximity to the antenna has a similar depolarising effect on the antenna for *both* antenna types. However, because the printed monopole antenna starts off with a much higher CO/X-pol Ratio (in free-space) than the ‘Rufa’ antenna, its CO-pol component remains higher than its X-pol component when relocated to be on-body.

In conclusion, therefore, this exercise using a printed monopole antenna has shown that the depolarising effect of the body on the antenna is *not specific* to the original candidate ‘Rufa’ COTS antenna. However, on the basis of just two examples of this antenna type, it is probably premature at present to claim that this depolarisation effect will occur for all unshielded (and therefore largely omnidirectional) antenna types.

Nonetheless, this is in accordance with the author’s analysis, reported later in Chapter 4, which identifies a possible depolarisation mechanism and quantifies this effect assuming an ‘ideal’ largely omnidirectional electromagnetic source having two orthogonal linear components. A more detailed investigation of the extent to which this depolarisation effect applies would be an interesting avenue of further study.

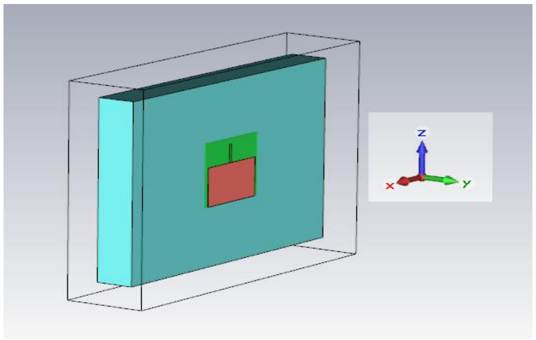

Figure 3.24a: (ε_r=1.0, μ_r=1.0, σ=0 Sm^{-1})
(i.e. FREE-SPACE)

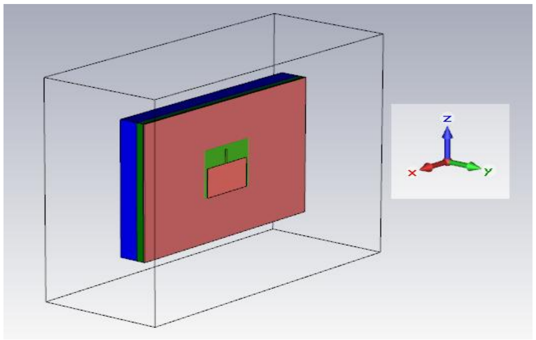

Figure 3.24b: (ε_r, μ_r, & σ's as in Figure 3.6)
(i.e. ON-BODY)

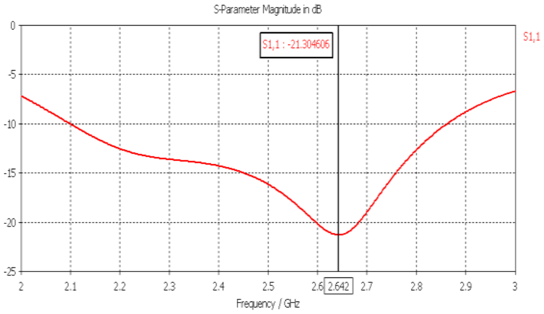

Figure 3.25a: S11 vs. Frequency

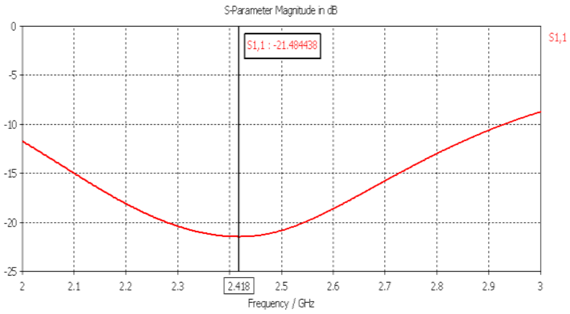

Figure 3.25b: S11 vs. Frequency

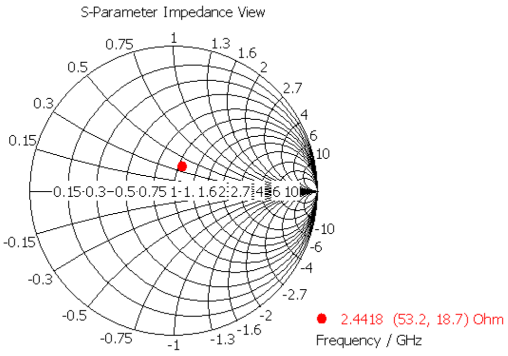

Figure 3.26a: Impedance (Smith Chart)

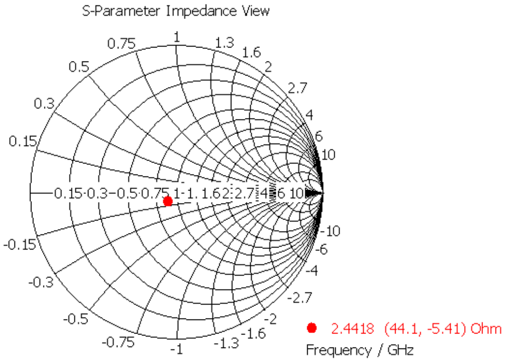

Figure 3.26b: Impedance (Smith Chart)

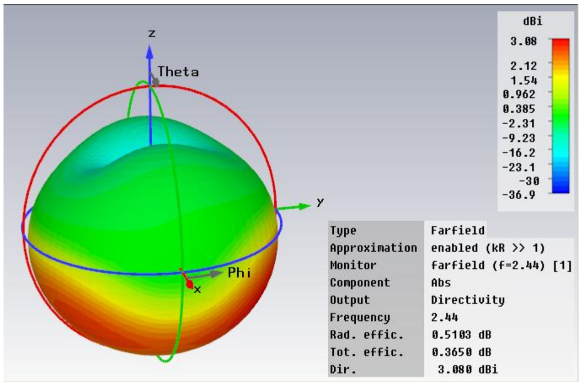

Type	Farfield
Approximation	enabled (kR >> 1)
Monitor	farfield (f=2.44) [1]
Component	Abs
Output	Directivity
Frequency	2.44
Rad. effic.	0.5103 dB
Tot. effic.	0.3650 dB
Dir.	3.080 dBi

Figure 3.27a: 3-D Absolute Patterns

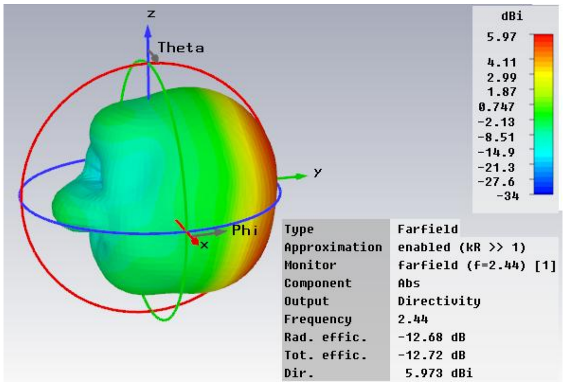

Type	Farfield
Approximation	enabled (kR >> 1)
Monitor	farfield (f=2.44) [1]
Component	Abs
Output	Directivity
Frequency	2.44
Rad. effic.	-12.68 dB
Tot. effic.	-12.72 dB
Dir.	5.973 dBi

Figure 3.27b: 3-D Absolute Patterns

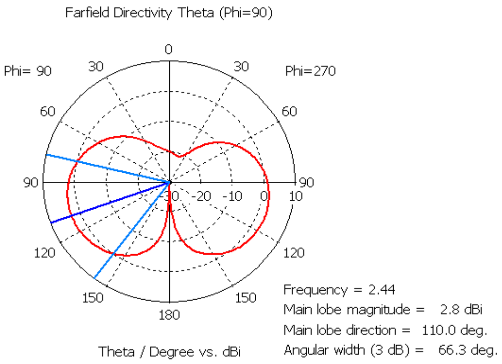

Frequency = 2.44
Main lobe magnitude = 2.8 dBi
Main lobe direction = 110.0 deg.
Angular width (3 dB) = 66.3 deg.

Figure 3.28a: 2-D CO-pol Component

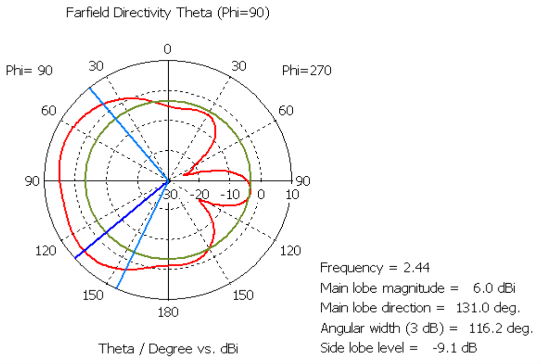

Frequency = 2.44
Main lobe magnitude = 6.0 dBi
Main lobe direction = 131.0 deg.
Angular width (3 dB) = 116.2 deg.
Side lobe level = -9.1 dB

Figure 3.28b: 2-D CO-pol Component

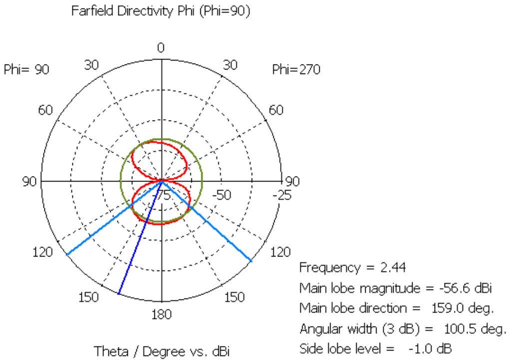

Frequency = 2.44
Main lobe magnitude = -56.6 dBi
Main lobe direction = 159.0 deg.
Angular width (3 dB) = 100.5 deg.
Side lobe level = -1.0 dB

Figure 3.29a: 2-D X-pol Component

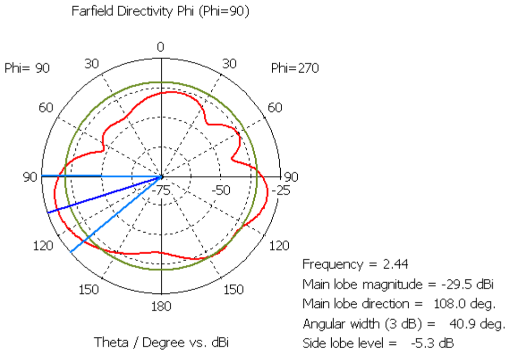

Frequency = 2.44
Main lobe magnitude = -29.5 dBi
Main lobe direction = 108.0 deg.
Angular width (3 dB) = 40.9 deg.
Side lobe level = -5.3 dB

Figure 3.29b: 2-D X-pol Component

Effect of Antenna Types EXTRA HUMUNGOUS dielectric (Thesis version 6).xls

Antenna Type	Environment	Nominal Pattern Shape	Simulated Directivities at Fc = 2.4418GHz (ISM-band)		
			Av. CO-pol Directivity (Dtheta) [dBi]	Av. X-pol Directivity (Dphi) [dBi]	Av. (CO/X)-pol Ratio [dB]
Rufa' (Figs 3.19 & 3.20)	Free-Space	Omnidirectional	1	-18	+19
	Onbody	Directional	-15 (Forwards) -25 (Backwards)	-15 (Forwards) -23 (Backwards)	0 (Forwards) -2 (Backwards)
Printed Monopole (Figs 3.25 & 3.26)	Free-Space	Omnidirectional	0	-57	+57
	Onbody	Directional	+6 (Forwards) -9 (Backwards)	-30	+36 (Forwards) +21 (Backwards)

Table 3.5: Effect of body on Simulated CO/X-pol Ratios for ‘Rufa’ and Printed Dipole Antennas (Dielectric Size (L x W x T) = (300mm x 200mm x 37mm) and Intervening Air Gap T_{airgap} = 2mm)

3.7 Using CST Simulated 3-D Patterns within Wireless Insite Simulations to Derive Overall System Performance

The ‘Wireless Insite’ software package, used later in Chapter 5 to derive overall system performance, permits antennas to be selected from a range of internally generated *generic* antennas types (for example half-wave dipoles).

However, of more use in the present context, is an alternative facility within this ‘Wireless Insite’ package whereby ‘User Defined Patterns’ can be imported which represent the characteristics of *specific* antenna patterns. This allows the effect of ‘real-life’ antennas on the overall system performance to be assessed.

Sub-section 3.7.1 following considers the detailed requirements of ‘User Defined Antenna’ data to permit its use in the ‘Wireless Insite’ (WI) software package.

3.7.1 ‘Wireless Insite’ Requirements for ‘User Defined Antenna’ Pattern Data

As indicated above, in order to use the User Defined Antenna facility (which only functions correctly in version v2.5 of the WI package and later), WI requires the antenna pattern data to be in a specific format.

In particular, this pattern data must specify the *three*-dimensional Antenna Pattern in terms of its gain and, where necessary (as here), its phase for two orthogonal components in the elevation (θ) and azimuth (ϕ) directions. Thus, for each angular direction (θ,ϕ), four parameters (G_θ & G_ϕ) plus ($phase_\theta$ & $phase_\phi$) are required.

Further, θ & ϕ must also be specified in *fixed increments* for Wireless InSite to enable it to interpolate more readily to accurately derive gains for signals in specific directions between these specified values.

Unfortunately, the *measured* pattern data here is only *two*-dimensional, since a turntable rotating in the azimuth plane only was available. Full 3-D pattern measurements would require an azimuth-over-elevation antenna mount; a facility which was not available at the time of measurement. Further, the angular increments involved in pattern *measurements* are not inherently fixed, as required by Wireless InSite, although post-processing interpolation could be used to derive these.

However, the CST *simulated* on-body ‘Rufa’ patterns *are* available. Further, these are *three*-dimensional and have gains and phases at fixed increments of elevation and azimuth angle (θ,ϕ) as required. Also, now that a larger dielectric sandwich has been used, which is more representative of the human body, the resulting simulated patterns now have a realistic measure of body blockage when the patient/client is located such that their body gives rise to a Non Line Of Sight (NLOS) link propagation condition.

As a direct consequence, the *simulated* 3-D (rather than the measured 2-D) pattern data was chosen for importation into the subsequent Wireless InSite system model described later in Chapter 5.

3.8 Effect of Reducing *Overall* Size of *COTS 'Rufa' Antenna*

The RF performance in the 2.4GHz ISM band of the tiny (15mm x 5mm x 1mm) 'Rufa' antenna chip, when mounted on its associated (50mm x 21mm) Evaluation Board, was shown earlier to perform more than adequately when located *on*-body for the proposed Telecare/Telemedicine sensor applications. Of this (50mm x 21mm) total area, (46mm x 21mm) represents the areas of its top and bottom ground-planes, which are the key board components here as regards the antenna's RF performance.

However, the 50mm length of the *total* antenna assembly size here might be considered rather large for everyday on-body sensor applications. So, an investigation was conducted to determine the extent to which the length of this standard Evaluation Board could be reduced, without significantly degrading the antenna's overall RF characteristics. This was done by means of simulations, whose predictions would need to be validated by measurements on a resulting optimally sized prototype.

So, the original CST simulation model of the full-sized 'Rufa' antenna assembly was modified to allow the length of the ground-plane elements within the Evaluation Board to be a variable. Evidently, the length of the CPW feed-line within this ground-plane also had to vary in accordance.

The 46mm long ground-plane component within the original 50mm long Evaluation Board was reduced in three stages to 31mm, 26mm and 21mm, corresponding to reductions of 67%, 57% and 46% respectively. Such reductions tend to degrade the match of the antenna to its 50Ω feed-line; so, to improve this, a small series-capacitor (typically 3pF) was inserted in the feed-line, at the antenna chip end, to offset the otherwise inductive element within the resulting impedance.

Figure 3.30 shows a CST model of the original 'Rufa' chip antenna chip mounted on a miniaturised version of the standard Evaluation Board whose length is now only 21mm. This figure also shows the dielectric sandwich here used to emulate the nearby body (1mm away here).

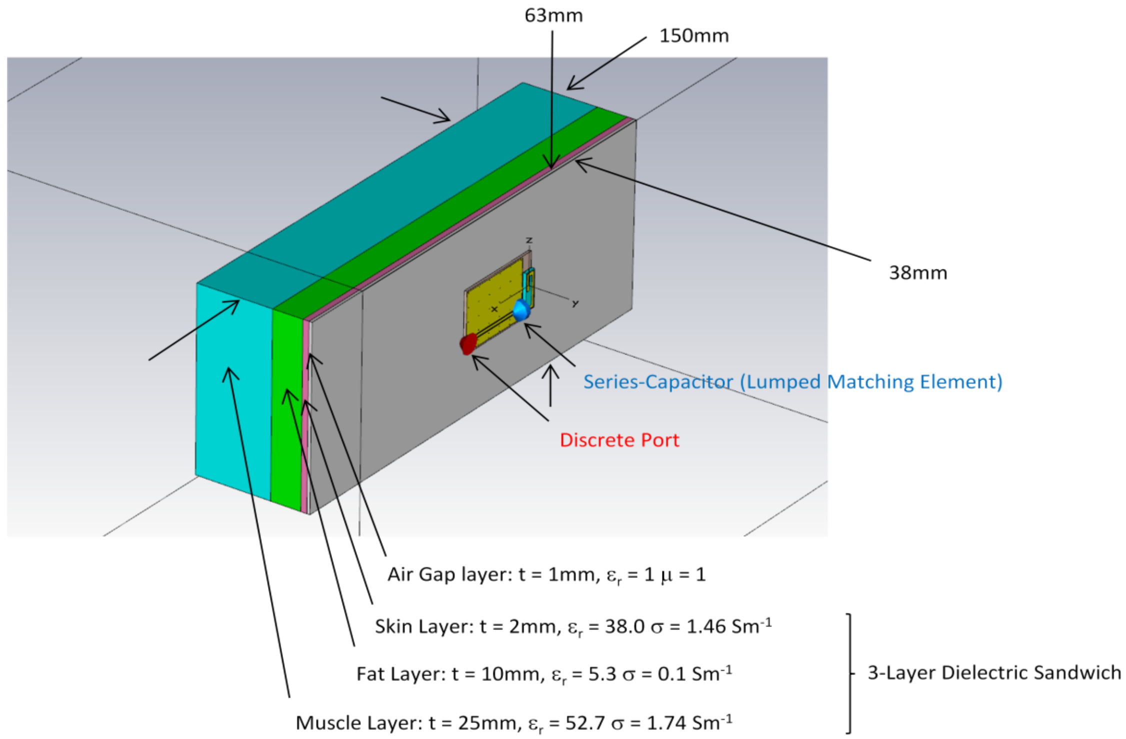

Figure 3.30: CST Model of *Miniaturised* Antenova's 'Rufa' COTS Antenna Located at 1mm above the Dielectric Sandwich/Body

The results for this smallest ground-plane length of 21mm (a 46% reduction) are given in Figures 3.31 to 3.33.

Figure 3.31 below shows that the f_c = 2.441GHz centre frequency, here, is well matched to f_c = 2.442GHz required for the ISM band. Further, with the 2.26pF series capacitor used for matching purposes here, the Δf_{-10dB} = 68MHz = 2.8% bandwidth is nearly adequate to satisfy the Δf_{-10dB} = 84MHz = 3.4% bandwidth required to cover the complete ISM band.

Figure 3.32 overleaf shows the *simulated* impedance of the antenna assembly in this *on-body* environment at f_c = 2.4482GHz centre-frequency, showing that its complex impedance is now $Z_0 = (28 + 4j)\Omega$. This is not very close to the nominal 50Ω quoted in Antenova's specification sheet [21] for their *full-sized* antenna assembly in *free-space*. However, the imaginary part of Z, which is inductive here, could be partially offset, by replacing the simple Series-C 2.26pF capacitor currently in the matching network with a slightly more complex LC network.

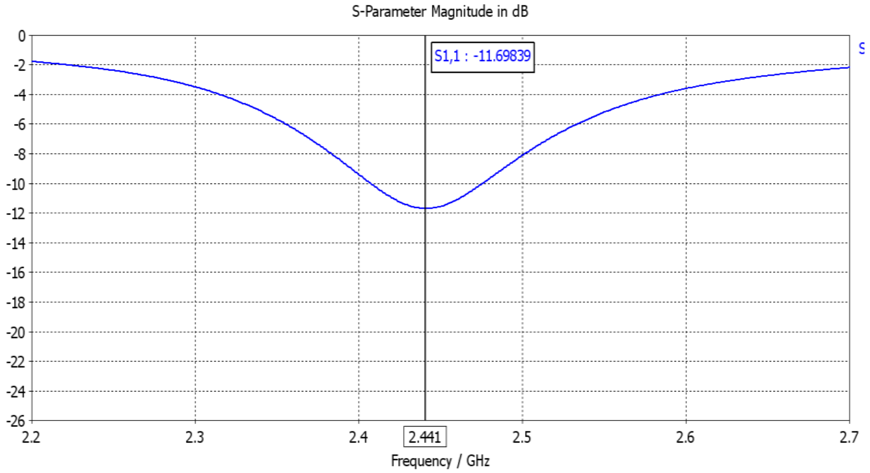

Figure 3.31: *Simulated* S11 versus frequency in *On-Body* Environment for Miniaturised (21mm ground-plane length) Antenova's 'Rufa' COTS Antenna Located 1mm above the Dielectric Sandwich/Body

The appropriate values for these LC components were computed using the standard technique on the assumption that the antenna chip impedance in the absence of any matching network was $Z_0 = (28 + 4j)\Omega$. However, the ensuing match was disappointing, being far from optimum. It is believed that this is because this $Z_0 = (28 + 4j)\Omega$ value is not the true impedance of the antenna chip, but rather the *apparent* impedance of the antenna chip *as seen at the end of the feed-line to which it is attached*.

Evidently this LC matching exercise could be performed again with the true *antenna chip* impedance and it is expected that, with the ensuing more optimum match, the current bandwidth of Δf_{-10dB} = 68MHz = 2.8% might be extended to more fully satisfy the Δf_{-10dB} = 84MHz = 3.44% bandwidth required to cover the full ISM band. Evidently, this is of key interest as it would confirm that the existing 'Rufa' antenna assembly can indeed be miniaturised to be half its current length and still fulfill the complete RF requirement.

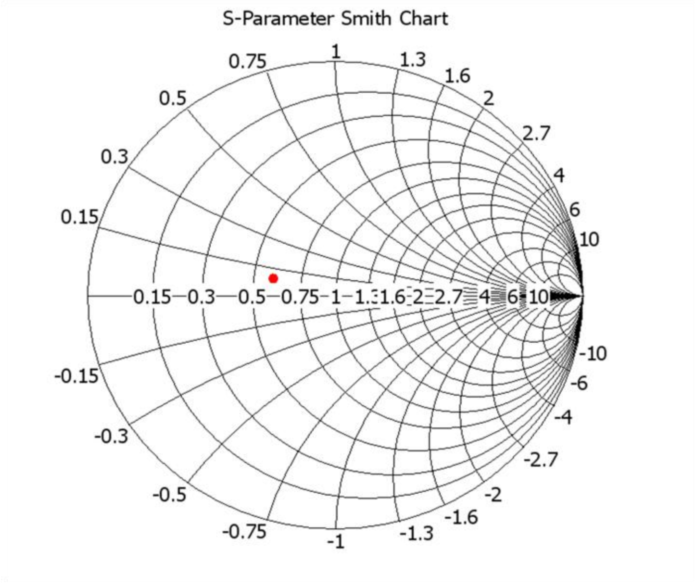

$$Z = (28 + 4j)\Omega$$

Figure 3.32: *Simulated* Impedance at fc = 2.4482GHz in *On-Body* Environment for Miniaturised (21mm ground-plane length) Antenova's 'Rufa' COTS Antenna Located 1mm above the Dielectric Sandwich/Body

Finally, for the sake of completeness, the effect of different values of capacitances in the simpler series capacitance-only type of matching network was investigated. The results are shown in Figure 3.33 overleaf, confirming that the optimum value in this simple matching scheme is indeed 3.26pF. Figure 3.33 also illustrates just how closely the miniaturised antenna, having a reduced 21mm length ground-plane, comes to matching the frequency coverage from 2.400 to 2.484GHz required for the complete 2.4GHz ISM band with this optimum capacitance value.

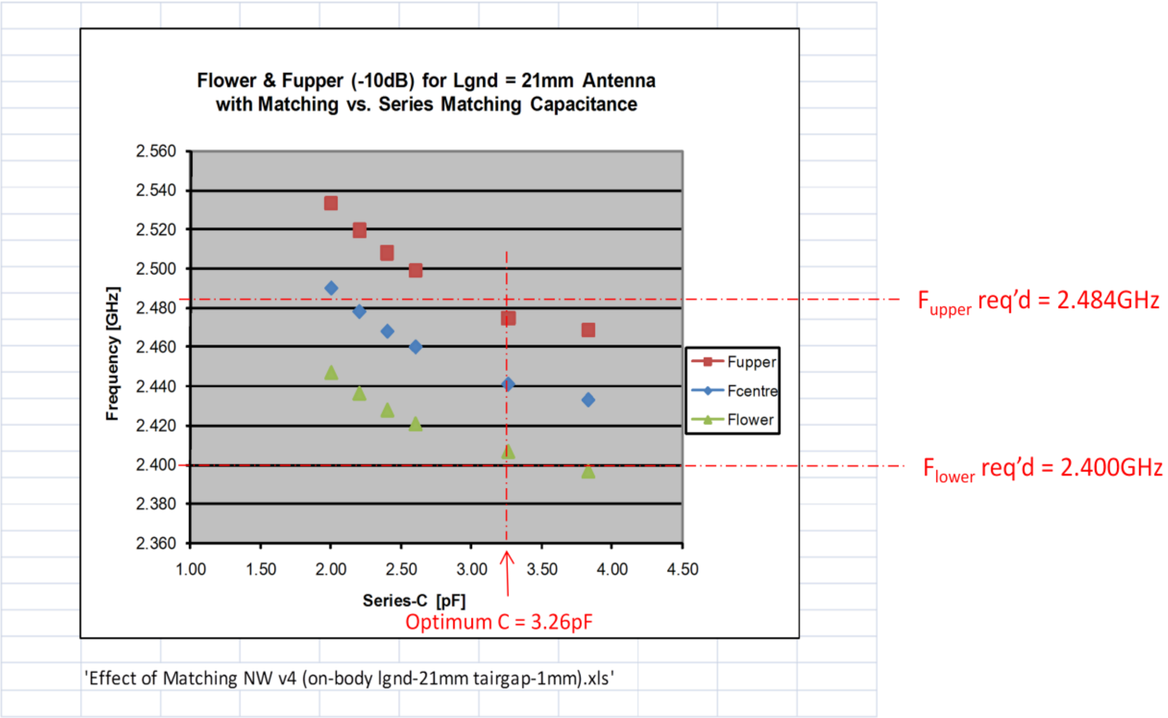

'Effect of Matching NW v4 (on-body lgnd-21mm tairgap-1mm).xls'

Figure 3.33: *Simulations* Showing the Effect of Varying the Capacitance in a Simple Series-C Matching Network in *On-Body* Environment for Miniaturised 'Rufa' COTS Antenna Located 1mm above the Dielectric Sandwich/Body

Measurements, to confirm the simulations above of the effect of reducing the size of the Evaluation Board have yet to be carried out. Clearly, however, it is important that these measurements on miniaturised prototypes of the existing 'Rufa' antenna assembly *are* conducted to confirm that this considerable potential miniaturisation as predicted by this simulation exercise can indeed be realised in practice.

Therefore, in conclusion, this simulation exercise indicates that a potentially useful halving of the length of the complete antenna assembly size from 50mm down to 25mm, resulting in overall (L x W x T) = (25mm x 21mm x 2mm), should still give acceptable RF performance.

3.9 *Un*anticipated Effect of Human Body on Mutual Coupling between a *Pair* of Closely Spaced 'Rufa' Antennas

3.9.1 Introduction

The second *un*anticipated effect of the body in close proximity to the 'Rufa' antenna is the significant reduction in mutual coupling between a *pair* of such antennas, which are located closely side by side, each the same polarisation. This was observed in the present study in both CST simulations and measurements, and was reported by the author at EuCAP 2011 [20].

However, towards the end of this study, it was found that the same effect had been reported in an earlier reference [19]. Consequently, the present author's contribution in this respect can no longer claimed to be novel, but nonetheless remains a useful independent confirmation of this earlier result. Both references [73] and [25] demonstrate a mutual coupling *reduction* in excess of 10dB, even for an antenna pair with only ($\lambda_0/5$) separation (where λ_0 is the wavelength in free-space).

3.9.2 Reduction in S_{21} – *Simulated* Results

Figure 3.34 shows the pair of COTS antennas in the CST simulation for two cases where:

i) The pair of antennas share a *common* Evaluation Board,
ii) Each antenna has its own *individual* (50mm x 21mm) original size Evaluation Board.

Case ii) was found to give much lower mutual coupling than case i); possibly because coupling by means of Surface Wave propagation is more limited due to the presence of the break between the two individual Evaluation Boards in (ii).

CST simulations, for case (ii) with individual Evaluation Boards, were conducted for the free-space and on-body cases to derive the on-body reduction as shown in Figure 3.35. The reduction in excess of 10dB in the mutual coupling between the two antennas here can be clearly seen, even for antennas as closely-spaced as ($\lambda_0/5$). Confirmatory mutual coupling *measurements* were also made for the on-body case and are included in Figure 3.35 (grey triangular points). These can be seen to be in good agreement with the corresponding *simulated* on-body results.

The present author's finding [20] that the mutual coupling between a pair of unshielded COTS antennas is significantly reduced with respect to its free-space level when used in close proximity to the human body is also referred to in reference [27].

Now reference [27] correctly states that excessive mutual coupling between the multiple antennas used at both the on-body node and off-body node, to implement MIMO techniques to enhance link capacity, will significantly degrade this capacity enhancement.

However, reference [27] then proceeds to assert that this reduction in antenna spacing for a given level of mutual coupling, is likely to permit a smaller *on*-body multiple element MIMO solution, for a given degradation of capacity enhancement, than would be realisable in free-space. If so, this potential benefit would enhance user-acceptability of such multi-element on-body nodes.

However, this latter assertion is not entirely self-evident because:

i) Although it is well established that excessive mutual coupling degrades the independence of signals otherwise present at two antenna elements, it not self-evident that reduced coupling can *improve* it if there is insufficient *spatial* separation between them to give the required independence in the first place.
ii) In addition, for the miniature on-body node(s) considered here, the *whole* node effectively becomes the antenna so that the overall performance improvement arises as a result of a complex combination of the resulting spatial, polarisation and pattern diversity.

Thus, to exploit this effect, a more definitive understanding of the composite effect of the many mechanisms involved here is needed. However, because of its potential benefit, it is recommended as a worthwhile topic for further consideration under the heading of Suggested Further Work in section 6.2.

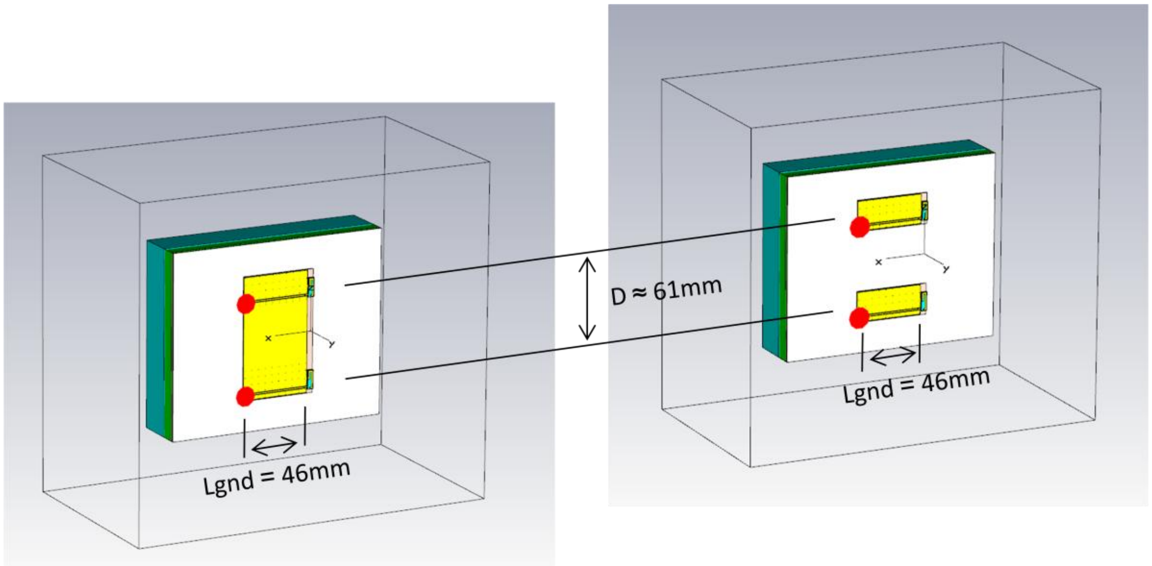

Case i) Case ii)

Figure 3.34: Mutual Coupling between Antenna Pairs (with D = 0.5λ_0 separation here) having Common & Separate Evaluation Boards with GND-planes

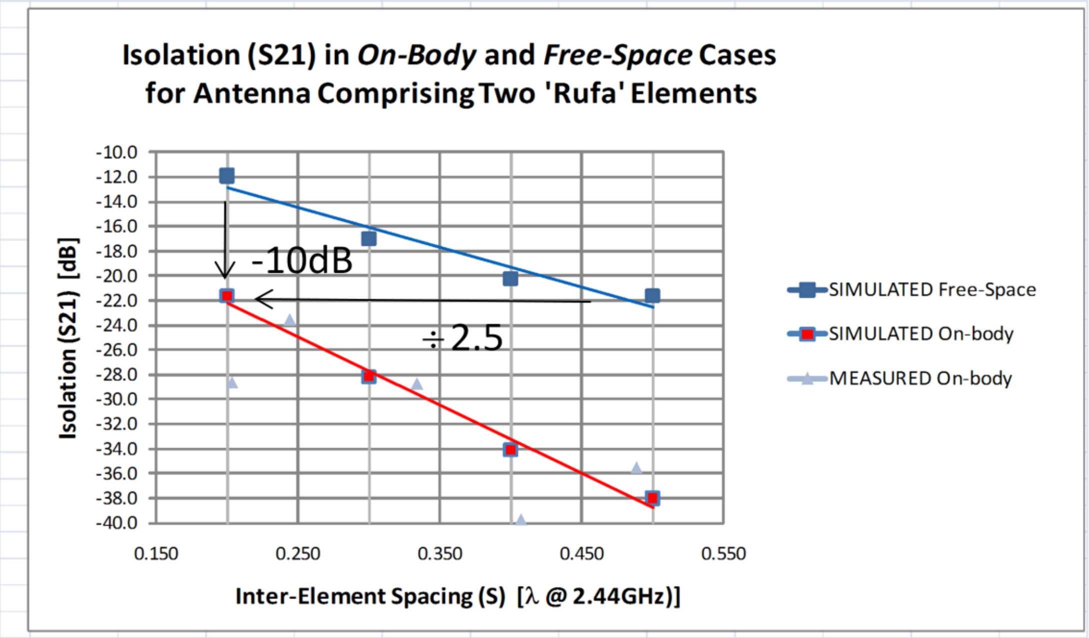

'Effect of inter-element separation (on-body vs. free-space) v0_4_corr.xls'

Figure 3.35: Mutual Coupling versus Spacing between Antenna Pairs in Free-Space and On-body for Case (ii) in Figure 3.34.

3.10 Conclusions

To summarise, therefore, key effects of the presence of a nearby body on the RF Properties of a *single* COTS candidate ‘*Rufa*’ antenna are:

a) An unacceptable level of detuning, when the ‘Rufa’ antenna is in *direct* contact with the body.
b) A drastic efficiency reduction (~19dB), when the ‘Rufa’ antenna is in the immediate vicinity of the body.
c) A depolarising effect, whereby the co/x-polar ratio of the ‘Rufa’ antenna is reduced by 19dB from +13dB in Free-Space to about -6dB when located on-body.

Now it was shown that the ‘Rufa’ antenna detuning effect can be limited to an acceptable degree by the simple expedient of spacing the antenna about ~3mm away from the body. Fortunately, this small spacing does not detract significantly from the desirable low-profile characteristic of the ‘Rufa’ antenna.

However, no equivalent obvious method was discovered to address the drastic on-body antenna efficiency reduction, which would compromise the overall system performance in the presence of deep multipath fading. Instead, diversity techniques must be implemented to mitigate the deepest multipath fades so that this on-body inefficiency can be tolerated. The efficacy of spatial and polarisation diversity techniques to do this are investigated, as detailed later in Chapter 5 where *overall system* aspects are addressed.

The effect of antenna depolarisation, produced by the presence of the body, has, in turn, been found to have a slightly adverse effect on the off-body diversity-gain necessary to mitigate the otherwise troublesome multipath fading. This is described in detail in Chapter 5 where the *overall system* performance with an on-body ‘Rufa’ antenna is quantified for both types of off-body diversity scheme.

Preliminary *simulations* of an alternative unshielded antenna type to the ‘Rufa’ candidate COTS antenna investigated in depth here were conducted using a simple printed monopole antenna type. These demonstrated that this example printed monopole type of antenna also experiences a depolarisation effect of similar extent (~20dB) when in close proximity to a representative body sandwich. However, because the printed monopole antenna had a much higher CO/X-pol Ratio in free-space than the ‘Rufa’ antenna to start off with, the resultant CO/X-pol Ratio on-body still remains >0dB for this monopole antenna type. Thus, the depolarising effect of the nearby body is not unique to the ‘Rufa’ antenna.

Although only a single alternative type of antenna was investigated, this shows that the depolarising effect of the body is not specific to the candidate ‘Rufa’ antenna. This, plus the more generic analysis reported later in Chapter 4, suggests that the body’s depolarisation effect is more generic and might be expected to apply to other unshielded antenna types.

The current 50mm long Evaluation Board associated with the ‘Rufa’ antenna chip may be useful to accommodate a considerable number of transceiver components in addition to the antenna chip. However, if all this board area is not required and a reduction in the overall on-body node is desirable, simulations have shown that a useful halving of the current overall length from 50mm down to 25mm is possible without significantly affecting the ‘Rufa’ antenna’s S-parameter performance.

Finally, the presence of a body in close proximity to a *pair* of closely-spaced candidate COTS ‘Rufa’ antennas has been investigated. This was shown to produce a reduced mutual coupling between them when compared to that experienced in free-space by this pair with the same *physical* separation. Alternatively, the antenna pair can be spaced closer together physically, when on-body than in free-space, for a specified level of mutual coupling. However, further work would be needed to isolate the physical cause for this effect and also whether (or not) it can be exploited to miniaturise multi-element on-body antennas without adversely degrading the potential capacity enhancement that such a MIMO antenna configuration would otherwise afford.

Chapter 4

An Analytical Approach to the On-body Depolarisation Effect

4.1 Introduction

The author's PhD study of low-cost 2.4GHz wireless links for applications such as Telecare and Telemedicine makes use of a particular miniaturised low-cost COTS antenna at the on-body nodes. The candidate antenna used here is Antenova's 'Rufa'™ antenna, which is specified as having a largely omnidirectional Far-Field pattern in Free-Space (FS). However, the pattern actually realised will vary considerably according to the real-life environment in which it is used.

In particular, as detailed previously in Chapter 3, during this study it was discovered that the (otherwise) reasonably polarised Free Space patterns of this COTS antenna become almost completely depolarised when it is relocated to be in close proximity to the body.

Literature searches failed to uncover any previous observation of this depolarisation effect, which was reported recently by the author at EuCAP 2011 in [20]. So, at that time, no physical mechanism to account for this effect could be given.

It *is* noted that Hall et al. [73] consider the effect of a nearby horizontal dielectric slab on the fields of a horizontal short-dipole in terms of the different resulting surface-wave propagations in orthogonal directions on the surface of the dielectric slab. However, following further consideration, it was concluded that this mechanism will give rise to different far-fields patterns on different pattern cuts, rather than different co-polar and x-polar responses on a common azimuthal cut which is of interest here.

Other references regarding surface-wave propagation were also consulted, but these did not shed further light on mechanism(s) which would account for the depolarisation effect. Nonetheless, these are included here in the References section as references [74] and [75] for potential future use.

Consequently, consideration of (the more esoteric) surface-wave propagation mechanisms was temporarily shelved, and attention redirected towards mechanisms involving more conventional space-wave propagation based on a Geometrical Optics approach.

4.2 Use of Modified Geometrical Optics to Explain On-Body Depolarisation Effect

This short sub-section considers the validity of using Geometrical Optics (GO) to analyse the depolarising effect of the human body on (otherwise reasonably polarised) antennas which were designed primarily for free-space use.

Conventional GO assumes propagation by means of Uniform Plane Waves (UPWs) with associated 'rays' normal to these wavefronts, giving 'ray-bundles' which are parallel. This is only applicable for Far-Field (FF) ranges (R) (where $R >> 2.D^2/\lambda$ [76]) of structures whose largest dimension (D) is considerably larger than the electromagnetic wavelength (λ) involved. Thus, for the present case, for an ideal half-wave dipole antenna where $D \approx (\lambda/2)$ in the immediate vicinity ($\lambda/40$) of a human body, a *conventional* GO approach involving UPWs is *un*likely to be valid.

Instead, therefore, a modified version of GO analysis, formulated by the present author, was used here which does not constrain itself to the conventional case of UPWs. Rather, it adopts a more generic approach; assuming wavefronts which are still defined as surfaces of constant phase [102], but that are now associated with *non*-parallel 'ray-bundles' [77].

This chapter will then proceed to show that this *modified* GO analysis provides a result for the *change* in *average* co/x-polar ratio parameter due to the proximity of the body (a reduction of 19.5dB) that is in remarkable agreement with the measured reduction in this average parameter and that provided by CST simulation (both being 19dB, as reported earlier in Section 3.5.1). Now, it is acknowledged, as pointed out in reference [78], that this agreement could be fortuitous and does not *conclusively* prove that the physical mechanisms assumed to derive this result are those actually taking place.

Nonetheless, it is believed that analysis of the specific antenna structure considered here, using this *modified* GO approach, provides a relatively simple physical model which (at the very least) *emulates* the physical processes occurring to surprisingly good accuracy. On these grounds, therefore, this analysis is considered worthy of inclusion here and possibly worth pursuing more rigorously at a later date; if only to investigate its potential for wider application.

Considerations of symmetry for the ideal thin-wire dipole antenna assumed in the analysis here dictate that (in the absence of other nearby objects) wavefronts in its immediate vicinity must be cylindrical [79]. Evidently, these surfaces of constant phase are circular around the dipole axis and constant along its length. As for any antenna, the wavefronts in its immediate vicinity (here cylindrical) become spherical at intermediate ranges and eventually tend to UPW's at extreme ranges.

In effect, the analysis is exploiting a Huygens Wavefront Reconstruction approach, as described in references [80] and [81], to allow the development of the wave front at waypoints as it progresses along the route from the source to a hypothetical plane located at a convenient point in space to be visualised. The analysis allows a description of the illumination of this hypothetical plane to be computed in terms of the phases and amplitudes for individual elemental areas on this plane.

Although relatively simple in concept, such an approach is remarkably general in that it does not assume anything regarding the structure of the source or the media within which the wavefronts propagate other than their basic electromagnetic properties and physical shapes must be *known*. In particular, it makes no reference to the structure's *electrical* size and is therefore independent of frequency. However, it is accepted that the geometrical complexity of most structures is likely to preclude its practical use in all but the simplest cases such as that considered here.

The analysis here takes into account the way in which, on the basis of conservation of flux density, the varying divergence of rays within different local ‘ray-bundles’ impacts on the flux density impinging on associated elemental areas on the hypothetical plane.

The analysis then proceeds to include an approximate representation of the nearby human body, by means of a simple dielectric slab, to investigate how amplitudes and phases of wavefronts produced by reflections from this representative body combine with those originating directly from the source to produce the total amplitudes and phases on the incremental areas for the combined (source plus nearby body) structure.

In principle, the resulting far-field patterns of the combined structure could be derived by means of a Fourier Transform (FT) of the total amplitudes and phases of the individual local areas on the hypothetical plane [82]. However, because both polarisations involve identical paths (and therefore phases), it is argued here that, to first approximation, the co/x-polar *ratio* in the far-field will be similar to those experienced for the individual elemental areas on the common hypothetical plane from which both polarisations originate. So, to first approximation, this final FT step has been omitted here as being unnecessary for the present purpose.

4.3 Further Consideration of Analysis of Antenna Depolarisation Effect

For simplicity, a pseudo 3-D analysis was formulated which was implemented using MATLAB; the resulting coding being given here as Appendix A3. This model, involving a relatively rigorous analysis in 2-D, is extended by appropriate simple assumptions to give an approximate 3-D analysis that is required to represent the real-life situation.

For the purposes of simplicity, it is assumed in this analysis that the body can be adequately represented by an *equivalent,* single, isotropic dielectric slab. Further, this ‘slab’ is assumed to be flat and of large extent in comparison to the dimensions of the associated small on-body antenna.

The assumptions regarding size and flatness of this slab are more likely to be applicable to a miniature antenna located in close proximity to *larger* parts of the body. However, it is less likely to be valid for smaller parts of the body at the 2.44GHz frequency assumed in the analysis here.

The single slab assumption is often taken to emulate the properties of a multi-layered dielectric sandwich structure in terms of an equivalent single layer whose effective permittivity and conductivity can be expressed as a function of the permittivities, conductivities and thicknesses of the individual constituent layers [83] & [84] within the dielectric sandwich structure. Interactions arising as a result of rays transmitted to (and reflected from) subsequent interfaces between lower layers in a more realistic dielectric *sandwich* are ignored here. It is reasoned that their inclusion will give rise to second-order effects, but these would considerably complicate the analysis without significantly affecting the main arguments presented here. Nonetheless, the validity of this single slab assumption being truly representative of a multi-layer structure remains a simplification which needs to be borne in-mind.

A conventional geometric optics (GO) approach [85] & [86] given in terms of Uniform Plane Waves (UPW) with parallel associated ‘rays’, would require the reflecting surface (the body, here) to be in the Far-Field (FF) of the associated antenna. Clearly, this is not the case here, where the antenna is located only 3mm ($\cong (\lambda_0/40)$ at 2.44GHz) away from the body. Instead, the body here is in the Near-Field (NF) of the small dipole antenna, where the wavefronts are of cylindrical shape [86].

Thus to address the non-planar wavefronts in this NF region, a generic Huygens Wavefront Reconstruction approach [80] is adopted here, in which energy within small increments (ΔAoA = 1°) of solid-angle emanate from this antenna source. These impinge on the planar dielectric slab, illuminating specific incremental areas there. The Huygens Wavefront Reconstruction approach then assumes that these small illuminated areas can be regarded as secondary sources, each of which emits radiation having spherical wavefronts. The different amplitudes and phases of these indirect secondary sources can then be combined (along with the direct emissions from the antenna source) at points where they intersect on an illumination-plane located at an arbitrary distance from the antenna. A 2D cross-section of the 3D geometry for an *individual* ‘ray’ (typical of multiple rays within the various diverging ‘ray-bundles’ simulated here) at an associated Angle of Arrival (AoA) is shown in Figure 4.1 overleaf.

If this illumination plane is in the NF of the antenna, then the FF patterns due to the composite signal could be derived by taking the 2D Fourier Transform of the illumination (phase and amplitude) on this plane. However, it is believed that this step is not required for the present purpose of deriving the CO/X-polar ratio, as discussed later.

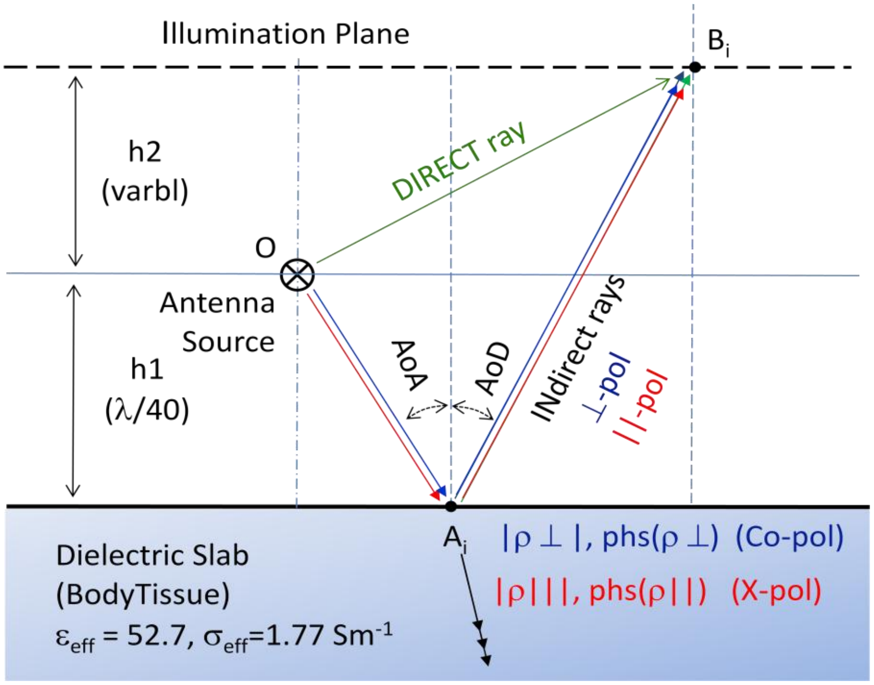

Figure 4.1: Geometry of Rays Involved in Geometric Optics Analysis here Showing Typical *Direct* and *In*direct Rays Emanating from a Common Source at O and Converging at a Common Point B_i on the Illumination Plane

This analysis is carried out independently for the two orthogonal polarisations; one for which its E-vector is parallel (||) to the incident plane containing the incident ray, the reflected ray and the normal to the reflecting surface, the other having its E-vector perpendicular (⊥) to this incident plane.

4.4 Further Details and Results of MATLAB Model

In most texts, including [85] and [86], analyses are given in terms of an incident ray impinging on a *horizontal* dielectric interface, giving a vertical incident plane, as depicted by the present author in Figure 4.2 below. Analysis in this case would involve computing the complex refection coefficients for different *elevation* angles of arrival (AoA) of the incident rays.

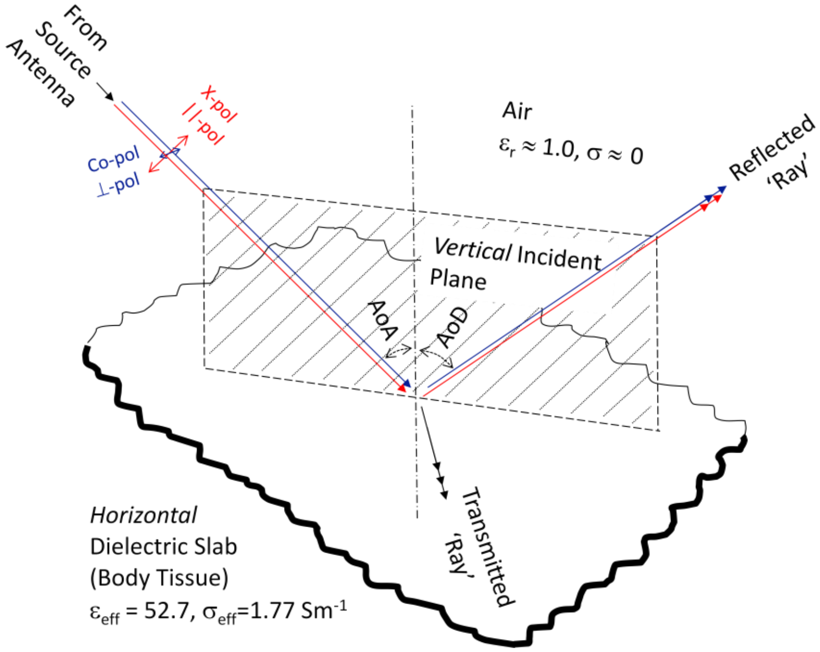

Figure 4.2: Showing Typical Rays Involved for Reflection from a *Horizontal* Dielectric Surface (As Appearing in most Texts)

However, in the on-body case of interest here, the incident ray impinges on a *vertical* dielectric interface, giving a horizontal incident plane, as depicted in Figure 4.3 overleaf. Consequently, the analysis here involves computing the different complex reflection coefficients for the range of *azimuthal* AoA's of the incident rays (0° to 90°) as those of the measurements and CST simulations reported previously.

The main purpose of Figure 4.3 is to establish at the outset that the *co*-polar component of the incident ray corresponds to the component which is perpendicular (⊥) to the incident plane, whilst the *x*-polar component of the incident ray corresponds to the component which is parallel (||) to this plane. This is important because these orthogonal components are analysed independently and it is essential to know the correspondence between them to allow the resultant co/x-polar ratio to be correctly determined during the final stage of the analysis.

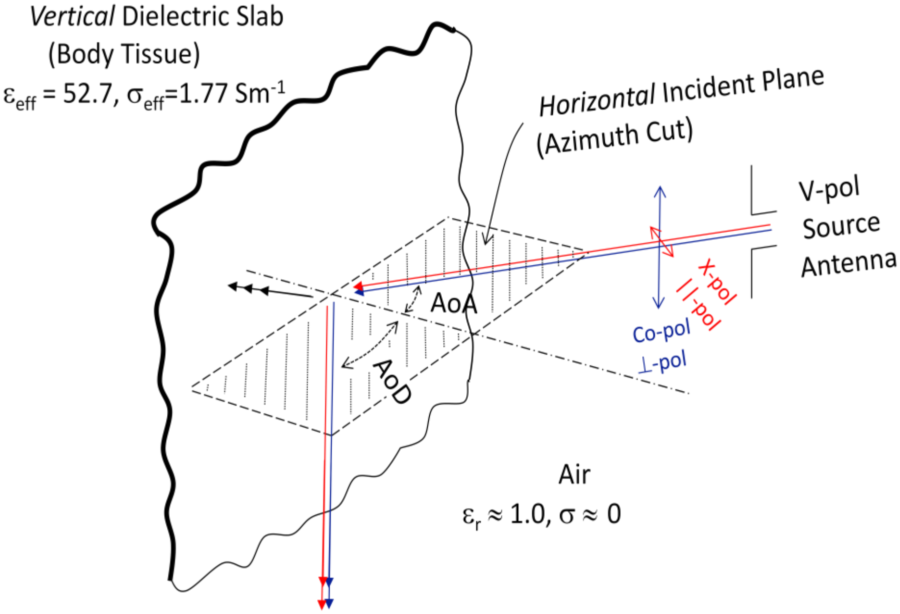

Figure 4.3: Showing Typical Rays in the On-Body Case here, where Reflections from a *Vertical* Dielectric Surface are Involved (as Assumed for the Present Applications)).

The frequency used in all the figures presented here is the centre frequency of the 2.4GHz ISM-band, which is f_c = 2.44175GHz. However, since the geometry of the model is formulated in terms of wavelength, any frequency can easily be investigated by simply changing this parameter, which is stored as a programme constant in the MATLAB analysis here.

Likewise, *effective* ε_{eff} = 52.7 and σ_{eff} = 1.77Sm^{-1} are assumed in all the figures here, as being representative of typical body tissue as given in [84] However, again, these can easily be varied by simply changing these parameters, also stored as programme constants. In fact, this was done earlier on when writing the MATLAB programme to validate this part of it by comparison with previously published plots of complex reflection coefficients, which use different f_c, and effective ε_{eff} and σ_{eff} values from those here.

As previously mentioned, Figure 4.1 illustrates the geometry of the 'ith' individual direct and indirect typical ray-pair converging at a common point B_i for a specific Angle of Arrival (AoA) and Angle of Departure (AoD), where AoA = AoD. Two routes, involving 3 paths from O to B, can be seen for:

(i) the direct ray on the direct route (path OB_i), and

(ii) the indirect ray on the indirect route (paths OA_i and AB_i).

The orthogonal perpendicular and parallel polarisation components for the various rays are shown in blue and red respectively; as are the corresponding amplitude reflection coefficients and phases at A_i.

Simple application of the law of cosines [87] for the geometry of the 'ith' direct ray shown in Figure 4.1, gives the path length (PL) involved for this:

$$PL_{\underline{direct}} = \sqrt{(A_iO^2 + A_iB_i^2 - 2*OA_iA_iB_i*\cos(2*AoA_i))}. \tag{4.1}$$

Now, it is also evident from this figure that:

$$A_iO = h_1/\cos(AoA_i) = h1*\sec(AoA_i), \quad \text{and}$$

$$A_iB_i = (h_1 + h_2)/\cos(AoA_i) = (h_1 + h_2)*\sec(AoA_i).$$

Hence, upon insertion in (4.1) and some trignometrical manipulation, these give:

$$PL_{\underline{direct}} = \sqrt{((2*h_1 + h_2)^2*\sec^2(AoA_i) - 4*h_1*(h_1 + h_2))}. \tag{4.2a}$$

In addition, Figure 4.1 also shows that the path length for the indirect ray is given by:

$$PL_{\underline{in}direct} = (OA_i + A_iB_i) = h_1*\sec(AoA_i) + (h_1 + h_2)*\sec(AoA_i)$$

$$= (2*h_1 + h_2)*\sec(AoA_i). \tag{4.2b}$$

The path lengths for the direct and indirect rays, given by (4.2a) and (4.2b) respectively, are shown plotted vs. AoA for $h_1 = h_2 = (\lambda/40)$ in Figure 4.4. This confirms that, as required, the path length for the indirect ray is always larger than that for the direct ray. Also as expected, the *difference* in path lengths for these two rays is a maximum ($\lambda/20$) when AoA = 0°, and tends to zero as AOA tends to 90°.

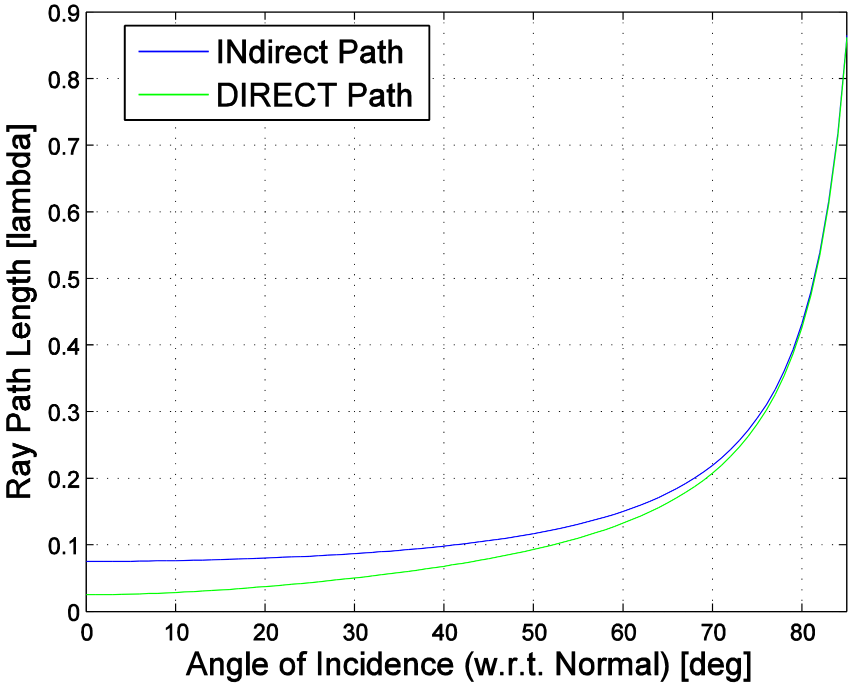

Figure 4.4: Path lengths involved for direct and indirect rays for $h_1 = h_2 = (\lambda/40)$

From equation (4.2a), the total phase lag of the direct ray at the common point B, with respect to that at O, is given simply by:

$$phs_{\underline{direct}} = (2\pi/\lambda)*(\sqrt{((2*h_1 + h_2)^2*\sec^2(AoA) - 4*h_1*(h_1 + h_2))}) \qquad (4.3a)$$

It is noted that this phase lag for the direct ray is independent of its polarisation, since it arises from the path-length involved alone (which is common to both polarisation components) and involves no reflection.

However, the corresponding total phase lag of the indirect ray at B is given by:

$$\mathrm{phs}_{\underline{\mathrm{in}}\mathrm{direct}} = (2\pi/\lambda)*((2*\mathrm{h1} + \mathrm{h2})*\sec(\mathrm{AoA})) + \mathrm{phs}(\rho) \qquad (4.3b)$$

where, $\mathrm{phs}(\rho)$is the extra phase change introduced in the reflection process at the dielectric slab for this indirect path, in addition to that due to the path length also involved.

Now this complex reflection coefficient (ρ) depends on the electrical properties of the dielectric slab (its effective permittivity (ε_r) and conductivity (σ)), the AoA of the indirect ray and whether the incident ray is polarised parallel ($||$) or perpendicular ($\perp$) to the incident plane. The resulting complex reflection coefficients for these two orthogonal polarisations are given in [86] as:

$$\rho_{||} = \{(\varepsilon - j*\chi)*\sin\alpha - \sqrt{}((\varepsilon_f - j*\chi) - \cos^2\alpha)\} / \{(\varepsilon - j*\chi)*\sin\alpha_i - \sqrt{}((\varepsilon - j*\chi) - \cos^2\alpha)\} \qquad (4.4)$$

$$\rho_{\perp} = \{\sin\alpha - \sqrt{}((\varepsilon - j*\chi) - \cos^2\alpha)\} / \{\sin\alpha - \sqrt{}((\varepsilon - j*\chi) + \cos^2\alpha)\} \qquad (4.5)$$

where, α_i is the grazing angle involved here i.e. the *tangential* angle of arrival at the horizontal slab. This is simply related to the *normal* angle of arrival AoA, previously defined, by:

$$\alpha = (90° - \mathrm{AoA})$$

Also, the term 'χ' in equations (4.4) and (4.5) above is given by:

$$\chi = 18 \times 10^9 *(\sigma / f),$$

where the units of σ and f, here, are given in terms of [Sm^{-1}] and [Hz], respectively.

Straightforward manipulation of the complex reflection coefficients given by (4.4) and (4.5) yields their phases and magnitudes, which describe the phase and amplitude changes introduced in this reflection process. These are shown plotted versus AoA for the individual polarisations in Figures 4.5 and 4.6, respectively overleaf. It can be seen that for parallel polarisation a fairly abrupt phase change of ~180° (in the region AoA = 80° to 90°) gives rise to a minimum in the reflection amplitude in this region.

Insertion of the phase changes incurred on reflection, given by (4.4) and (4.5) for the two polarisations, into (4.3b), gives the *total* phase lags for the four direct & indirect ray and

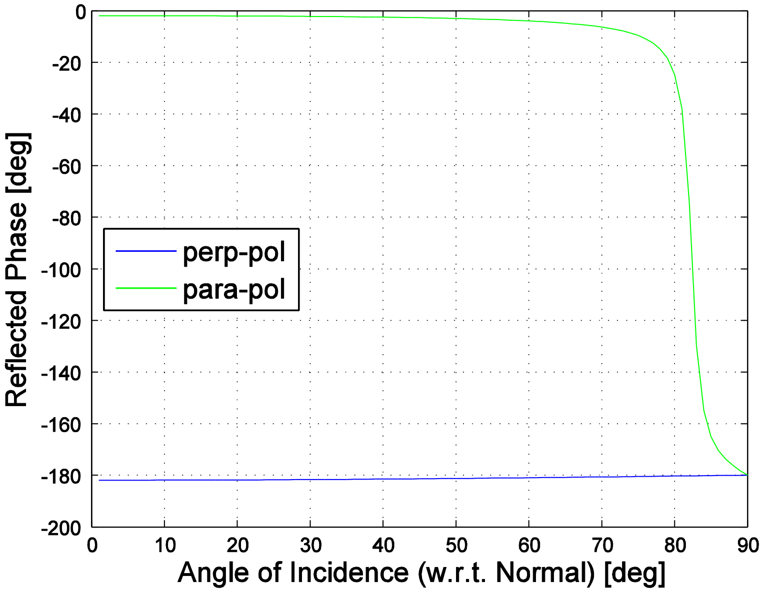

Figure 4.5: *Phase* of reflection coefficient (phs(ρ)) following reflection from slab of tissue (ε_{eff}=52.7, σ_{eff}=1.77Sm^{-1}) for parallel (||) and perpendicular (⊥) polarisations

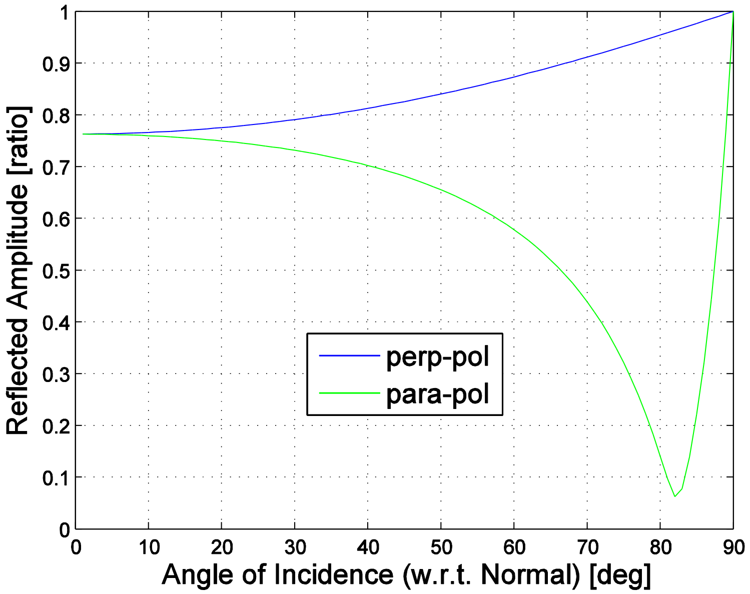

Figure 4.6: *Amplitude* of reflection coefficient (phs(ρ)) following reflection from slab of tissue (ε_{eff}=52.7, σ_{eff}=1.77Sm^{-1}) versus AoA for parallel (||) and perpendicular (⊥) polarisations

parallel & perpendicular polarisations combinations. These are individually plotted versus AoA in Figure 4.7, where the direct path, involving no reflection, has no polarisation dependence.

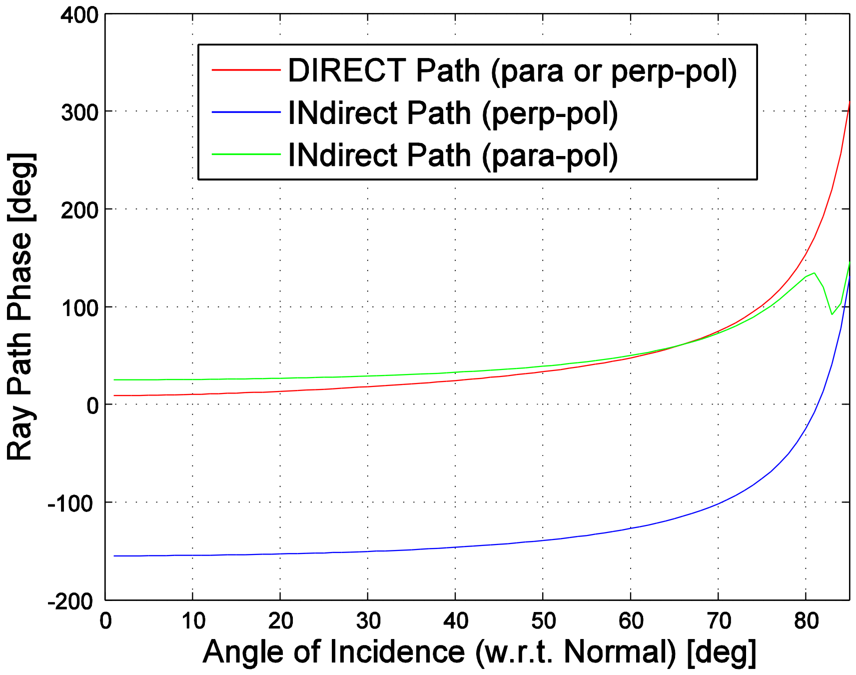

Figure 4.7: *Total* phases, due to different path lengths and (where applicable) any phase change upon reflection, for <u>direct</u>/<u>in</u>direct paths and parallel/perpendicular polarisations

The seemingly anomalous behaviour in the phase for the *parallel*-polarised *in*direct path at AoA ~83° in Figure 4.7 above is, in fact, genuine. It arises due to the combined effect of an exponentially increasing phase, due to the path length, combined with an abrupt phase decrease of ~170° due to phase change upon reflection in the AoA region from 80° to 90°.

Likewise, the corresponding *amplitudes* of the various ray/polarisation components are plotted vs. AoA in Figure 4.8 overleaf. The characteristic minimum in the amplitude of the parallel polarised indirect component associated with reflection in the region of the Brewster angle can be seen. Further, in addition to the amplitude change introduced upon reflection, the *amplitudes* of all these components have also been scaled according to the square-root of their distance travelled from the source to the common point B at which they intersect on the Illumination Plane. This is done to ensure conservation of *power* on the *cylindrical* wave front in the Near Field of the dipole antenna (the area of a cylinder being 2πrL). At this stage, for the sake of clarity, the source is also assumed to emit *equal*-strength co-polar and x-pol signals i.e. the co/x-polar ratio in free-space has been assumed to be 0dB. This point must be taken into account later when calculating the *actual* co/x-polar ratios for real-life antennas.

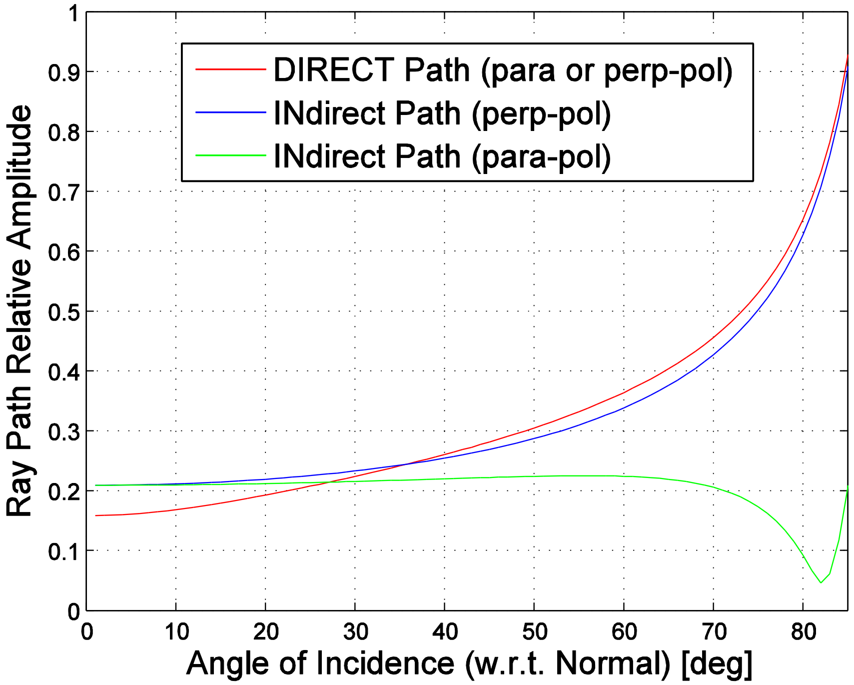

Figure 4.8: *Relative amplitudes*, due to different path lengths and (where applicable) amplitude reflection coefficients for <u>direct</u>/<u>in</u>direct paths and parallel/perpendicular polarisations

It is noted that Figure 4.8 shows that the *amplitude* of the perpendicularly polarised component, corresponding to the co-polar signal, is greater than that of the parallel polarised component associated with the x-polar signal. At first sight, therefore, it might be supposed that the antenna's co/x-polar ratio will be *in*creased by the presence of the body (rather than reduced). However, the resultant combination of the indirect and direct rays here must be computed by means of a *vector* sum and, since the phases in the two polarised components are different, the combined result for the different polarisations can be very different.

A vector diagram showing how the vector sum of the direct and indirect rays is formulated is shown (for arbitrary polarisation) in Figure 4.9. In practice, this vector sum is carried out separately for vectors corresponding to the two orthogonal polarisations involved here.

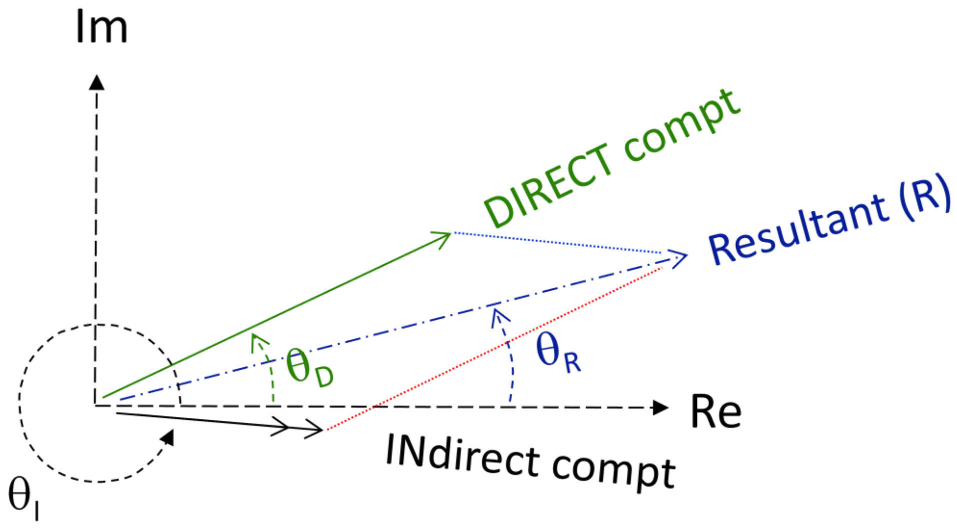

Figure 4.9: Vector Diagram Showing how Direct and Indirect Signal Components Combine to Yield the Total Resultant Signal

Figure 4.10 overleaf shows the resultant complex vector (magnitudes and phases) for different AoAs following the vector summation of the direct and indirect rays for perpendicular (⊥) and parallel (||) polarisations.

Figure 4.11, also overleaf, shows the radius (R) of the ‘ith’ common point B_i in Figure 4.1 where the direct and indirect rays cross the illumination plane from the centre point of this plane. Again, with reference to the geometry shown in Figure 4.1, this can be shown to be:

$$R = \sqrt{(OB_i^2 - h_2^2)} = \sqrt{((2*h_1 + h_2)^2 * \sec^2(AoA) - 4*h_1*(h_1 + h_2) - h_2^2)} \qquad (4.6)$$

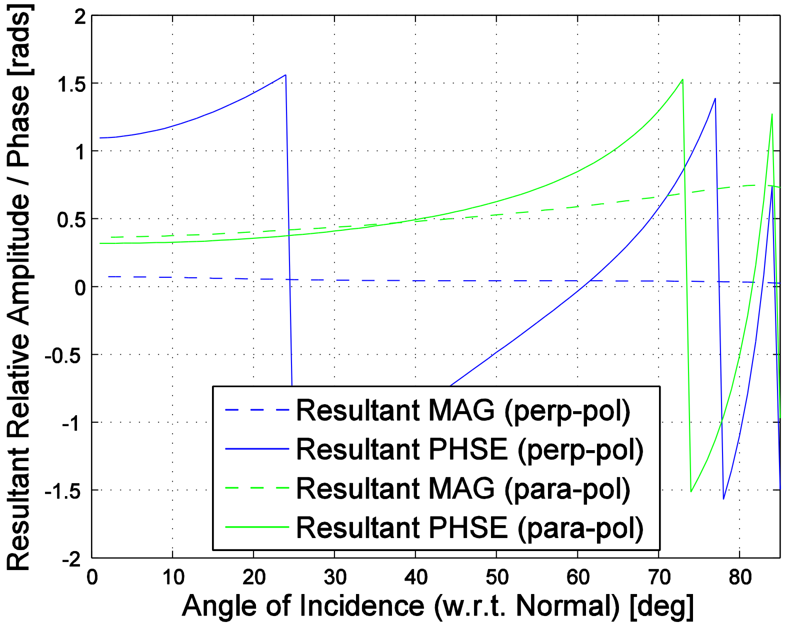

Figure 4.10: *Resultant* complex vector (magnitudes and phases) following vector sum of direct and indirect signals for parallel (||) and perpendicular (⊥) polarisations with h_1=h_2=(λ/40), ε_r=52.7 and σ=1.77Sm^{-1}

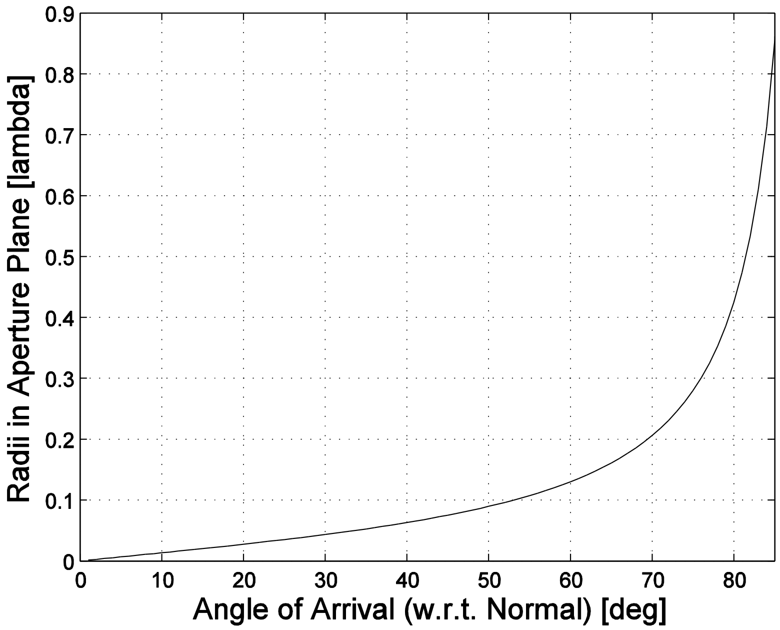

Figure 4.11: Radial location of 'ith' common point B_i on illumination plane for direct and indirect signals for h_2 = (λ/40)

Further, the difference between adjacent radii will give the length increment for adjacent AoAs over which the individual rays act. Consequently, by squaring the resultant *amplitudes* at a given AoA and dividing by its associated length increment, the *intensity* of the perpendicular (⊥) and parallel (||) polarisations can be calculated for the different AoAs. Figure 4.12 below shows the result of doing this and confirms that, as expected for the signal source here which is omnidirectional in the azimuth plane, the intensities for both polarisations are a maximum when the incident ray is normal to the body surface (AoA=0°) and fall away with larger AoAs when the body is illuminated more obliquely.

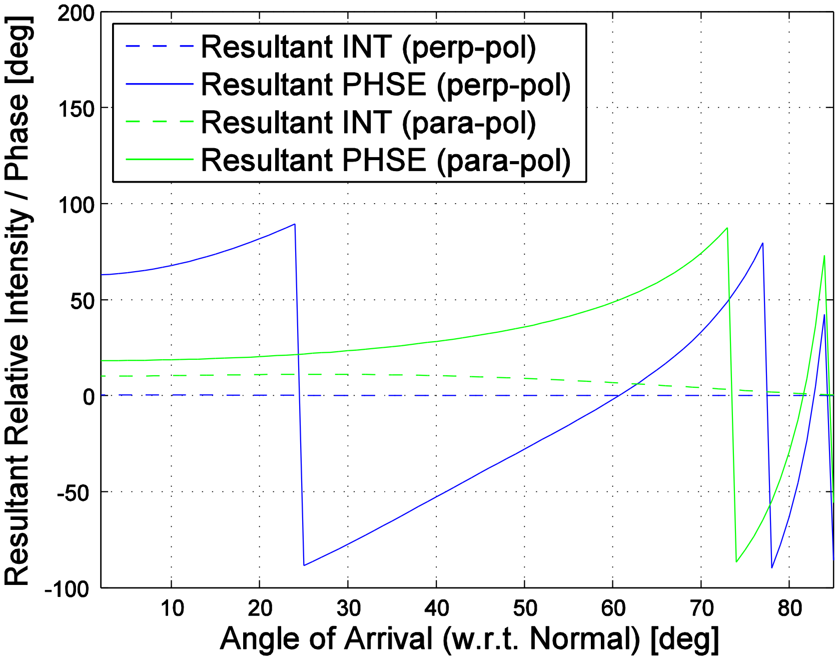

Figure 4.12: *Intensities* of resultant combined direct and indirect signals for parallel (||) and perpendicular (⊥) polarisations with $h_1=h_2=(\lambda/40)$, $\varepsilon_{eff}=52.7$ and $\sigma_{eff}=1.77Sm^{-1}$

Now, it is reasonable to assume that the ratio of the co/x-polar components of the signal in the far-field (FF) will be the same as the ratio of the perpendicular (⊥) and parallel (||) polarisation intensities on the illumination plane in the near-field (NF). Thus, to obtain the ratio of the co/x-polar components in the FF it is only necessary to derive the quotient of the perpendicular (⊥) and parallel (||) polarisation intensities on the illumination plane in the near-field (NF).

The result of doing so is shown in Figure 4.13 below, which plots the result of the co/x-polar ratios for different AoAs over the 0° to 90° quadrant as the solid red line. Also shown in Figure 4.13, as the dotted red line, is the *average* of these co/x-polar ratios across all AoA within this quadrant, which gives -6.5dB. Finally, shown as the solid blue line, is the average co/x-polar ratio, which is 13dB for this antenna, when in *free-space*.

Thus, the *average* reduction in co/x-polar (over 90° quadrant in AoA here) predicted by this analysis is (13 – (-6.5)) = 19.5dB. Given the approximate nature of this analysis, its predicted 19.5dB reduction is in remarkable agreement with the actual 19dB *measured average* reduction and in reasonable agreement with the 16dB CST *simulated average* reduction reported earlier here in Table 3.2 for an air gap between the human body and antenna of T_{airgap} = 3mm, as here.

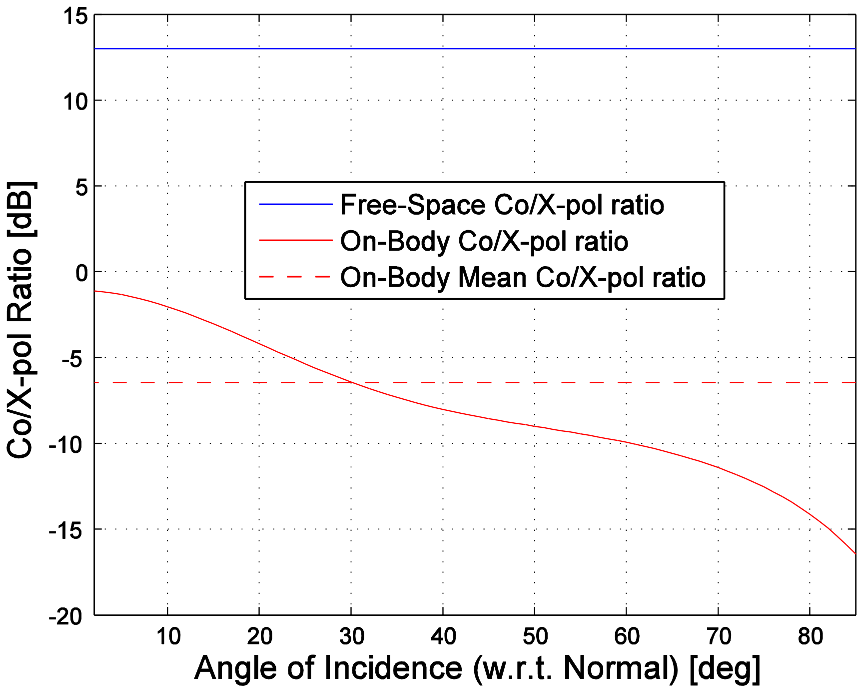

Figure 4.13: Corresponding average *Co/X-pol ratios* versus Angle of Arrival (AoA) for $h_1=h_2=(\lambda/40)$, $\varepsilon_{eff}=52.7$ and $\sigma_{eff}=1.77Sm^{-1}$

All considerations reported so far here have been for (h_1=h_2=λ_0/40), so that the dielectric slab and the illumination plane are both in the near-field of the antenna source. However, investigations were also conducted in which h_2 was gradually increased until the illumination-plane was located in the far-field of the antenna. It was found that the co/x-polar ratio gradually increased, being -6.5dB in the near-field ($h_1 = h_2 = \lambda/40$) and tending to -2.8dB at h_1=1024*h_2=25λ (i.e. the far-field).

However, this behaviour is likely to be expected because the analysis scales the amplitudes of the various components by the square-root of the path distances they travel, in order to conserve energy on the basis of cylindrical wavefronts in the near-field. Now, when the illumination plane is in the far-field, the assumption that the wavefronts are cylindrical is no longer valid, so that the amplitudes will require a different scaling factor. Whilst interesting, this was not pursued further as the objective of the analysis had already been achieved.

4.5 Conclusions

The ‘relatively unsophisticated’ analysis here assumes *cylindrical* wavefronts (rather than uniform plane waves) emanating from the thin-wire dipole antenna within its near-field region. These allow the illumination intensities on multiple patches on a hypothetical plane in the intermediate zone to be derived. These patches act as secondary sources and, the use of a Huygens Wavefront Reconstruction approach would allow the far-field radiation patterns to be derived by means of a vector summation process of all these secondary sources. This is analogous to the explanation of diffraction (as caused by a knife-edged obstacle) [103]; a familiar phenomena whose existence could not otherwise be explained purely in terms of uniform plane waves.

Good agreement has been found between the *average* reduction in the co/x-polar ratio derived here using an approximate and relatively unsophisticated analysis, with that observed for the candidate ‘Rufa’ antenna when in close proximity to the human body.

It is noted that this analysis involves only conventional space wave propagation, and it was not found necessary to invoke more esoteric propagation modes, such as surface waves, to adequately account for the observed depolarisation effect of the body. This is not to imply that such propagation mechanisms are absent here; indeed, they are likely to be present but appear to be of secondary significance in the present case.

As a result, it is concluded therefore that the analysis presented here provides (at the very least) a useful emulation of the observed depolarisation effect on the Rufa 'COTS' antenna when it is relocated from its intended free-space location to be in close proximity to the human body.

Whether or not the mechanisms used in this analysis here provide the definitive explanation of the physical mechanisms actually taking place would require further work beyond the scope of the present study. This could be worth considering, if only to indicate whether it might be more widely applicable to antenna analysis and design.

Chapter 5

System Performance Using Ray Tracing Techniques

5.1 Introduction

Having established the changes in RF performance of a candidate COTS ‘Rufa’™ antenna when used in close proximity to the human body, it was important to determine whether or not it was still suitable for use in an indoor propagation scenario which was representative of the intended Telecare/Telemedicine application here.

Therefore, simulations of the overall system were conducted using Remcom’s well-established ‘Wireless InSite’ (WI) software package [88], which employs ray-tracing type modelling techniques [89]. As stated earlier in section 3.7, this package has the facility to provide either internally-generated generic antenna patterns, for example an ideal half-wave dipole, or user generated specific pattern data, such as that for the on-body ‘Rufa’™ antenna considered here.

The ‘L’-shaped Body Centric Laboratory (BCL) at QMUL (following its reconstruction in Y2010) was taken as a typical indoor scenario for this study. The WI scale model of this is shown in Figure 5.1 where, to give some idea of perspective, the longest wall here is 8.6m.

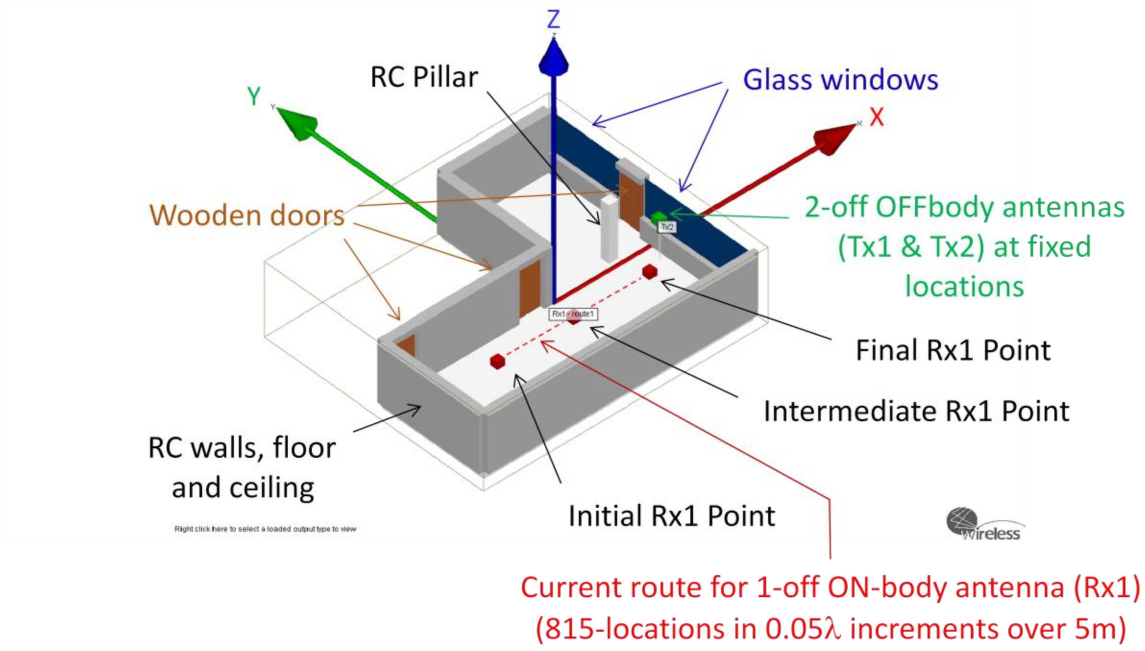

Figure 5.1: Wireless InSite Model of QMUL's Body Centric Laboratory

The propagation parameters in this WI model were initially set up to allow:

i) 2 reflections from surfaces,
ii) 0 transmissions through objects, and
iii) No diffraction from suitable diffraction candidates

No furniture or similar objects were included as this would make the model less generic, as well as significantly increasing its complexity and hence execution time.

Figure 5.2 shows the ray paths determined by the model as a result of these initial propagation parameters at three points along an example 5m linear route taken by the mobile patient/client as it moves towards the Access Point as given in Figure 5.1.

More stringent propagation parameters were also investigated which resulted in more ray paths, as expected. However, it was observed that the powers in these additional paths were much lower. Consequently, because these more stringent propagation parameters

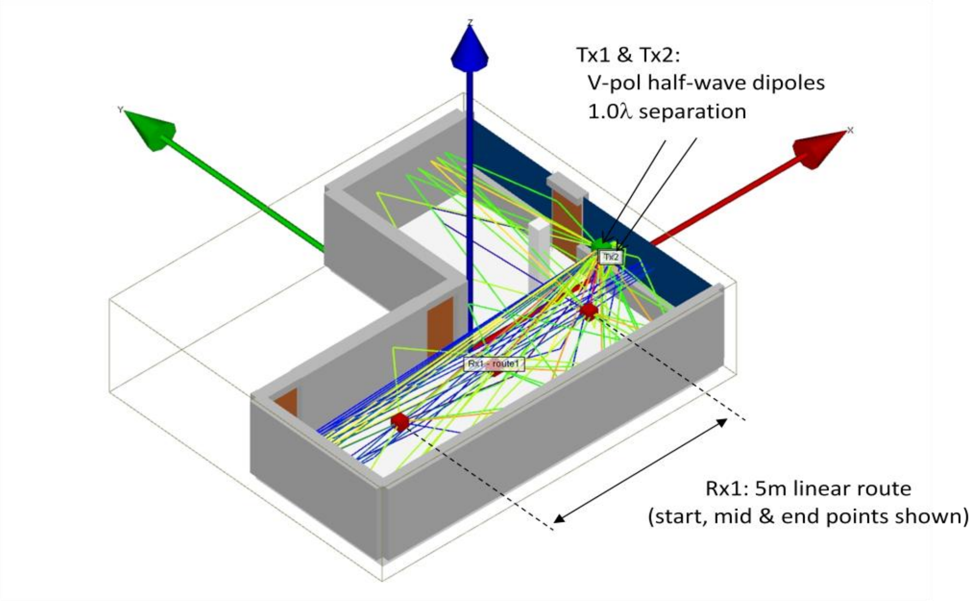

Figure 5.2: Propagation Paths Involved in BCL Model for Three Example Locations of the On-body Antenna along its Linear 5m Route with *Original* Propagation Parameters

were found to have little influence on subsequent key results, but drastically increased the WI model's execution time, by a factor of 60x with these more stringent parameters, the original parameters given earlier were reverted to for use thereafter.

As initially suspected in this multipath-rich indoor environment, a measure of diversity was found to be necessary at the *off*-body Access Point to mitigate the effect of deep (~20dB) multipath fading without recourse to the more crude expedient of increasing on-body transmit power with its corresponding shortening of on-body battery lifetimes.

Accordingly, *two* transmit antennas separated by variable distance are shown at the *off*-body Access Point in Figures 5.1 and 5.2. Two fixed *transmit* antennas at the *off*-body Access Point and a single moving *receive* antenna at the on-body location are shown (i.e. the downlink) because the WI software does not permit use of moving transmit antennas. This is not a problem, however, as transmit/reciprocity can be invoked, since the antenna(s) at both ends of the link are used for both transmit and receive purposes on a duplex basis. Hence, the propagation characteristics for the uplink (from the on-body transmit antenna to the two receive antennas at the Access Point) are identical for those derived for the downlink here using the WI model.

To investigate the potential improvement afforded by *spatial* diversity, two identically polarised *off*-body antennas (V-pol dipole type, internally generated within the WI model) but having *non*-zero *separation* were specified.

Subsequently, to investigate the potential improvement afforded by *polarisation* diversity, two *collocated* (i.e. zero separation) but *orthogonally-polarised* off-body antennas (V-pol and H-pol dipole type) were specified within the WI model.

Although thermal noise at a given specified level could be included in the WI simulation, this option was turned-off in the model here. As a result, the WI model generated pure signals as seen by the two off-body antennas in order to provide a clearer *qualitative* insight into the effect of multipath(s) involved in this scenario, without the distracting influence of thermal noise.

Thus, the output of the WI model is a common plot which includes pure signal levels, from the two off-body antennas, versus distance travelled by the on-body antenna at 815 locations in 0.05λ increments along the linear route shown in Figure 5.1. An example of this is shown later in Figure 5.4.

Following this WI model, the pure signal level data was imported into a user written MATLAB analysis, reproduced in Appendix A1 here, which included simple Selective Combining (SC) processing to implement the diversity scheme used to mitigate multipath fading. After this, the MATLAB analysis includes the effect of thermal noise, at an appropriate level given by the link budget considered in section 5.2 following.

Finally, the MATLAB analysis performs a statistical analysis of the resulting signal-to-noise levels for the 815 different samples along the 5m example linear route, to derive the diversity gains for the two different spatial and polarisation diversity schemes.

As a result, the *qualitative* insight, provided by the initial noise-free WI simulation data here, is augmented by the more *quantitative* statistics of the diversity gain afforded by the subsequent MATLAB statistical analysis for the signal-only WI data when random thermal noise is included.

5.2 System Link Budget to Determine Typical On-Body Transmit Power Required

Figure 5.3 below shows key modules and their parameters involved in the simple wireless link assumed here between the wireless-equipped on-body sensor node and its associated off-body Access Point.

A link budget for Figure 5.3 in the *absence* of multipath, is given in this section to derive an upper-bound on the on-body transmit power required to achieve a given SNR. This defines the link performance, in the worst case scenario identified. This worst case scenario, having the lowest received signal power, is due to the most extreme blockage by the body (associated with the lowest on-body antenna gain). This NLOS case occurs when the patient/client is moving along the linear route *away* from the off-body Access Point. The effect of multipath fading is considered separately later using results of the WI model.

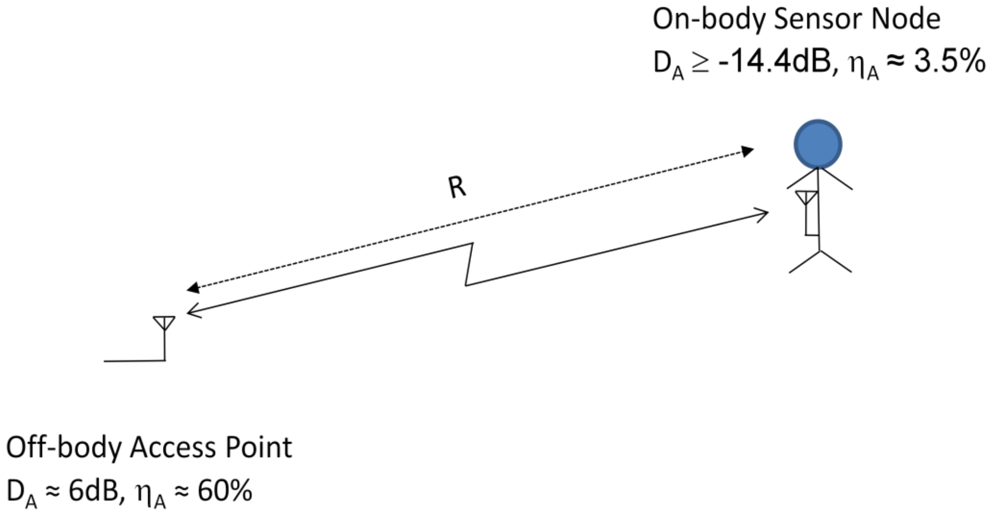

Figure 5.3: Key parameters for Simple Wireless Link Here

Ignoring receiver gain, being common to both signal and noise components, the thermal noise floor at the output of a receiver in a wireless link is given by:

$$N = k \cdot T \cdot B \cdot NF_{Rx} \quad \text{W}$$

$$= 10.\log_{10}(k.T) + 10.\log_{10}(B) + 10.\log_{10}(NF_{Rx}) \quad \text{dBW} \qquad (5.1)$$

where:

k is Boltzmann's Constant = 1.38×10^{-23} JK^{-1},

T is the typical receive temperature = 290 K (= 20°C),

B is ISM band individual channel bandwidth, here = 5×10^{6} Hz, and

NF_{Rx} , is typical receiver noise figure = 3dB, (say).

Hence, in dB terms:

$10.\log_{10}(k.T) = -202.98$ dB

$10.\log_{10}(B) = 66.99$ dBHz

Therefore, substituting these values into equation (5.1) gives the thermal noise floor level:

$$N = -202.98 + 66.99 + 3 \quad \text{dBW}$$

$$= -132.99 \quad \text{dBW} \qquad (5.2.)$$

Now, ref [90] indicates that to obtain a reasonable Bit Error Rate (BER) of (9×10^{-4}) for the important medical data involved here (with a relatively straightforward Differential Phase Shift Keying (DPSK) modulation scheme) requires a signal-to-noise ratio of

SNR = 8dB.

Hence, in the *absence of multipath* fading, the signal level required to give this BER would be

$$S = (SNR + N) = +8 - 132.99 = -125.99\text{dBW} \qquad (5.3)$$

Now, in terms of key system parameters for a transmitter (Tx) located at range (R) from a receiver (Rx), in the *absence* of multipath fading this signal level is also given by:

$$S = (P_{Tx} . D_{Tx} . \eta_{Tx}) . (D_{Rx} . \eta_{Rx}) . ((c/f_c)^2/4\pi)) . R^{-n} \quad W \qquad (5.4)$$

Once again, receiver gain has been ignored here as this is common to both receive signal and noise components.

So, in dB terms, equation (5.2.3a) becomes

$$\begin{aligned} S &= P_{Tx}\,[dBW] + D_{Tx}[dBi] + \eta_{Tx}[dB] \\ &\quad + D_{Rx}[dBi] + \eta_{Rx}[dB] \\ &\quad + 10.\log_{10}(c^2/4\pi) - 20.\log_{10}(f_c) \\ &\quad - 10.n.\log_{10}(R[m]) \qquad dBW \end{aligned} \qquad (5.5)$$

Typically, the effect of propagation in the indoor scenario here is to increase the exponent of the *long-term* range dependence from n=2.0 (its value in free-space) to n = 3.0 [91].

For the on-body end of the link, having the COTS ‘Rufa’ antenna, the following parameters apply:

P_{Tx} is on-body transmit power = TBD [dBW],

D_{Tx} is minimum transmit antenna directivity $\geq$ -14.4dBi (NLOS worst case), and

η_{Tx} is on-body antenna efficiency = 3.5%, => $10.\log_{10}(\eta_{Tx}) = -14.56$dB.

At the off-body end of the link, having V-pol dipole antennas with some elevation directivity, the corresponding parameters are:

D_{Rx}, is transmit antenna directivity = +6dBi, and

η_{Rx}, is off-body antenna efficiency = 60% => $10.\log_{10}(\eta_{Tx}) = -2.22$dB.

The centre frequency of the ISM band for the link here is:

$f_c = 2.4418$ GHz $\Rightarrow 20.\log_{10}(f_c) = 187.75$dB

It is noted that, to ensure SNR = 8dB required for the 1% link-outage level, it is necessary to use an average $SNR_{av} = 21.5$dB in the MATLAB analysis programme. This SNR_{av} will be that experienced at an intermediate point along the mobile patient/client route and hence is quite a lot higher than the SNR = 8dB required, which will be that incurred at the start of the route here (where $R_{max} = 5$m).

Also, in the scenario here, the maximum link range on the patient/client route here is:

$R \leq 5$m $\Rightarrow 30.\log_{10}(R[m]) \leq 20.97$dB.

Finally:

$10.\log_{10}(c^2/4\pi) = 158.55$dB.

So, on substitution into equation (5.5), these values give:

$$\begin{aligned} S \geq\ & P_{Tx}\,[dBW] - 14.4dBi - 14.56dB \\ & + 6dBi - 2.22dB \\ & + 158.55dB - 187.75dB \\ & - 20.97dB \\ & = P_{Tx}\,[dBW] - 75.74dB \end{aligned} \tag{5.6}$$

Thus, equating equations (5.3) and (5.6) gives:

$-125.99dBW \geq P_{Tx}\,[dBW] - 75.74dB$

Hence:

$$P_{Tx} \leq -50.25\ [dBW] \approx -20dBm \approx 10\mu W \tag{5.7}$$

The 10μW transmit power here is an upper-bound, since the lowest on-body directivity, where the signal arrives via the direct *N*LOS direction has been assumed here.

However, it is *re*-emphasised that this on-body transmit power, of about -20dBm, is that which would be required to ensure acceptable link SNR (and hence BER) *in the absence of multipath fading*.

So, in any *real* indoor scenario where deep multipath fading occurs, a crude way of compensating for this fading would be to increase the on-body transmit power commensurately. For example, to counteract deep 20dB multipath fades, the -20dBm on-body transmit power above would need to be increased to +0dBm. However, this would dramatically reduce the lifetime of the on-body battery required. More crucially, this +0dBm *slightly exceeds* the maximum regulatory level for on-body use, which has been specified in [92] as -1.25dBm (i.e. 0.75mW). In this regulatory context, reference [93] is also of interest.

Fortunately however, as will be shown in Section 5.3 following, spatial diversity given by two optimally spaced off-body antennas at the Access Point can provide typically 8dB processing gain in severe multipath fading conditions. Therefore, a more sophisticated approach is proposed here, whereby this 8dB spatial diversity gain is used to partially offset the deep 20dB multipath fading.

As a result, the original -20dBm on-body transmit power in the absence of fading need only be increased by 12dB now to -8dBm to counteract 20dB fades. Crucially, this revised -8dBm figure is now about 7dB (i.e. 5x) lower than the maximum regulatory value of -1.25dBm [92].

In addition, of particular significance for user acceptability of the *on*-body wireless equipped sensor nodes considered here, the use of spatial diversity to significantly decrease on-body transmit power, will greatly increase the lifetimes of the on-body batteries. In this regard, the wireless aspect of the wireless-equipped on-body sensor nodes is assumed to dominate their overall power consumption.

Finally, the 12dB reduction in the on-body node transmit power, afforded by the use of spatial diversity, will have a further advantage in that it will greatly enhance the node's electromagnetic compatibility (EMC) with other wireless devices which are also operating within this already congested ISM band.

For the sake of completeness, it was thought useful to include Table 5.1 here. This contains the different variable parameters used within this link budget, the symbols used to represent them and the values assumed for these.

Parameter	Symbol	Value	Units
Boltzmann's Constant	k	1.38×10^{-23}	JK^{-1}
Receiver Temperature	T	290	K
ISM-band Channel Bandwidth	B	5×10^{6}	Hz
Typical Receiver Noise Figure	NF_{Rx}	3	dB
On-Body Transmit Power	P_{Tx}	**TBD**	dBW
On-Body Transmit Antenna Directivity	D_{Tx}	-14.4	dBi
On-Body Transmit Antenna Efficiency	η_{Tx}	2.2	%
ISM-band Centre Frequency	f_c	2.4418×10^{9}	Hz
Off-Body Receive Antenna Directivity	D_{Rx}	+6	dBi
Off-Body Receive Antenna Efficiency	η_{Rx}	60	%
Maximum Range	R	5	m
Propagation Constant: $10.\log_{10}(c^2/4\pi)$	N/A	158.55	dB

Table 5.1: Listing of Variable Parameters Appearing in the Link-Budget here

5.3 Off-body *Spatial* Diversity: *Reference* Case with V-pol Half-Wave Dipoles for *all* Antennas

Initially, to provide an ideal *reference* case against which other cases can be compared, a WI simulation (and subsequent MATLAB analysis) was performed for a link in which *all* *three* antennas (one on-body and two off-body) were *identical ideal half-wave V-pol dipoles* generated internally within the WI simulation.

Figure 5.4 below shows the output of the individual signal levels, on the two branches here afforded by the two off-body antennas Tx1 (blue line) and Tx2 (green line), following MATLAB plotting of the basic pure signal data generated by the WI model. As expected, on an average basis, the long-term trend is for the signal levels to rise as the mobile antenna proceeds along the route towards the individual fixed antennas at the Access Point and link range decreases.

Obviously, no spatial diversity is involved in the two *individual* branches here and the expected deep (typically up to 20dB) multipath nulls are clearly evident in both cases.

Figure 5.4: Received signal powers with and without *spatial* diversity for 1.0λ separation between the two off-body antennas for *Reference* Case (with identical V-pol dipole antennas for all three antennas involved here)

However, it is also clearly evident that the peaks in the blue plot (for Tx1) correspond to the nulls in the green plot (for Tx2) and vice-versa. This decorrelation is ideal for a diversity scheme, and shown superimposed in red in Figure 5.4 is the result *with* spatial diversity implemented by means of simple selective combining (SC) within the MATLAB analysis programme. This SC scheme just compares the signal levels within the individual branches and chooses that having the greatest power. Therefore, as expected, the multipath nulls present in the plots for the individual signal branches with*out* diversity are largely absent in the red plot *with* spatial diversity.

Using the average noise level, given by the link budget earlier in section 5.2, the MATLAB analysis programme then calculates the individual signal-to-noise levels at each of the 815 locations along the 5m standard route originally indicated in Figure 5.1. From this it identifies those locations, having SNR below the 8dB level, which give rise to link errors at BER > $9x10^{-4}$ for DPSK modulation and constitute a link outage. These outages can be detected by simple error detection means, and rectified by a straightforward repeat transmission at a different subsequent location. However, since this is standard practice, it is not considered further here.

Details of the derivation of generic diversity-gain from the multiple instances of SNR along the route here are given with reference to Figure 5.5 overleaf. This shows representative Cumulative Distribution Functions (CDFs), being plots of the number of instances (y-axis) having signal-to-noise-ratio ≤ SNR (x-axis), for the cases with*out* and *with* diversity.

As might be expected, for the two extreme link outage cases in Figure 5.5:

i. 100% link outage, corresponding to *all* the data (815 instances here), occurs if the SNR required to achieve a specific BER exceeds SNR_{max}, and,
ii. 0% link outage, corresponding to *none* of the data, is obtained if the SNR required to achieve a specific BER is less than SNR_{min}.

For an intermediate link outage case (say 1%), corresponding to $y = (815 \text{ x } (1/100)) \approx 8$ instances within a total population of 815 data points here, Figure 5.5 shows that:

i. With*out* diversity, this 1% outage corresponds to 8 instances having SNR ≤ x dB

ii. *With* diversity, the same 1% outage gives 8 instances having SNR ≤ x' dB.

Since (x' > x), the application of diversity can be seen to have given rise to an improved SNR level for a given outage, thereby effectively providing a SNR gain.

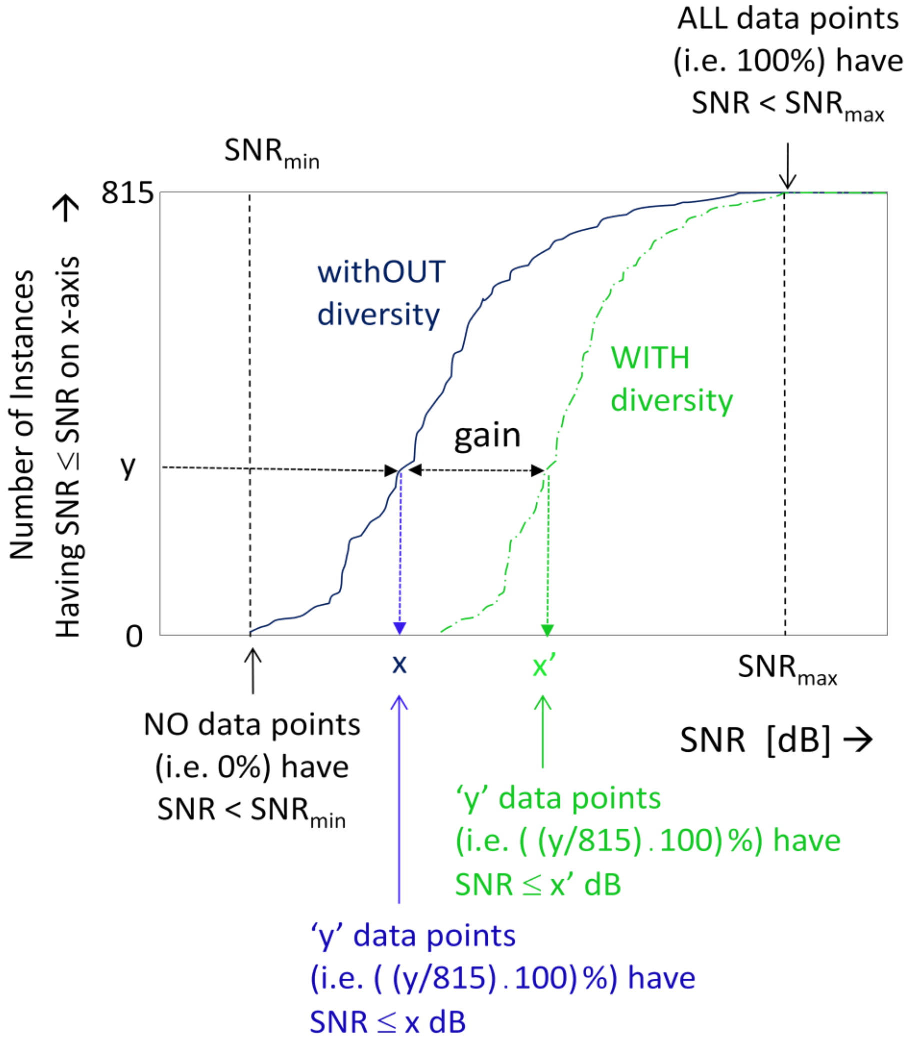

Figure 5.5: Typical Cumulative Distribution Functions for *with* and with*out* Diversity Cases

An example of the result of this analysis performed by the MATLAB programme, operating independently on the two data sets (*with* and with*out* spatial diversity) generated by the WI simulation propagation model of the Body Centric Laboratory, is shown in Figure 5.6.

This shows the tail-ends of the resulting CDFs for these two data sets on a common plot to allow direct comparison. As previously described the difference between the SNRs at common link outage levels on these plots *with* and with*out* diversity is the diversity gain for the *spatial* diversity scheme here.

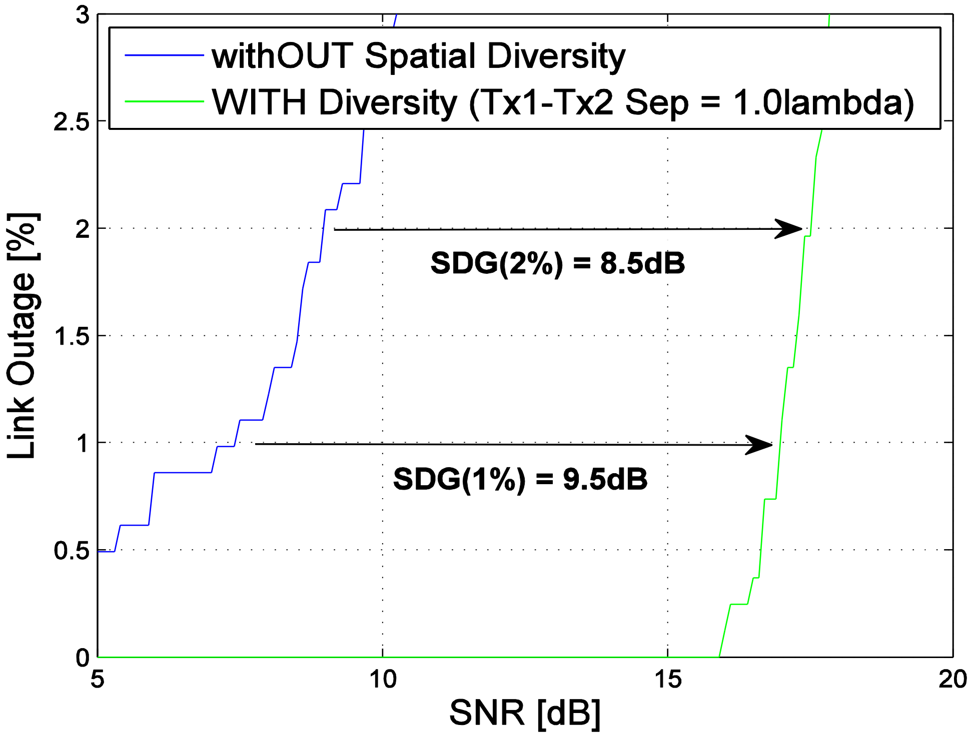

Figure 5.6: Link Outages versus SNR *with* and with*out* spatial diversity for 1.0λ separation between the two off-body antennas for *Reference* Case (with identical V-pol dipole antennas for all three antennas involved here)

Specifically, Figure 5.6 shows that, with*out* diversity, 1% of the data has an SNR less than 7.5dB. For DPSK modulation, these instances give rise to a BER in excess of (9×10^{-4}) thereby contributing to the 1% overall link outage.

Likewise, Figure 5.6 also shows that the SNR *with* spatial diversity at the same 1% link outage level is 17.0dB. This is for 1.0λ separation between the two off-body antennas

Therefore, the difference between these two SNR levels at the common 1% outage level constitutes a substantial 9.5dB *Spatial* Diversity Gain (SDG) at this level in this reference case in which all three antennas involved are internally-generated ideal V-pol dipole types.

5.3.1 Effect on *Spatial* Diversity of Varying Separation between Off-body Antennas for Reference Case

The analysis procedure, described above for 1.0λ separation between the two off-body antenna elements at the Access Point, was repeated using WI model generated data sets for different inter-element spacings of 0.5λ, 0.75λ and 1.5λ. The aim here was to determine the optimum inter-element separation giving the largest spatial diversity-gain.

Now, rather than showing a multiplicity of slightly different plots (corresponding to Figures 5.4 and 5.5 earlier) for the different inter-element spacings, it is considered more meaningful to plot the resultant spatial diversity gains for these four spacings, as shown in Figure 5.7 overleaf. From this, it can be seen that, for both 1% and 2% outage levels, the maximum spatial diversity gain occurs at about 1.0λ separation between the two off-body antennas.

Finally, it is reassuring to note that reference [94] for an M = 2 branch system (such as the (1 x 2) SIMO scheme simulated here) also gives SDG = 10dB and 8dB for outages of 1% and 2% respectively (c.f. 9.5dB and 8.5dB in figure 5.6 here). It is noted that reference [94] assumes that the signals in the two individual branches are largely uncorrelated; as is the case here when the separation between the two off-body antennas is 1.0λ.

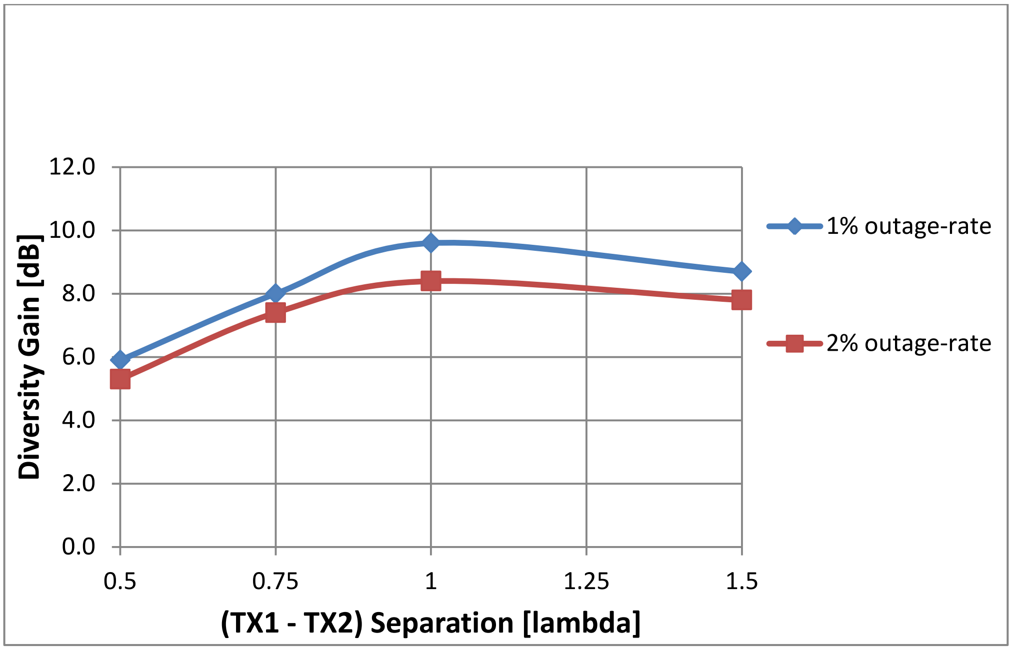

Figure 5.7: Spatial Diversity Gain at 1% and 2% Outage Levels for SNR_{av} = 10dB

5.4 Off-body *Spatial* Diversity: COTS ‘Rufa’ *On*-body Antenna

Considerations so far have been for the *reference* case in which identical V-pol dipole antennas are used for all three antennas involved here. It is now appropriate to consider the *real-life* case where the single dipole antenna at the *on*-body end of the link is replaced by a single COTS ‘Rufa’ on-body antenna whose patterns include body-blockage and are largely depolarised.

However, the two V-pol dipole antennas having 1.0λ separation between them are still retained at the *off*-body end of the link to permit direct comparison between this and the reference case.

Accordingly, the Wireless Insite simulation model was modified to read-in the 3-D CST simulated antenna co-polar and x-polar pattern data-files, generated as described earlier in selection 3.7. This 3-D co-polar and x-polar pattern data is representative of the patterns of the COTS ‘Rufa’ antenna when used *on*-body; in particular, having ~15dB of body-blockage.

Results for this *real-life* 'Rufa' COTS antenna *on*-body are shown in Figures 5.8 and 5.9. These are equivalent to Figures 5.4 and 5.6 shown previously for the *reference* case having a V-pol dipole antenna at the *on*-body end of the link.

Comparison of the signal levels versus distance along the mobile on-body antenna's route in Figure 5.8 here with those shown previously for the *reference* case in Figure 5.4 shows similar long-term trends and medium-term multipath behaviour

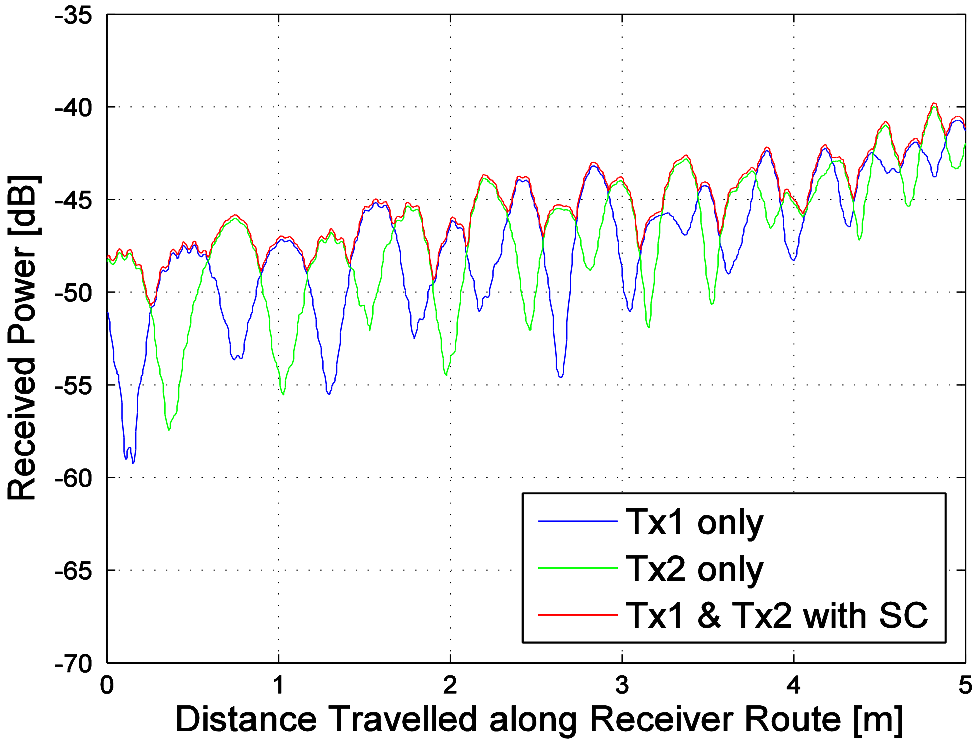

Figure 5.8: Received signal powers with and without *spatial* diversity for two V-pol dipole off-body antennas and a single *COTS 'Rufa' onbody antenna* used *on*-body here

However, the short-term fluctuations, originally present in Figure 5.4 for the reference case, are now largely absent in Figure 5.8 with the COTS 'Rufa' onbody antenna. An analysis to be presented later in section 5.9 will show that the original short-term fluctuations are due to multipath reflections from the wall *opposite* the Access Point in the BCL scenario simulated here.

Owing to the (typical 15dB) body blockage of the COTS 'Rufa' on-body antenna used in Figure 5.8, the multipath signals reflected from this wall are much reduced compared to those for the reference case in Figure 5.4, where the V-pol on-body antenna is largely omnidirectional in azimuth. As a result, the short-term peak-to-peak fluctuations due to these signals are also greatly reduced in Figure 5.8. However, since the relative phases in the direct and indirect paths are unaffected by the different on-body antenna patterns in the two cases, the *location* of the nulls and peaks in the resultant received signals remains the same in both cases.

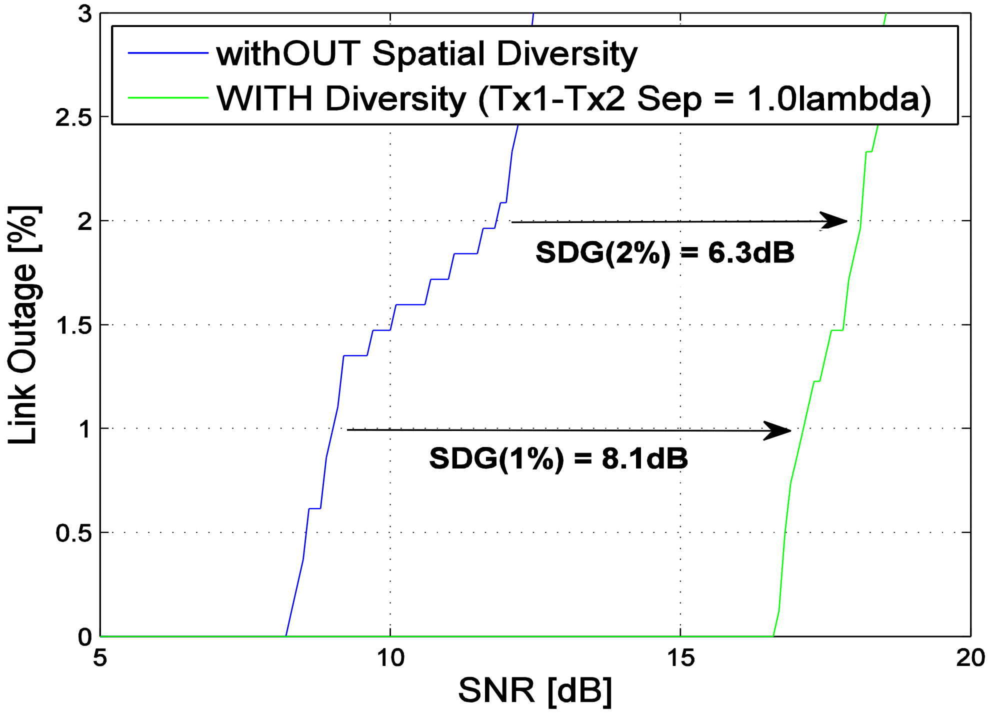

Figure 5.9: Link Outages versus SNR *with* and with*out* off-body spatial diversity for two V-pol dipole off-body antennas and a single *COTS 'Rufa' antenna* used *on-body* here

Figure 5.9 above shows the corresponding plot of link outage versus SNR with the real-life *on*-body antenna. By comparing with Figure 5.6 for the reference *on*-body antenna case, it can be seen that the COTS 'Rufa' on-body antenna affords slightly less off-body *spatial* diversity gain than the original reference case with a V-pol dipole at the on-body end of the link (The spatial diversity gains at the 1% and 2% link outage levels are 8.1dB and 6.3dB now respectively, compared to 9.5 and 8.5dB originally). This only minor degradation is good since, as discussed earlier, this ~8dB diversity gain is essential if adequate overall system performance is to be realised with reasonable *on*-body transmit powers and battery lifetimes.

5.5 Off-body *Polarisation* Diversity: *Reference* Case

Sections 5.3 and 5.4, just given, have considered cases for an off-body *spatial* diversity scheme.

By way of comparison, the effect which the depolarised nature of the COTS ‘Rufa’ on-body antenna might have on the diversity-gain afforded by an off-body *polarisation* diversity scheme was also investigated and reported in this section and 5.6 following.

To do so, a conventional polarisation diversity scheme was initially simulated to provide a *reference* case. In this case, an ideal quarter-wave dipole, rotated by 45°, was used at the *on*-body end of the link in conjunction with the original two *collocated* but *orthogonally* polarised (V-polar and H-polar) dipole antennas at the *off*-body end of the link.

The results of *polarisation* diversity for this reference case with are shown in Figures 5.9 and 5.10. The signal levels versus distance plots in Figure 5.9 show a small (~3dB) reduction in long term average signal level for all three curves when compared to those for the reference case for *spatial* diversity (Figure 5.4). This is probably due to the fact that the on-body antenna, being rotated by 45° here, is no longer polarisation-matched to either of the V-pol and H-pol antennas at the off-body end of the link. In this regard, a 45° polarisation mismatch would be expected to produce a $10*\log_{10}(\cos^2(\pi/4)) \approx 3$dB loss.

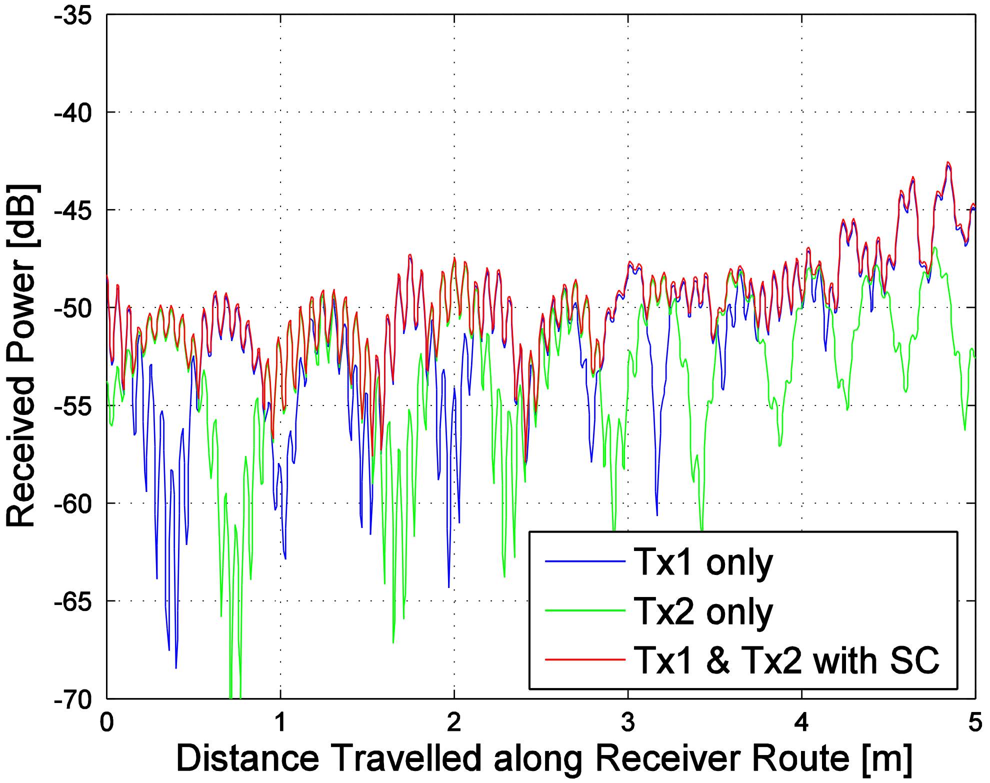

Figure 5.10: Received signal powers versus distance *with* and with*out* Off-body *Polarisation* Diversity for the *Reference* Case

Inspection of Figure 5.10 indicates that the short-term signal level fluctuations, associated with reflections from the wall opposite the Access Point in the BCL scenario, have returned for the ideal dipole antenna used at the *on*-body end of the like once more in this reference case. This is expected since this ideal dipole antenna is omnidirectional in azimuth.

Nonetheless, the general decorrelation between individual branches (blue and green curves) in the 2-branch off-body polarisation diversity scheme here is still potentially favourable for a diversity scheme. The result of this, with simple selective combining, is given as the red curve in Figure 5.10.

Figure 5.11 shows the corresponding plots of link outage versus SNR. It can be seen that, for this *reference* case, the off-body *polarisation* diversity scheme here affords 6.7dB and

5.9dB polarisation diversity gain at the 1% and 2% link outage levels respectively. This is slightly less those for the equivalent *reference* case for *spatial* diversity, considered earlier in section 5.3, which gave 9.5dB and 8.5dB (Figure 5.6).

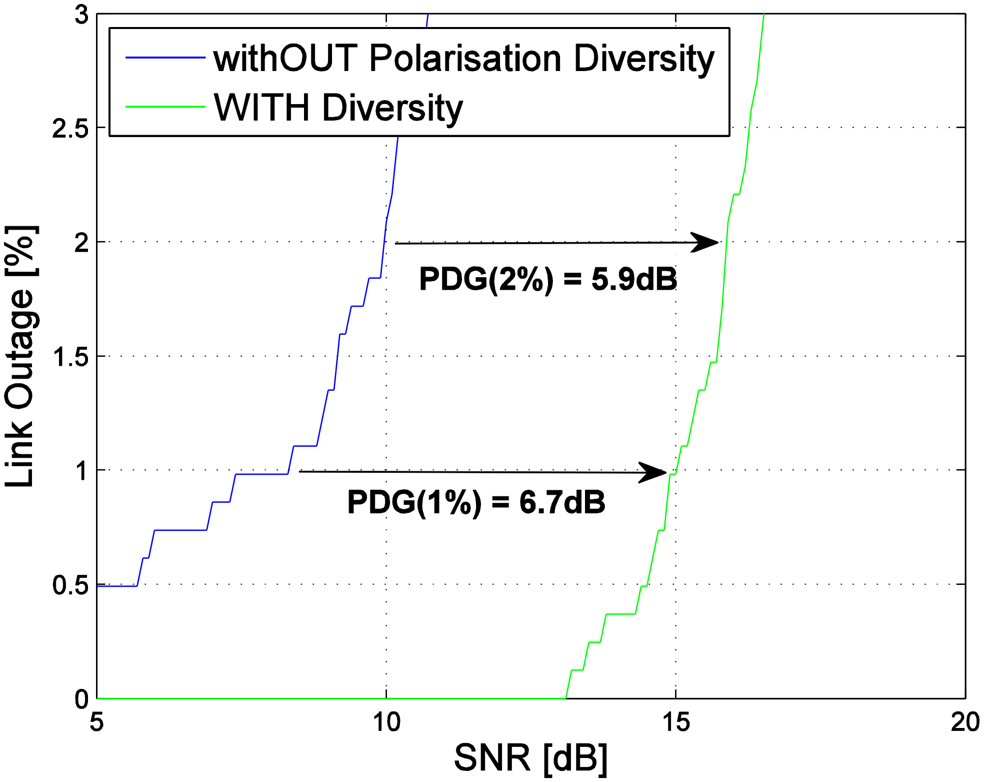

Figure 5.11: Link Outages versus SNR *with* and with*out* Off-body *Polarisation* Diversity for the *Reference* Case

5.6 Off-body *Polarisation* Diversity: COTS 'Rufa' *On*-body Antenna

Finally, as before, the 45°-pol dipole on-body antenna in the reference case is replaced with the 'real-life' depolarised COTS 'Rufa' on-body antenna. Again, to permit direct comparison with the reference case (section 5.5), the two *collocated* but *orthogonally* polarised (V-pol and H-pol) off-body antennas are retained for use here. The results for this case are shown in Figures 5.12 and 5.13.

Figure 5.12 shows that the effect of body blockage for the on-body COTS 'Rufa' antenna again greatly reduces the short-term peak-to-peak signal level fluctuations originally observed in Figure 5.9.

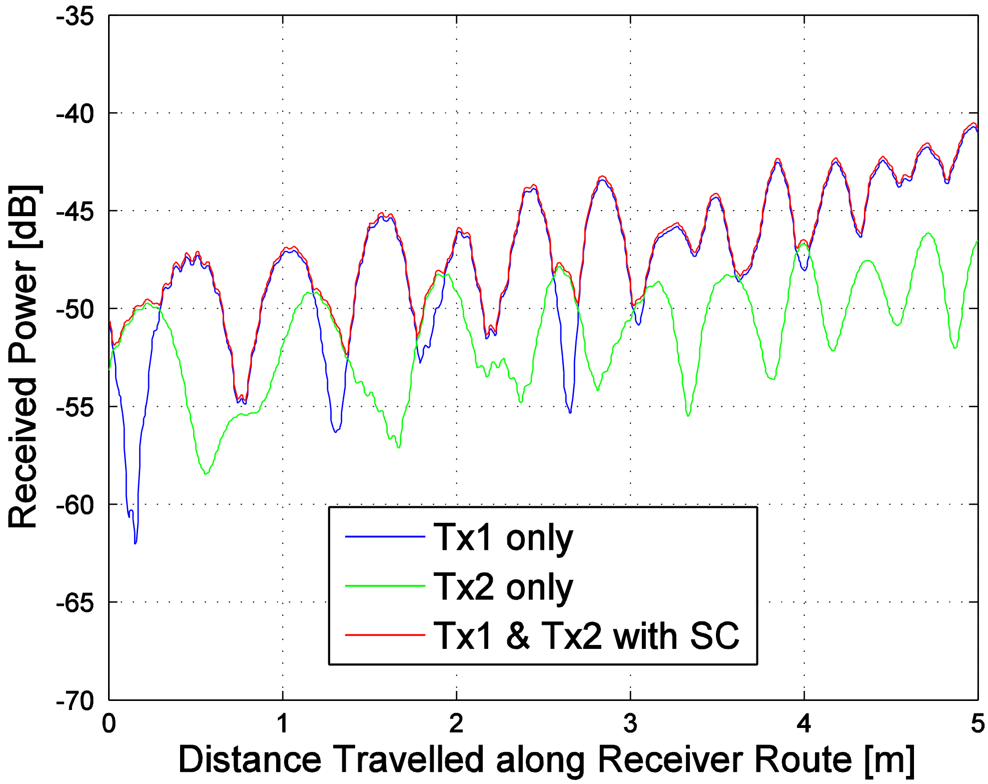

Figure 5.12: Received signal powers versus distance *with* and with*out* Off-body *Polarisation* Diversity for the *COTS 'Rufa' On*-body antenna

Now, in any *effective* diversity scheme not only must the signals in its individual branches be reasonably decorrelated, but also these signals must be of similar magnitude. For example, in the extreme case for a 2-branch diversity scheme in which the signal in one branch is zero due to some kind of permanent module malfunction, evidently there will be *no* diversity gain.

Figure 5.12 indicates that, although the signal levels in the individual branches have now become slightly more correlated than in the reference case previously in Figure 5.10, they are generally still reasonably decorrelated. However, the most obvious feature in Figure 5.10 is the typical 5dB difference in the signal levels within the individual branches associated with the two orthogonally-polarised off-body antennas Tx1 and Tx2 ('green' and 'blue' curves). This is due to the considerable difference in the co-polar and x-polar responses of the largely depolarised COTS 'Rufa' antenna when used on-body here, which has an average co-pol/x-pol ratio of about -6dB.

This degrading effect is reflected in the corresponding outage levels versus SNR plots shown in Figure 5.13 below. By comparison with Figure 5.11 for its equivalent reference case, it can be seen that the depolarised COTS 'Rufa' on-body antenna in Figure 5.13 again affords less off-body *polarisation* diversity gain than the original reference case with its 45°-pol dipole at the on-body end of the link. The relevant PDGs at the 1% and 2% link outage levels are 5.7dB and 3.4dB here for the 'Rufa' antenna, compared to 6.7 and 5.9dB previously for the ideal dipole antenna.

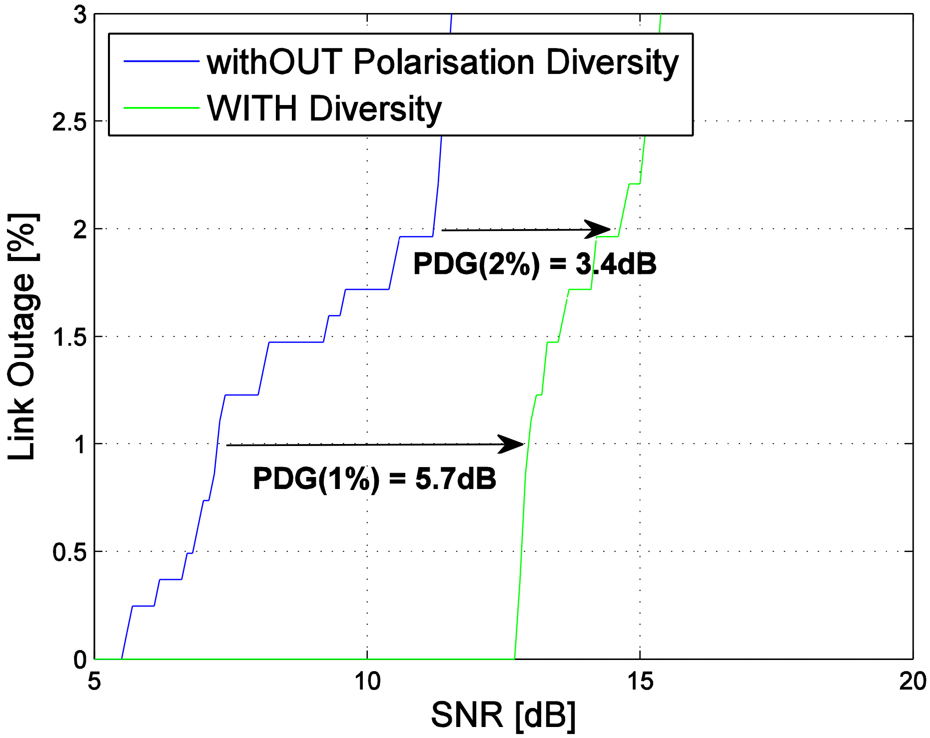

Figure 5.13: Link Outages versus SNR *with* and with*out* Off-body *Polarisation* Diversity for the *COTS 'Rufa' On*-body antenna

5.6.1 Effect of Rotating On-Body Antenna on *Polarisation* Diversity Gain

Given the imbalance in Figure 5.10 between the typical signal levels in the two signal branches in the polarisation diversity scheme (where the COTS 'Rufa' on-body antenna is rotated by 45°), the possible effect of rotating this on-body antenna to redress this imbalance was investigated.

Again, rather than reproducing a multiplicity of plot-pairs here, the key diversity gain results at 1% link outage are tabulated in Table 5.2 below. For comparison purposes, results for the equivalent reference case, having a 45°-pol *dipole* on-body antenna, are also included here.

Antenna Type at Body End of Link	On-body Antenna Rotation [°]	Diversity Gain at 1% outage [dB]	Correlation Coefficient
45° dipole (reference)	N/A (0)	6.7	0.22
COTS Candidate	0	**5.0**	0.55
	-10	5.7	0.31
	-20	5.0	0.02

Table 5.2: *Polarisation* Diversity Gains for Various Rotations of the on-body COTS 'Rufa' Antenna Compared to that of a Reference Dipole at 45° Pol

As intended, although not shown in Table 5.2, this rotation does indeed reduce the imbalance between the signal levels in the two branches.

Table 5.2 shows that rotating the on-body COTS 'Rufa' Antenna from its original 0° angle to -10° reduces the correlation between the signals in the two branches. As a result, the polarisation diversity gain *in*creases slightly from 5.0dB to 5.7dB at the 1% link outage level. Further rotation, from -10° to -20°, *de*creases the polarisation diversity gain from 5.7dB to 5.0dB, which confirms that the -10° rotation is optimum here.

However, this optimum -10° rotation may be specific to the particular 5m linear route considered here, and so may not be universally applicable. Also, in practice, since the angular orientation patient/client is likely to change in an unpredictable fashion, such a rotation technique to balance the signals in the two branches is unlikely to be robust/viable. Consequently, it is considered prudent to assume that the on-body COTS ‘Rufa’ antenna remains unrotated, in which case Table 5.2 indicates that the slightly non-optimum 0° antenna rotation with 5.0dB polarisation diversity gain is more typical of that likely to be experienced in practice.

5.7 Comparison of Simulated *Spatial* and *Polarisation* Diversity Schemes

Table 5.3 for *polarisation* diversity is reproduced below to allow direct comparison with the equivalent results for the case of *spatial* diversity, which are shown in Table 5.4.

Antenna Type at Body End of Link	On-body Antenna Rotation [°]	Diversity Gain at 1% outage [dB]	Correlation Coefficient
45° dipole (reference)	N/A (0)	6.7	0.22
COTS Candidate	0	**5.0**	0.55
	-10	5.7	0.31
	-20	5.0	0.02

Table 5.3: *Polarisation* Diversity Gains for Various Rotations of the on-body COTS ‘Rufa’ Antenna

Antenna Type at Body End of Link	Off-body Antenna Spacing [l]	Diversity Gain at 1% outage [dB]	Correlation Coefficient
V-pol dipole (reference)	0.75	8.0	0.69
	1.0	9.5	0.48
	1.5	8.7	0.53
COTS Candidate	1.0	8.1	0.51

Table 5.4: *Spatial* Diversity Gains for Various Separations of the off-body V-pol Dipole Antennas (derived from Figure 5.6)

It can be seen that, when the COTS 'Rufa' antenna is used at the body end of the link, *spatial* diversity provides (8.1 – 5.0) ≈ 3dB more diversity gain than *polarisation* diversity. For a given link performance, this extra 3dB diversity gain allows the on-body transmit power to be reduced by 3dB allowing at least a 2-fold increase in on-body battery lifetimes [95]. As a result, off-body *spatial* diversity (rather than the equivalent off-body polarisation diversity) is *preferred* here.

5.8 Possible Effects of COTS 'Rufa' On-body Antenna Orientation Due to Client/Patient Movement

The duration of this study has only permitted investigations with the on-body antenna pointing in the direction of travel along the specific linear route *towards* the off-body antennas shown earlier in Figure 5.1.

However, this near line of sight (LOS) link case cannot be assured for an arbitrary client/patient route. Consequently, for this reason, the link-budget given in section 5.2 previously assumed the worst-case blockage by the body (about 15dB) when using the MATLAB analysis to calculate the SNRs at different locations along the route.

Therefore, it is suggested that any further work should include a more detailed series of simulations to investigate different routes with a more comprehensive range off on-body antenna orientations to give a more truly representative statistical picture of a typical real-life scenario. This could be done using a modification to the existing Wireless Insite model, since the WI software package permits arbitrary route to be specified.

5.9 Geometrical Analysis of Physical Mechanism(s) to Explain the Behaviour Observed in the BCL Simulations

At this stage, having investigated the performance of the Wireless InSite model of the BCL, a partial geometrical *analysis* was undertaken to explain the main behaviour(s) observed in the results of received signal strength versus distance of these *simulations*. These behaviours include the long term trend, plus the medium and short term fluctuations.

The analysis here is *partial* in the sense that it only determines the relative *phases* of the direct and indirect components based on the geometry of the BCL and does not include signal amplitude considerations. As such, it identifies the spatial *locations* of peaks and nulls in the resultant signal as the on-body node moves along the chosen 5m linear route, but does not predict the composite signal amplitudes.

5.9.1 Long Term Trend

The long term trend observed in the WI *simulation* results of received signal strength versus distance along the patient/client route merely reflects the expected decreasing path-loss as the patient/client moves towards the fixed Access Point and distance between them decreases. Thus for example, at 5m along the route corresponding to the point of closest approach, the *mean* received signal strength is maximum; as observed in the simulation results.

The path-loss exponent here was obtained from best linear fits to plots of *log*(signal strength) (e.g. received signal strength (in dB) as given here) versus *log*(range). Although the details are not reported here, this gave an exponent of about:

$$\gamma = -2.0$$

which is not untypical of measured values in many multipath-rich indoor environments [91].

5.9.2 Medium Term Fluctuations

Because these medium-term fluctuations in the WI simulation results occur *less* rapidly (typically 2 periods per metre along the route), this suggests that they arise from interference between the direct LOS signal and the primary multipath signal arriving by means of reflection from a wall that is *laterally offset* from the direct path.

The geometry here is illustrated in Figure 5.14 which includes the direct signal and the primary multipath signal reflected from wall #3 adjacent to the Access Point. Also shown in this figure is the image of the Access Point antenna in the reflecting wall, which constitutes the apparent source of the reflected ray.

Straightforward geometry gives the path difference (ΔD) between the direct and multipath components here as:

$$\Delta D = \sqrt{((D' - D)^2 + (d_2 + d_1)^2)} - \sqrt{((D' - D)^2 + (d_2 - d_1)^2)} \qquad (5.7)$$

The variable D, being the x-axis in the graphs of received signal strength, is the distance travelled along the predefined patient/client route shown in Figure 5.14. Also, D’, d_1 & d_2 present in equation 5.7 are fixed dimensions in the BCL in the same figure.

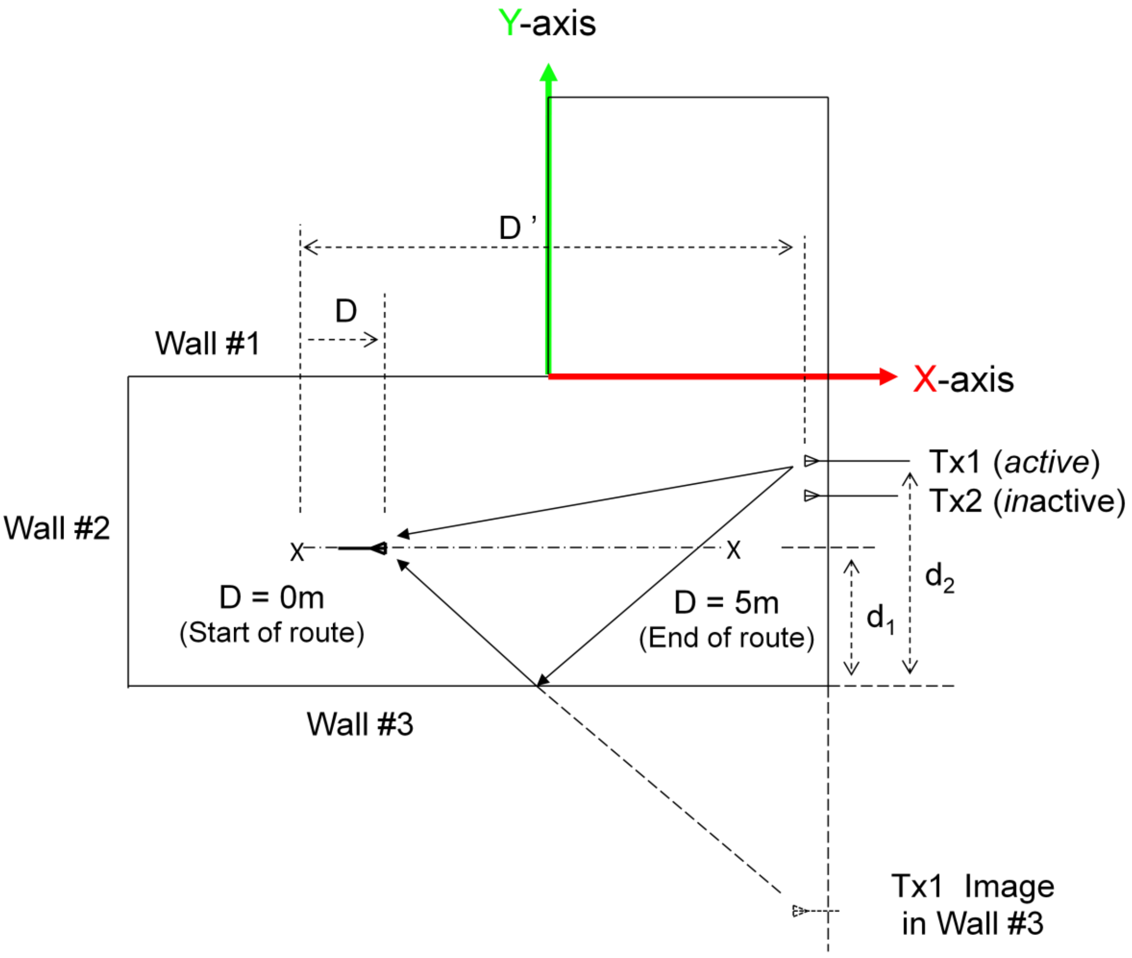

Figure 5.14: Geometry of Direct and Primary Multipath Signal Components for Reflection from Wall #3 Adjacent to the Off-body Access Point in Wireless InSite BCL Ray-Tracing Simulation Model

5.9.3 Short Term Fluctuations

Because these short-term fluctuations in the WI simulation results occur *more* rapidly (typically 16 periods per metre along the route), this suggests that they arise from interference between the direct LOS signal and the primary multipath signal arriving by means of reflection from a wall that is located *along* the direct path.

This situation is illustrated in Figure 5.15 which includes the direct signal and the primary multipath signal reflected from wall #2 now, which is directly opposite the Access Point. Again, the (different) image of the Access Point antenna in the reflecting wall that constitutes the apparent source of the reflected ray is also shown.

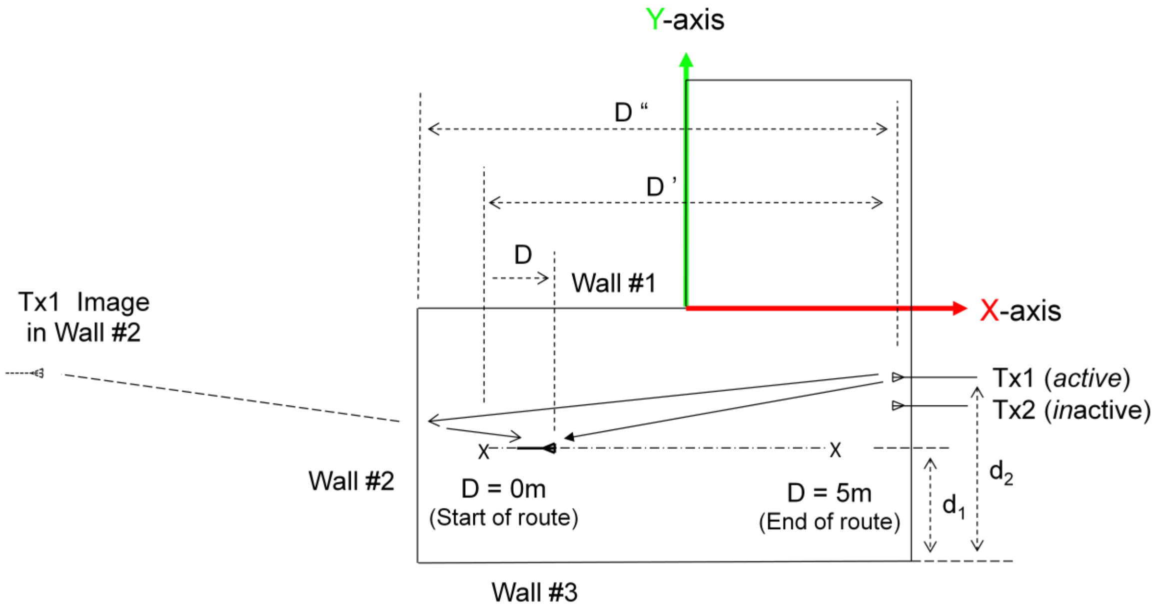

Figure 5.15: Geometry of Direct and Primary Multipath Signal Components for Reflection from Wall #2 Opposite to the Off-body Access Point in Wireless InSite BCL Ray-Tracing Simulation Model

In this case, straightforward geometry indicates that the path difference (ΔD) between the direct and multipath components is now given by:

$$\Delta D = \sqrt{((2D'' - D' + D)^2 + (d_2 - d_1)^2)} - \sqrt{((D' - D)^2 + (d_2 - d_1)^2)} \qquad (5.8)$$

As before, the variable D is the distance along the predefined patient/client route and D”, D’, d_1 & d_2 are fixed dimensions shown in Figure 5.15.

Again, the (different) image of the Access Point antenna in the reflecting wall that constitutes the apparent source of the reflected ray is also shown.

5.9.4 Results of this Partial Analysis

For the fluctuation cases considered here, values of the fixed parameters in the equivalent WI model of QMUL’s Body Centric Laboratory are:

D” = 8.26m

D’ = 6.46m

d_2 = 2.85m,

d_1 = 1.55m, and

f_c = 2.4482GHz.

The *path* differences between the direct and principal multipath components, given by equations 5.7 & 5.8 for the medium and short term fluctuation cases, are used to derive their *phase* differences by means of a simple ‘Excel’ spreadsheet computation. These phase differences are shown plotted versus the variable distance (D) along the route in Figure 5.16.

Evidently, a relative phase difference of 0° or 360° corresponds to a *constructive* vector combination (simple addition) of the direct and principal multipath components giving a maximum result, whilst 180° corresponds to a *destructive* vector combination (simple subtraction) associated with a minimum result. Finally, relative phases between these two extremes correspond to more complex vector combinations, giving intermediate results.

Now, Figure 5.16 shows that the phase difference cycles most rapidly (with 79 periods over the 5m route) for reflections from Wall #2 directly *opposite* to the Access Point. In addition, it is apparent that the phase difference cycles more slowly (with 12 periods over 5 metre) for reflections from Wall #3 *adjacent* to the Access Point.

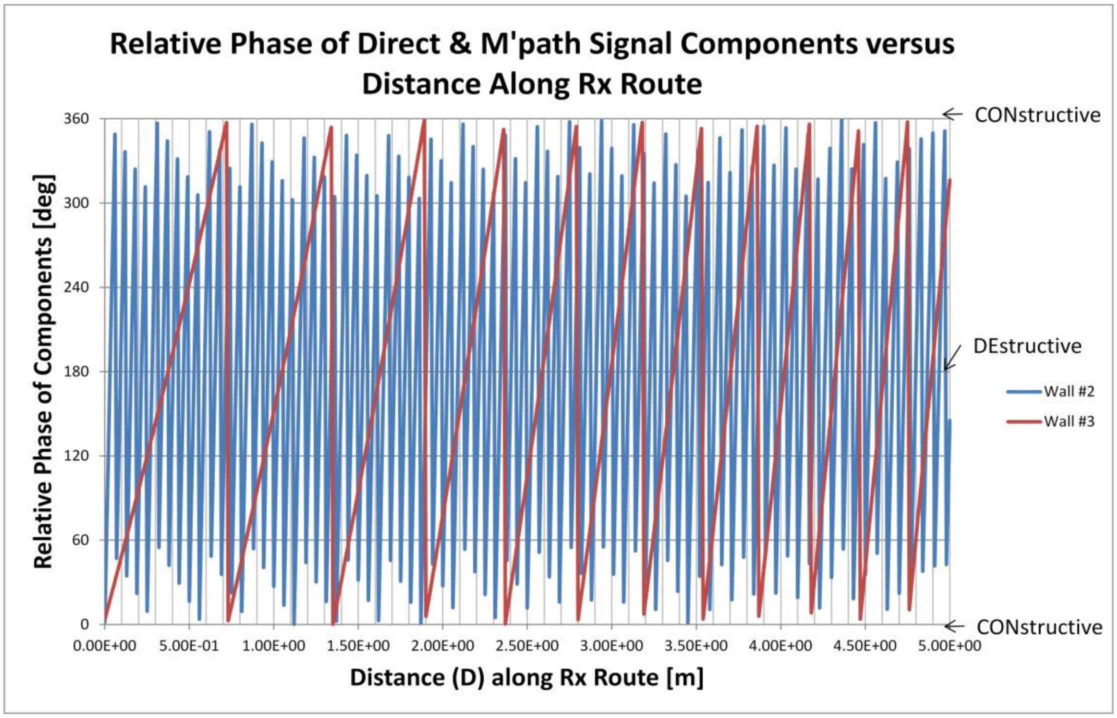

Figure 5.16: The Relative Phases between Direct and Principal Multipath Signal Components versus Distance along the Patient/Client Route in the BCL Simulation Model for Reflections from Wall #2 (blue) & Wall #3 (red)

Comparison of this partial geometrical *analysis* result is best made with the with*out* diversity result for the Wireless InSite BCL *simulations* given in Figure 5.4. All the antennas in Figure 5.4 (both off-body and on-body) are half-wave V-pol dipole types, having largely azimuthally omnidirectional patterns, which therefore produce the most marked signal strength fluctuations. Now Figure 5.4 shows 78 periods of rapid fluctuations and 11 periods of slower fluctuations over the 5m linear route, which agree remarkably well with the 79 and 12 periods over the same route in Figure 5.16 here for the partial geometrical analysis.

This agreement shows that the partial geometrical analysis provides a straightforward physical mechanism which explains the phases of the longer and short term fluctuations observed in the fuller analysis given by the Wireless InSite BCL model. It also constitutes further reassuring validation of this WI model.

As noted previously, the analysis here is 'partial' in that, for simplicity, it only considers the phases of the various direct and primary multipath signals and disregards their amplitudes. However the Wireless InSite BCL simulation is more 'full' in the sense that it includes relative amplitudes, as well as the phases, for up to 2 reflections.

5.10 Conclusions

In summary, this chapter, presenting the fairly comprehensive WI simulations with the associated MATLAB statistical analysis of their output data, has shown that:

i) Where multipath induced signal level fluctuations are high, and the separation between the two *off*-body antennas involved at the Access Point is such that they receive relatively uncorrelated signals, then the simple 2-branch *spatial* diversity proposed here can afford significant (typically 8dB) diversity gain.

ii) This diversity gain is essential for the present applications, since the link budget shows that, in its absence, to counter 20dB deep multipath fades would otherwise require an on-body transmit power level of about +0dBm at maximum range. This slightly exceeds the maximum -1.25dBm regulatory level allowed for use on a human body. The proposed use of spatial diversity permits this on-body transmit power to be reduced to a more acceptable -8dBm level.

iii) This reduction in on-body transmit powers afforded by spatial diversity gain is also very useful in the present applications because it affords greatly extended battery lifetimes for on-body nodes which need to be battery powered for maximum client/patient mobility.

iv) For the 2-branch diversity considered here, *spatial* diversity affords about 3dB more diversity gain than its equivalent *polarisation* diversity scheme. This 3dB difference is significant because, all other parameters being equal, on-body battery lifetimes with spatial diversity will be at least twice [95] as long as those with polarisation diversity. Therefore, *spatial* diversity is recommended for use here.

v) For the linear route investigated in the BCL scenario here, the optimum separation (providing maximum spatial diversity gain) between the two off-body antennas at the Access Point was found to be about 1.0λ. This separation corresponds to the minimum correlation coefficient of $\rho = 0.48$, so that, as expected, maximum spatial diversity gain is achieved when the signals in the two branches here are least correlated. At 2.45GHz, this electrical separation corresponds to a physical separation of about 1.2m, which is perfectly acceptable at the *off*-Body Access Point node in the selected SIMO link architecture. This would not be the case for the same element separation if a MISO scheme, having a pair of elements at the on-body end of the link had been selected

Alternatively, rather than using the spatial diversity gain to increase on-body battery lifetimes, it could instead be used to improve the system signal-to-noise ratio above the 8dB level required here to give an acceptable BER of (9×10^{-4}) with simple DPSK modulation. In more favourable propagation instances, this would allow use of a higher-level modulation scheme than the basic (M=2) DPSK scheme considered here. This could be useful for future applications involving the transmission of more complex information types (e.g. imagery snapshots [96]) requiring higher data-rates within the same 5MHz ISM channel bandwidths.

A final intriguing possibility is that the use of spatial diversity to reduce on-body node transmit powers might allow on-body node transmit powers to be reduced to the extent that these nodes might be powered by radically different means such as ‘energy-harvesting’ (with associated rechargeable batteries acting in a back-up capacity when energy-harvesting is temporarily unavailable).

Reference [97] indicates that current micro energy-harvesting technologies produce of order 0dBm power, which should be compatible with the -8dBm on-body transmit power level required here (when diversity is used to achieve this figure). Evidently, the successful application of such power sources would avoid the inconvenience and cost of having to change *non*-rechargeable on-body batteries, which would be a most welcome development.

Thermo-Electric Generators (TEG) or piezo-electric energy-harvesting technologies are two potential candidates here and chip-sized examples of these can be found in references [98] and [99]. The former rely on the difference between the body and ambient temperatures to generate electrical energy, whilst the latter would involve exploitation of body movement, such as chest expansion of any (living) patient/client.

Finally, reference [95] considers the lifetimes of a commonly-used coin cell in medical applications and shows that the use of Ultra Low Power design techniques, in particular the intelligent use of ‘sleep-modes’ when the wireless sensor node is not actually transmitting, can greatly increase the lifetime of such non-rechargeable batteries.

Chapter 6

Conclusions and Further Work

6.1 Overall Conclusions

Reasoning, based on a preliminary literature survey, showed that an initial Proof of Concept wireless solution for Telecare/Telemedicine use, should adopt a non-networked architecture topology having a dedicated link between each on-body sensor node and its associated Access Point node.

Subsequently, as wireless sensor techniques become more widely adopted in such applications, so that *multiple* wireless nodes on a common body become more commonplace, the node to node relaying advantages of a more complex networked topology could then be exploited.

Adopting a *standard* protocol at the outset, such as IEEE802.15.4 that already has provision for both topologies, would be advantageous to permit a smooth transition between them according to the availability (or otherwise) of multiple on-body nodes. In this regard, in addition to the *physical presence* (or absence) of multiple nodes, their *availability for use* will also vary according to the prevailing propagation environment; a factor which will change in real-time in any dynamic real-life scenario.

Similarly, reasoning based on the literature survey showed that the best *multi-antenna* architecture for use in the great majority of Telecare/Telemedicine applications, where data-rates are expected to be low, is a Single Input Multiple Output (SIMO) scheme. The simplest SIMO scheme, having a single *on*-body antenna and two *off*-body antennas was simulated in considerable detail here. This showed that such a SIMO scheme can provide a very useful (~9dB) spatial diversity gain, to partially offset deep multipath fading.

The single *on*-body antenna in this SIMO scheme provides the smallest size on-body wireless sensor node, thereby maximising user acceptability. Also, the simplicity of the *single* antenna on-body sensor in this scheme will also give the lowest on-body node cost. This is important from the system-provider's point-of-view in a system where these on-body nodes will be more numerous than their associated off-body Access Points. Further, for hygiene reasons, such on-body sensor nodes may also need to be disposable.

As *anticipated*, simulations and measurements conducted in the present study both confirm that the presence of the human body in close proximity to the *un*shielded COTS candidate 'Rufa' antenna (designed primarily for free-space use) produces a marked effect on this antenna's RF performance. In particular, the close proximity (~3mm) of the body severely reduces (~13dB) the antennas efficiency. Further, in the extreme case when the antenna is in *direct* contact with the human body, significant detuning (~13% reduction in resonant frequency) is also experienced.

More intriguingly, both simulations and measurements revealed a previously *un*reported effect of the nearby body on this unshielded antenna. This is that their otherwise reasonably polarised patterns in free-space (co/x-polar ratio ~13dB) become almost completely depolarised (co/x-polar ratio about -6dB) when located 3mm away from the body; i.e. a reduction of ~19dB. The discovery of this unanticipated effect of the body is of particular relevance to the PhD study here, and a paper including this finding was presented by the author at the EuCAP 2011 conference in Rome [20].

Subsequently, an analysis was conducted to explain this effect based on conventional Geometric Optics considerations. This predicted a 19.5dB *reduction* in the co/x-polar ratio, which is in remarkably close agreement with that observed in both measurements and simulations. Therefore, this conventional analysis, which only involves conventional space-wave propagation, is believed to represent a satisfactory physical explanation for the observed depolarising effect of the body. This is not meant to imply that propagation by more esoteric mechanisms, such as surface-waves, is not present here. Rather, if these mechanisms are active, their contribution to the overall picture must be of second-order significance. It is anticipated that a paper describing this depolarisation mechanism will be submitted shortly to AWPL for future publication.

The main conclusion of the present study is that, despite their lack of shielding from the nearby body, the 2.4GHz COTS 'Rufa' antenna can *still* be used in the on-body application here *provided certain steps are taken*. These are:

i) To ensure that the detuning of the antenna by the nearby body remains acceptable (i.e. its resonant frequency remains within the 2.4 GHz ISM-band) an intervening air or clothing (largely air) gap of 2mm or more should be included between the antenna and the body.

ii) To offset the efficiency reduction of the antenna by the nearby body, a mechanism providing additional gain must be provided to partially mitigate the severe (~20dB) multipath fading experienced in the multipath-rich indoor scenario here. This is mandatory; even for the favourable link budget here with the very short ranges (typically up to 5m) involved in the present applications.

The first proviso can easily be ensured, by providing a simple thin (~2mm) expanded polystyrene spacer between the body and the antenna, without unduly compromising the inherently low-profile nature of the COTS 'Rufa' antenna. This low-profile attribute is essential for user acceptability in the proposed on-body Telecare/Telemedicine applications.

To address the second proviso, without increasing on-body transmitted power with consequent reduction in limited on-body battery lifetimes, relatively straightforward *off*-body diversity techniques can be employed. The diversity gains afforded by such techniques (~9dB) can be used to partially offset the most severe multipath fades.

For this purpose, two diversity types (spatial and polarisation diversities) at the off-body Access Point and the effect of the depolarised on-body antenna have been simulated in the present study. This shows that, for an acceptable 1% link outage at a bit error rate of 10^{-3}, 9.5dB diversity-gain is realised by the use of spatial diversity, whilst 8.1dB is available using polarisation diversity. These diversity gains are in good agreement with those given in the literature (typically 9dB, although these were largely for outdoor environments). Both diversity schemes are equally simple to implement, involving a pair of antennas, or a single dual-polar antenna, at the less numerous off-body Access Point node (where space is also more readily available). Thus, use of the marginally more effective *spatial* diversity scheme is proposed here. A letter describing this has been submitted to Antennas Wireless and Propagation Letters (AWPL) for consideration for future publication.

The effect of relocating a closely-spaced *pair* of ‘Rufa’ COTS antennas from their conventional application in free-space to be in close proximity to the human body was also simulated and measured. Simulations and measurements both indicate that a substantial (3-fold) reduction in the spacing between the two antenna elements is possible for a given level of mutual coupling between the on-body element *pair*. This finding was reported in a paper by the present author at EuCAP 2011 [20].

Reference to this conference paper was also made by Prof. Simon Kingsley in a subsequent whitepaper in a recent trade journal [27]. This whitepaper indicated that the effect might allow link capacity enhancements, afforded by MIMO techniques, to be achieved for wireless equipped on-body sensor nodes employing *two* closely spaced antennas without commensurately increasing their overall size. However, in order to constrain the scope of this study, application aspects of this on-body mutual coupling reduction effect have not been considered further here.

In conclusion therefore, it is believed that the author’s two main aspirations formulated at the outset of this study have been largely achieved, namely:

i) To further expand the existing research knowledge base, and conduct the study in a sufficiently rigorous manner, to satisfy the requirements of a PhD, and
ii) To devise a technically sound and economically viable wireless link that satisfies the current urgent requirement for low data-rate wireless-equipped on-body sensors for use in nearer-term Telecare and Telemedicine applications.

6.2 Suggested Further Work

To further progress the work reported in this PhD study, the following items are suggested:

i) The Wireless Insite simulations of the overall *system* performance with a COTS ‘Rufa’ on-body antenna reported here are currently limited to a single linear route taken by the on-body wireless sensor node in the Body Centric Lab. Further, only one on-body antenna orientation has been thoroughly investigated (that giving V-pol in a free-space environment). Therefore, it is suggested that additional routes be investigated using this Wireless Insite simulation to determine whether the findings presented here are route-dependent, or whether the single route investigated so far is reasonably representative. Although non-trivial to implement, the WI software package does allow different routes and antenna orientations to be simulated. Naturally, the associated user-written MATLAB analysis programme would need to be rerun for each case considered.

ii) The Wireless Insite *simulation* results of the overall system performance given here should be validated by means of a complementary *measurement* programme. However, given the good reputation of the Wireless Insite software package, such verification need only comprise a limited number of representative cases.

iii) The CST *simulation* finding here that the area of the ‘Rufa’ COTS antenna evaluation board (and therefore the overall size of the on-body wireless node) can be halved without seriously detracting from its performance, should be confirmed by *measurements* on an antenna assembly whose evaluation board has been ‘cropped’. This cropping procedure should be conducted in an incremental fashion until such time as the on-body antenna assembly no longer performs in a satisfactory manner. Assuming that the size of the wireless aspect is the dominant factor in the on-body wireless sensor node, this exercise will serve to establish the overall size of the miniaturised sensor node.

iv) For on-body use in longer-term future Telecare/Telemedicine sensor applications, the use of more exotic artificial surface types, located between the unshielded antenna and the human body should be investigated. The shielding effect of such intervening surface types will significantly increase the antenna’s efficiency and therefore increase on-body battery lifetimes. Such artificial surface types should include Electromagnetic Band Gap (EBG) shields, which can be realised in thin planar form. These can be located much closer to the associated antenna than a conventional PEC GND-plane, which must be located h=(λ/4) away ((λ/4)≈30mm at 2.4GHz here). Hence, the use of such artificial surface types would not compromise the inherently low-profile (h≈2mm) nature of the COTS 'Rufa' antenna. This low-profile attribute is essential to ensure user-acceptability in Telecare/Telemedicine applications considered here.

v) The assertion in reference [27] that the reduced mutual coupling, observed between pairs of Rufa antenna when on-body, should allow MIMO capacity enhancements to be achieved within a smaller overall wireless sensor node (than would otherwise be possible in free-space) merits further consideration. This effect could be of particular significance for future generations of *in-hospital* Telemedicine links where increased data-rates afforded by MIMO techniques may be required (e.g. for 'snap-shot' imagery purposes). Further, the user inconvenience of these larger multi-element antennas is more likely to be tolerated by such *in*-patients. As usual, the customary initial literature search is suggested to determine whether any work in this area has previously been reported before embarking on more extensive investigations.

vi) For *in*-patient use, where the wearing of multiple on-body nodes on a common body is more likely to be tolerated by the patient, a more robust networking approach having the attendant advantages of relaying, could be explored using these multiple nodes in a Body Area Network (BAN). This approach could be particularly beneficial for largely static patients, for whom a particular adverse propagation condition for a single on-body node may prevail for an extended period of time.

vii) Finally, the work presented here uncovered the interesting depolarising effect of the body when in close proximity to the antenna. This was observed for two types of antenna, both of which were unshielded from the influence of the body and largely omnidirectional in azimuthal when in free-space. Further, this effect was also confirmed here to remarkable accuracy by an analysis which was conducted on the basis of a *modified* Geometric Optics approach and assuming only limited basic assumptions about the antenna characteristics. Whether this depolarisation effect is generic to all similar antenna types, also whether this analytical approach represents what is actually occurring in reality, might be an interesting topic for further study – if only at MSc level.

REFERENCES

[1] HM Government Whitepaper, 'Caring for our Future: Reforming Care and Support', ISBN: 9780101837828, July 2012, www.official-documents.gov.uk

[2] Frederix I., Dendale P., Berger J., Vandereyt F., Everts S. and Hansen D., 'Comparison of Two Motion Sensors for Use in Cardiac Telerehabilitation', Journal of Telemedicine and Telecare, Vol. 17, no. 5, pp 231-234.

[3] Smith J.M., 'The Doctor Will See You ALWAYS', IEEE Spectrum, October 2011, p51-55

[4] Lutz D., 'Wireless Network in Hospital Monitors Vital Signs', Wireless Design Online, August 5, 2011.

[5] Petroski H., 'The Essential Engineer: Why Science Alone Will Not Solve Our Global Problems', Knopf 2010.

[6] IEEE 802.15 Standards: Wikipedia Overview.

[7] 'First Cell Phone Based Post-Operative Orthopedics Surgery Monitoring Kit Announced by GENTAG Inc. and the CORE Institute', Wireless Design Online, May 18th 2011.

[8] IEEE 802.15.4™-2006: Wikipedia Overview.

[9] IEEE 802.15.4™-2006, 'Part 15.4: Wireless Medium Access Control (MAC) and Physical Layer (PHY) Specifications for Low-Rate Wireless Personal Area Networks (WPANs)', IEEE Computer Society, 8th September 2006.

[10] Gilason D., 'Zigbee Wireless Networking', ISBN: 978-0-7506-8597-9, Elsevier, 2009.

[11] ‘Wireless Design Online’ website: http://www.wirelessdesignonline.com/article.mvc/Bluetooth-Technology-Gets-Faster-with-Bluetoo-0001

[12] IEEE 802.15.3b-2005™, ‘Part 15.3: ‘Wireless Medium Access Control (MAC) and Physical Layer (PHY) Specifications for High Rate Wireless Personal Area Networks (WPANs): Amendment to MAC Sublayer’, IEEE Computer Society, 5th May 2006.

[13] Amadi-Shokouh J., and Caiming Qiu R., “Ultrawideband (UWB) Communications Channel Measurements – a Tutorial Review”, Int. J. Ultra Wideband Communications and Systems, Vol. 1, No. 1, 2009, pp 11-31.

[14] Fort A., Desset C., Ryckaert J., De Doncker P., Van Biesen l., Wambacq P., “Characterisation of the Ultra Wideband Body Area Propagation Channel”, Ultra-Wideband 2005, ICU 2005, pp 22-27.

[15] Alomainy A., Hao Y., Parini C. G., and Hall P.S., “Comparison Between Two Different Antennas for UWB On-Body Propagation Measurements”, IEEE Antennas and Wireless Propagation Letters, Vol. 4, 2005, pp 31-34.

[16] Serra A.A., Nepa P., Manara G., Tribellini G., Cioci S., “A Wide-Band Dual-Polarised Stacked Patch Antenna”, IEEE Antennas and Wireless Propagation Letters, Vol. 6, 2007, pp 141-142.

[17] Demming-Jannssen F., Raman A., and Hao Y., “UWB Antenna Simulation with CST MICROWAVE STUDIO”, CST UGM 2009.

[18] Murray R., ‘How to Write a Thesis’, Open University Press, 3rd printing, 2002, p52.

[19] Roelens L., Van den Bulke S., Joseph W., Vermeeren G. and Martens L., ‘Path loss model for wireless narrowband communications above flat platform’, Electronics Letters, 5th January 2006, Vol. 42, No. 1.

[20] Waddoup W.D., Alomainy A., Hao Y. and Dupuy J., ‘Effects of Using a Low-Cost COTS Antenna in Close Proximity to the Body’, EuCAP 2011, Rome, 11th - 15th April 2011, pp 3719-3722.

[21] Antenova, Rufa™ 2.4GHz SMD Antenna Part No. 3030A5887-01, Product Specification Sheet AE020157-M

[22] Hall M.P.M. Barclay L.W. and Hewitt M.T., 'Propagation of Radiowaves', IEE 1996, ISBN: 0 85296 819 1, Chapter 2.

[23] Nishimoto H., Ogawa Y., Nishimura T., Ogane T., 'Measurement-Based Performance Evaluation of MIMO Spatial Multiplexing in a Multipath-Rich Indoor Environment', IEEE Transactions on Antennas and Propagation, Vol. 55, Issue 12, pp 3677-3689.

[24] Hall P.S. and Hao Y., 'Antennas and Propagation for Body-Centric Wireless Communications', Artech House 2006, ISBN 1 58053 493 7, Ch 3 & Ch5.

[25] Khan I., Yu L., Nechayev Y.I., and S. Hall P.S., 'Space and Pattern Diversity for On-Body Communication Channels in an Indoor Environment at 2.45GHz', Antennas and Propagation, 2007, EuCAP 2007, pp 1-6.

[26] Chen Z. N., 'Antennas for Portable Devices', Wiley Press 2007, ISBN 978-0-470-03073-8.

[27] Ilvonen J., Kivekas O., Holopainen J., Valkonen R., Rasilainen K. and Vainikainen P., 'Mobile Terminal Antenna Performance With the User's Hand: Effect of Antenna Dimensioning and Location', IEEE Antennas and ireless Propagation Letters, Vol. 10, 2011, pp 772-775.

[28] Sani A., Rajab M., Foster R. and Hao Y., 'Antennas and Propagation for Implanted RFIDs for Pervasive Healthcare Applications', to be Published.

[29] Hao Y. and Hall P. S., 'On-Body Antennas and Propagation: Recent Development', IEICE Transactions and Communications, Vol. E91-B, June 2008, pp 1682-1688.

[30] Gampala G., Sammeta R. and Reddy C.J., 'A Thin Low-Profile Antenna Using a Novel High Impedance Ground Plane', Microwave Journal, Vol. 53, No. 7, July 2010, pp 70-79.

[31] Engheta N., Ziolkowski R.H., 'Metamaterials: Physics and Engineering Explorations', IEEE Press, 2006, ISBN: 13 978-0-471-76102-0, pp324-349.

[32] Kakoyiannis C.G., Constantinou P., and Gika P., ‘Mutual Coupling Reduction in Compact Arrays for Wireless Sensors via a Pre-fractal Defected Ground Structure’, Microwave Engineering Europe, April 2009, pp. 21-26.

[33] Sievenpiper D., Broas R., Yablonovitch E., ‘Antennas on High Impedance Ground Planes’, IEEE MTT-S Digest, 1999, p1245-1248.

[34] Simovski C.R., Ermutlu M.E., ‘Magnetic Properties of Novel High Impedance Surfaces’, IET Proceedings Microwave Antennas and Propagation, 2007, **1**, (1), pp. 190-197.

[35] Yang F., Rahmat-Samii Y., ‘Relection Phase Characteristics of the EBG Ground Plane for Low Profile Wire Antenna Applications’, IEEE Transactions on Antennas and Propagation, Vol. 51, No. 10, October 2003, pp. 2691-2702.

[36] Yang F., Rahmat-Samii Y., ‘Microstrip antennas Integrated with Electromagnetic Band-Gap Structures: A Low Mutual Coupling Design for Array Applications’, IEEE Transactions on Antennas and Propagation, Vol. 51, No. 10, October 2003, pp. 2936-2946.

[37] Hiranandani M.A., Yakolev A.B., Kishk A.A., ‘Artificial Magnetic Conductors Realised by Frequency-Selective Surfaces on a Grounded Dielectric Slab For Antenna Applications’, IET Proceedings Microwave Antennas and Propagation, Vol. 153, No. 5, October 2006, pp 487-492.

[38] Rajagopalan R., Rahmat-Samii Y., ‘On the Reflection Characteristics of a Reflectarray Element with Low-Loss and High-Loss Substrates’, IEEE Antennas and Propagation Magazine, Vol. 52, No. 4, August 2010, pp. 73-89.

[39] Clavijo S., Diaz R.E., and McKinzie W.E., ‘Design Methodology for Sievenpiper High-Impedance Surfaces: An Artificial Magnetic conductor for Positive Gain Electrically Small Antennas’, IEEE transactions on antennas and Propagation, Vol. 51, No. 10, October 2003, pp. 2678-2690.

[40] Feresidis A.P., Goussetis G., Wang S., Vardaxoglou J.Y.C., ‘Artificial Magnetic Conductor Surface and Their Application to Low-Profile High-Gain Planar antennas’, IEEE transactions on antennas and Propagation, Vol. 53, No. 1, January 2005, pp. 209-215.

[41] Kern D. J., Werner D.H., Monorchio A., Lanuzza L. and Wilhelm M.J., ‘The Design Synthesis of Multiband Artificial Magnetic Conductors Using High Impedance Frequency Selective Surfaces’, IEEE transactions on antennas and Propagation, Vol. 53, No. 1, January 2005, pp. 8-17.

[42] McKinzie W.E., Fahr R.R., 'A Low Profile Polarisation Diverse Antenna Built on an Artificial Magnetic Conductor', IEEE publication, pp. 762-764.

[43] Li Z., Rahmat-Samii Y., 'PBG, PMC and PEC Ground Planes: A Case Study of Dipole Antennas', IEEE publication, pp. 674-676.

[44] Fractal Antenna Systems Inc., 'Internal Wireless Antennas Take New Approach with Fractals', Wireless Design Online, October 1, 2010.

[45] Akhoondzadeh-Asl L., Hall P.S. and Nechayev Y., 'Wave Excitation on Human Body by a Short Dipole', EuCAP 2010, 12th-16th April 2010, pp 1-5.

[46] Kingsley S., 'Personal Healthcare Goes Wireless with Commercial 2.4GHz Technology', Electronics Weekly 16-22 May 2012, pp. 17-18.

[47] Roelens L., Van den Bulke S., Joseph W., Vermeeren G. and Martens L., 'Characterisation of Scattering Parameters Near a Flat Phantom for Wireless Body Area Networks', IEEE Transactions on Electromagnetic Compatibility, Vol. 50, No. 1, Feb 2008, pp 185 – 192.

[48] Schindler S., 'Introduction to MIMO', Application Note, Rhode & Schwarz, 07.2009-1MA142_0e.

[49] Chang W-J., Tarng J-H. and Pang S-Z., 'Frequency-Space-Polarisation on UWB MIMO Performance for Body Area Network Applications', IEEE Antennas and Wireless Propagation Letters, Vol. 7, 2008, pp 577-580.

[50] Akhoondzadeh L., Nechayev Y., Hall P.S., 'Surface and Creeping Waves Excitation by Body-Worn Antennas', 2010 Loughborough Antennas and Propagation Conference, 8-9 November 2010, pp 48-51.

[51] Morais D.H., 'Multiple Antenna Techniques Webcast', Adroit Wireless Strategies, www.BesserAssociates.com, 15th Dec 2011.

[52] Lackpour A., 'Maximising WLAN Range by Expoiting Two Types of Antenna Diversity', Oberon Wireless Inc., Whitepaper, p5.

[53] Poilasne G., Rowson S. and Desclos L., Ethertronics Inc., 'Implementing Antenna Diversity Inside Small Devices', EE Times 11th August 2002.

[54] Serra A. A., Nepa P., Manara G., and Hall P.S., “Diversity Measurements for On-Body Communications Systems”, IEEE Antennas and Wireless Propagation Letters, Vol. 6, pp. 361-363, 2007.

[55] Stein, S. et al., ‘Communication Systems and Techniques’, IEEE Book, Ch.10: Linear Diversity Combining Techniques, p416-489, Publication Year 2009.

[56] Rappaport T.S., ‘Wireless Communications: Principles and Practice’, Prentice Hall, Chapter 6, p325 – 345.

[57] Caimi F.M., Greer K. L., and Hendler J.M., “Antenna Diversity in Wireless Local Area Network Devices”, whitepaper on SkyCross website: http://www.skycross.com/Technology/whitepapers.asp

[58] Diggavi S.N., Al-Dhahir M., Stamoulis A. and Calderbank A.R., ’Great Expectations: The Value of Spatial Diversity in Wireless Networks’, Proc IEEE, Vol. 92, No. 2, February 2004, pp 219 - 270.

[59] Volakis J.L., Chen C-C., Fujimoto K., ‘Small Antennas: Miniaturisation Techniques and Applications’, McGraw-Hill, 2010, ISBN 978-0-07-162553-1, p192.

[60] Dargie W. and Poellabauer C., ‘Fundamentals of Wireless Sensor Networks’, Wiley 2010, ISBN 978-0-470-99765-9, Chapter 1.

[61] Huhn N., ‘Essentials of Short Range Wireless’, Cambridge University Press, 2010, ISBN 978-0-521-76069-0, Chapter 2.

[62] Rand P., ‘Achieving Good Co-existence in the 2.4GHz ISM band’, Microwave Engineering Europe, May 2008, pp 18-22

[63] Biglieri E., Goldsmith A., Muquet B. and Sari H., ‘Diversity, Interference Cancellation and Spatial Multiplexing in MIMO Mobile WiMAX Systems’, Mobile WiMAX Synposium, 2007, IEEE, pp 74-79.

[64] Yu, W. (Agilent Technologies), ‘Understanding the Impact of Spatial Effects on MIMO Wireless Channels’, RF Globalnet (www.rfglobalnet.com) newsletter, May 28, 2009.

[65] 'MIMO Channel Modeling and Emulation Test Challenges', Agilent Application Note, pp 1-60, http://cp.literature.agilent.com/litweb/pdf/5989-8973EN.pdf

[66] CST MICROWAVE STUDIO® 2011, 'Help' Manual, 'CST 2011 – Workflow and Solution Solver', p5.

[67] Garg R., 'Analytical and Computational Methods in Electromagnetics', ISBN-13: 978-1-59693-385-9, Chapter 10, pp 393-398.

[68] Weilland T., 'A Practical Guide to 3-D Simulation', IEEE Microwave Magazine, December 2008, pp 62-75.

[69] 'Computational Electromagnetics', Wikipedia Reference.

[70] 'Finite Element Method', Wikipedia reference.

[71] Wireless InSite Users Manual®, Release 2.5.14, March 2010, REMCOM™ Inc., Ch 6, pp 62-75.

[72] REMCOM™ Inc. Webinar, 'Wireless InSite: Urban Propagation Models', a summary of [71].

[73] Zhao Y., Sani A. and Hao Y., "A Simulation Environment for Subject-Specific Radio Channel Modelling in Wireless Body Sensor Networks", Body-Sensor-Networks Conference, 2009 (BSN 2009).

[74] Stratton J.A., 'Electromagnetic Theory', McGraw-Hill, 1942, Section 9-13, pp 516-520.

[75] Norton K.A., 'The Physical Reality of Space and Surface Waves in the Radiation Field of Radio Antennas', Proc Institute of Radio Engineers, Vol. 25, No 9, September 1937, pp 1192-1202.

[76] Balanis C.A., 'Antenna Theory Analysis and Design', Third edition, John Wiley & Sons, 2005, ISBN: 0-471-66782-X, p167.

[77] Hecht E., 'Theory and Problems of Optics', Schaum's Outline Series, McGraw Hill, 1975, ISBN 0-07-027730-3, Section 1.7, p15.

[78] Wigner E., 'The Unreasonable Effectiveness of Mathematics in the Natural Sciences', Communications in Pure and Applied Mathematics, Vol. 13, No. 1 (February 1960), John Wiley and Sons Inc., pp 1-13.

[79] Stratton J.A., 'Electromagnetic Theory', McGraw Hill, 1941, Section 8.5, pp 434-436.

[80] Hecht E., 'Theory and Problems of Optics', Schaum's Outline Series, McGraw Hill, 1975, Ch5 'Polarisation', pp 111-112, ISBN 0-07-027730-3.

[81] Ibid, Section 43-4, pp 944-946.

[82] Silver S., 'Microwave Antenna Theory and Design', Peter Peregrinus Ltd., 1984, section 6.3, pp 174-175.

[83] Wood B. and Pendry J.B., 'Directed Subwavelength Imaging Using a Layered Meta/Dielectric System', American Physical Society, Physical Review B 74, 115116 (2006)

[84] Ali W.K.W., Al-Charchafi S.H., 'Using Equivalent Dielectric Constant to Simplify the Analysis of Patch Dielectric Strip Antenna with Multi-Layer Substrates', APS International Symposium, 1998 IEEE.

[85] Longhurst R.S., 'Geometrical and Physical Optics', 2nd Edition, Longman, Green and Co., Ch 10, pp 194-202.

[86] Hall P.M., Barclay L.W. and Hewitt M.T., 'Propagation of Radiowaves', IEE Publications, equations (4.12) and (4.13), Chapter 4.7.2, pp 75-76.

[87] Spiegel M.R., 'Mathematical Handbook of Formulas and Tables', Schaum's Outline Series, 32nd printing, 1997, Equation 5.93, p19.

[88] The Wireless InSite Users Manual®, Release 2.5.14, March 2010, REMCOM™ Inc.

[89] Dama Y., Abd-Alhameed R., Salazar-Quinonez F., Zhou D., Jones S., Gao S., 'MIMO Indoor Propagation Prediction Using 3D Shoot-and-Bounce Ray (SBR) Tracing Technique for 2.4GHz and 5GHz', Proceedings on 5th European Conference on Antennas and Propagation, 2011, pp 1655-1658.

[90] Couch, L.W., 'Digital and Analogue Communication', Maxwell Macmillan, 3rd Edition, Table 7-1, p550.

[91] Morrow B., “Wireless Signal Propagation Analysis Made Easy”, Microwave Journal Webinar, 24th November 2009.

[92] Haller R.A., ‘FCC Regulations for Human Exposure to RF Fields’, IEEE Power Engineering Summer Society Summer Meeting 1999, Vol. 2, pp1355-1361.

[93] Sylla I., ‘Understanding Regulations when Designing a Wireless Product in the Unlicensed Frequency Bands’, Texas Instruments.

[94] Stein, S. et al., ‘Communication Systems and Techniques’, IEEE Book, Ch.10: Linear Diversity Combining Techniques, Figure 10-4-1, p437, Publication Year 2009.

[95] Furset K. and Hoffman P., ‘High Pulse Drain Impact on Coin Cell Capacity’, Ultra Low Power Wireless Quarterly, Nordic Semiconductors, winter 2011, pp 14-15 (part1), spring 2012, p 14 (part2), www.nordicsemi.com.

[96] ‘Given Imaging’ website: http://www.givenimaging.com/en-us/Patients/Pages/pageSmallBowel.aspx

[97] Raju M. and Grazier M., ‘ULP meets Energy Harvesting: A Game-Changing Combination for Design Engineers’, White Paper, Texas Instruments, ©2010.

[98] ‘eTEG™ UPF40 Thermoelectric Power Generator’ Preliminary Data Sheet, APS0011 rev 9.0, Nextreme Thermal Solutions Inc., www.nextreme.eu

[99] McAlpine M., ‘Piezo-Electric Ribbons Printed onto Rubber for Flexible Energy Conversion’, Nano Letters, American Chemical Society, Jan 26th 2009, pp524-529.

[100] Kakoyiannis C.G., Constantinou P., and Gika P., “Mutual Coupling Reduction in Compact Arrays for Wireless Sensors via a Pre-fractal Defected Ground Structure”, Microwave Engineering Europe, April 2009, pp 21-26.

[101] Rosengren K. and Kildal P. S., ‘Radiation efficiency, correlation, diversity gain and capacity of a six-monopole antenna array for a MIMO system: theory, simulation and measurement in a reverberation chamber’, IEEE Proceedings Microwave Antennas and Propagation, Vol 152, No. 1, February 2005, pp 7-16, equations (23) & (24).

[102] Stratton J.A., ‘Electromagnetic Theory’, McGraw-Hill, 1942, Sections 9.8 & 9.9, pp 500-516.

[103] Saunders S.R., ‘Antennas and Propagation for Wireless Communication Systems’, John Wiley and Sons, 1999, ISBN 0-471-98609-7, Section 3.5, pp 45-56.

[104] Volakis J.L., ‘A Uniform Geometrical Theory of Diffraction for an Imperfectly Conducting Half-Plane’, IEEE Transactions on Antennas and Propagation, 34(2), pp 172-180, 1986.

APPENDICES:

A1 Analysis Programme to Compute Diversity Gains

A listing of this analysis programme ‘test15_v2’, written using MATLAB by the present author, is included here for reference. This programme starts by reading in data-files generated by Wireless InSite simulations for a V-pol dipole on-body antenna having an ‘ideal’ azimuthally omnidirectional pattern. To do so, it initially derives filenames appropriate to this case.

A different variant, ‘test16_v2’, has different filenames and reads in WI generated data-files for the COTS ‘Rufa’ on-body antenna having more ‘realistic’ patterns with body blockage.

An outline of the function of these programmes, which derive Spatial Diversity Gain from simulated data generated by Wireless InSite, has been given earlier in Chapter 5.

```
%%%%%%%%%%%%%%%%%%%%%%%%%%%%%%%%%%%%%%%%%%%%%%%%%%%%%%%%%%%%%%%%%%%%%%%%
%%%
%
% test15_v2.m     - Description:
%           i)      Input variables
%           ii)     Determines filenames for two MODIFIED data-files
%                   corresponding to two OFF-body Tx antennas TX1 & TX2,
%                   for an input value of (TX1 / TX2) separation,
%           iii)    Reads these data-files,
%           iv)     Selects required column(s)of data from them,
%           v)      Performs SELECTIVE COMBINING on this required data,
%           vi)     Plots Rx'd power versus distance for TX1 only,
%                   TX2 only and selectively combined (TX1 & TX2),
%           vii)    Histogrammes SNR's WITH & withOUT diversity (SC)
%           viii)   Plots 'cdf's' of SNR's WITH & withOUT diversity (SC)
%           ix)     From 'cdf's' computes SNR's for specified outage-
level
%                   for WITH & withOUT diversity cases
%           x)      Computes diversity-gain, being difference of SNR's
%                   WITH & withOUT diversity
%
%%%%%%%%%%%%%%%%%%%%%%%%%%%%%%%%%%%%%%%%%%%%%%%%%%%%%%%%%%%%%%%%%%%%%%%%
%%%



% Initialisation process
clear all;      % Clears all VARBLS
clc;            % Clears COMMAND WINDOW
close all;      % Clears (previously open) figures
```

```
format;         % 15-bit precision, except where defined otherwise


% number of DATA lines in variable length 'DEHEADERED data file
num_data_lines = 815;
% N.B.  eventually this likely to be variable for more complex routes -
if
%       so, could use Frankie's 'extract_output.m' to derive this




% 1)        Inputting Variables
%
% 1.1)      Input average SNR for subsequent BER computation at average
%           range along section of Rx route here
av_SNR_withOUT_diversity = input('Input average SNR at mean range given
by link budget [dB]: ');

% 1.2)      Input TX1 - TX2 separation to select appropriate
%           TX1 and TX2 data-files output by Wireless InSite
Tx_sepn = input('Input TX1 - TX2 separation [lambda]: ', 's');




% 2)        Deriving file-names for TX1 and TX2 data-files output by
%           Wireless InSite using inputted TX1 - TX2 separation
%
filnam_var = num2str(Tx_sepn);

% 2.2.1)    Invariant initial part of filename (common to TX1 and TX2
data)
filnam_non_var_init = 'Modified_BCL_v5_';

% 2.2.2)    Final part of filename (common to both TX1 and TX2) data
filnam_non_var_end_Tx1 = 'lambda.power.t001_01.r002.p2m';
filnam_non_var_end_Tx2 = 'lambda.power.t001_02.r002.p2m';

% 2.2.3)    Combining various parts to give final filenames
filename_Tx1 = [filnam_non_var_init filnam_var filnam_non_var_end_Tx1]
filename_Tx2 = [filnam_non_var_init filnam_var filnam_non_var_end_Tx2]



% 3)    TX1 DATA
%
% 2.1)  FOR TX1 read in MODIFIED 'de-headered' ASCII data-file output
from
%       Wireless InSite simulation
filename_Tx1;
A = importdata(filename_Tx1);

% temporarily print it out first 5 rows of array 'A' for verification
for l = 1:5
    A_init(l,:) = A(l,:);
```

```
end
A_init;
% temporarily print it out last 5 rows of array 'A' for verification
for l = 1:5
    A_end(l,:) = A((num_data_lines-5)+l,:);
end
A_end;

% 2.2)  Extract particular columns of 'A' and put them into particular
%       column vectors each having 'num_rows' elements
A_col_5 = A(:,5);
A_col_6 = A(:,6);



% 4)    TX2 DATA
%
% 4.1)  FOR TX2 read in MODIFIED 'de-headered' ASCII data-file output
from
%       Wireless InSite simulation
filename_Tx2;
B = importdata(filename_Tx2);
% temporarily print it out first 5 rows of array 'B' for verification
for l = 1:5
    B_init(l,:) = B(l,:);
end
B_init;
% temporarily print it out last 5 rows of array 'B' for verification
for l = 1:5
    B_end(l,:) = B((num_data_lines-5)+l,:);
end
B_end;

% 4.2)  Extract particular columns of 'B' and put them into particular
%       column vectors each having 'num_rows' elements
B_col_5 = B(:,5);
B_col_6 = B(:,6);



% 5)    Concatenate these to form a single matrix with 3 columns for
%       subsequent diversity-gain processing

C = [A_col_5 A_col_6 B_col_6];
% temporarily print it out first 5 rows of array 'C' for verification
for l = 1:5
    C_init(l,:) = C(l,:);
end
C_init;
% temporarily print it out last 5 rows of array 'C' for verification
for l = 1:5
    C_end(l,:) = C((num_data_lines-5)+l,:);
end
C_end;
```

```
% 6)    Now do SELECTIVE COMBINING on the two Rx'd Signal Powers

for l = 1:num_data_lines
    if (C(l,2)>=C(l,3))
        D(l,1) = C(l,2);
    else
        D(l,1) = C(l,3);
    end
end



% 7)    Concatenate these to form a single matrix with 4 columns for
%       range, Rx1 power, Rx2 power, and power following SELECTIVE
%       COMBINING

E = [C D];
% temporarily print it out first 5 rows of array 'E' for verification
for l = 1:5
    E_init(l,:) = E(l,:);
end
E_init;
% temporarily print it out last 5 rows of array 'E' for verification
for l = 1:5
    E_end(l,:) = E((num_data_lines-5)+l,:);
end
E_end;



% 8)    Now plot out Rx'd power vs. distance travelled along the single
%       receiver route for :-
%       i)   TX1 only,
%       ii)  TX2 only and
%       iii) TX1 & TX2, following Selective-Combining
%       using information contained in the
%       ['num_data_lines' x 4] matrix 'E'

X_axis = E(:,1);
Y1x = E(:,2)-0.2;    % 0.2dB subtracted here to improve graph visibility
Y2x = E(:,3)-0.2;    % 0.2dB subtracted here to improve graph visibility
Y3x = E(:,4);        % nothing subtracted; so this represents true value
plot(X_axis, Y1x, 'b', X_axis, Y2x,'g', X_axis, Y3x, 'r');
xlim([0.0 5.0])      % Explicitly declare this for inter-graph
comparisons
ylim([-70 -35])      % Explicitly declare this for inter-graph
comparisons
plot_title = ['Received Power vs. Distance Travelled for TX1-TX2
Separation = ' filnam_var 'lambda'];
title (plot_title)
xlabel ('Distance Travelled along Receiver Route [m]')
```

```
ylabel ('Received Power [dB]')
legend ('TX1 only','TX2 only','TX1 & TX2 with SC')
grid on;




% 9)    Computing individual SNR's along the Rx route

% 9.1)  First compute AVERAGE signal POWER withOUT diversity and
distances
%       at locations along Rx route
F = mean(E(:,1));           % Ranges in 'E' are linear
for i = 1:num_data_lines
    for j = 2:4                        % Powers in 'E' are logarithmic
        G(i,j) = 10^(E(i,j)/10);    % powers in 'G' are linear
    end
end
I = mean(G);        % Average of linear powers in 'G'
J = (I(2)+I(3))/2;  % Average of mean powers for TX1 & TX2
K = 10*log10(I);    % Mean powers in 'K' are now logarithmic
K(1) = F;           % Overwrite 1st column of 'K' with mean distances
% temporarily print out 'L', giving mean distance, mean received powers
% for TX1 & TX2
K
av_range = K(1)
av_rx_pwr_withOUT_diversity = K(2)
av_rx_pwr_WITH_diversity = K(4)

% 9.2)  Next compute AVERAGE NOISE POWER level using inputted AVERAGE
SNR
%       withOUT diversity along Rx route and AVERAGE signal POWER
withOUT
%       diversity just computed
av_nse_pwr = av_rx_pwr_withOUT_diversity-av_SNR_withOUT_diversity

% 9.3)  Now compute three-col matrix 'L' having:
%       1st col - Ranges [km] along Rx route
%       2nd col - SNR's withOUT Diversity along Rx route TX1 only
%       3rd col - SNR's WITH Diversity along Rx route (TX1 & TX2)
% 9.2.1) 1st col - Ranges
L(:,1) = E(:,1);
% 9.2.2) 2nd col - SNR's withOUT Diversity
L(:,2) = E(:,2)-av_nse_pwr;
% 9.2.3) 3rd col - SNR's WITH Diversity
L(:,3) = E(:,4)-av_nse_pwr;
% temporarily print it out first 5 rows of array 'L' for verification
for l = 1:5
    L_init(l,:) = L(l,:);
end
L_init;
% temporarily print it out last 5 rows of array 'L' for verification
for l = 1:5
    L_end(l,:) = L((num_data_lines-5)+l,:);
end
L_end;
```

```
% 10)   Now compute outages vs. SNR's for WITH & withOUT diversity from
%       their CUMULATIVE 'pdf's and then plot them on a common graph for
%       direct comparison

% 10.1) TX1 only (i.e. withOUT diversity)
x = -15.0:0.1:30.0;     % Common to both plots
y1 = L(:,2);
n_elements = hist(y1,x);
c_elements_NO_div = cumsum(n_elements);
outage_NO_div_percent = 100*(c_elements_NO_div/num_data_lines);

% 10.2) TX1 & TX2 (i.e. WITH diversity (SC))
y2 = L(:,3);
n_elements = hist(y2,x);
c_elements_WITH_div = cumsum(n_elements);
outage_WITH_div_percent = 100*(c_elements_WITH_div/num_data_lines);

% 10.3  Now plot both outages (from 0 to 105%) WITH and withOUT
diversity
%       on common graph
figure;             % want a new figure - NOT OVERWRITE OLD ONE!
plot(x, outage_NO_div_percent, 'b',x, outage_WITH_div_percent, 'g');
xlim([-15 30])      % Explicitly declare this for inter-graph
comparisons
ylim([0 105])       % Explicitly declare this for inter-graph
comparisons
SNR_title =num2str(av_SNR_withOUT_diversity);
plot_title = ['Outage vs. SNR withOUT & WITH 2-Element Spatial-Diversity
(SC) for av(SNR) = ' SNR_title 'dB'];
title (plot_title);
xlabel ('SNR [dB]')
ylabel ('Outage [%]')
legend_title1 = ['withOUT Diversity'];
legend_title2 = ['WITH Diversity (TX1-TX2 Sep = ' filnam_var 'lambda)'];
legend (legend_title1,legend_title2);
grid on;

% 10.4  Now zoom-in to get picture at low outages (<3%, say)
figure;             % want a new figure - NOT OVERWRITE OLD ONE!
plot(x, outage_NO_div_percent, 'b',x, outage_WITH_div_percent, 'g');
xlim([-12 17])      % Explicitly declare this for inter-graph
comparisons
ylim([0 3])       % Explicitly declare this for inter-graph comparisons
SNR_title =num2str(av_SNR_withOUT_diversity);
plot_title = ['Outage vs. SNR withOUT & WITH 2-Element Spatial-Diversity
(SC) for av(SNR) = ' SNR_title 'dB'];
title (plot_title);
xlabel ('SNR [dB]')
ylabel ('Outage [%]')
legend_title1 = ['withOUT Diversity'];
legend_title2 = ['WITH Diversity (TX1-TX2) Sep = ' filnam_var
'lambda)'];
```

```
legend (legend_title1,legend_title2);
grid on;
```

A2 Alternative Derivation of Diversity Gain

Generally, diversity-gain is derived by comparing the curve of the BER versus SNR in the absence of diversity with the equivalent (improved) curve with diversity, with the diversity-gain being the difference in the two SNR's required to achieve a specific required BER. This process was described in Appendix A2 previously.

Usually, to derive these BER versus SNR curves multiple measurements of the system BERs must be made at different SNRs on the multiple antenna elements for different multipath scenarios. Alternatively the relationship between these parameters may be derived using simulations. However, in either case, obtaining these signal levels is a fairly involved procedure.

Instead, a potentially simpler method is included for discussion here, whereby diversity-gain might be derived directly from readily available measurements or simulations of the S-parameters of the antenna array to speed up this derivation.

Reference [98] gives an expression for the envelope correlation coefficient (ρ_c) in a 2-port network, comprising two antenna elements, in terms of its S-parameters as:-

$$\rho_c = |S_{1,1}^*.\ S_{1,2} + S_{2,1}^*.\ S_{2,2}|^2 \ / \ (1 - (|S_{1,1}|^2 + |S_{2,1}|^2)).(1 - (|S_{1,2}|^2 + |S_{2,2}|^2)) \qquad \text{(A2.1)}$$

Reference [99] gives an approximate expression for the apparent diversity gain (G_{app}) in a two element antenna system as:-

$$G_{app} = 10\ e_\rho = 10\ \sqrt{(1 - |0.99\ \rho_c|^2)} \qquad \text{(A2.2)}$$

So, by measuring or simulating the 2-port S-parameters of a two antenna element system *in the presence of typical source(s) of multipath*, equation (A2.1) above gives ρ_c which, in turn, can be inserted into equation (A2.2) to give the apparent diversity gain directly.

It is noted that equations (A2.1) or (A2.2) do not appear to include any *explicit* reference to parameters describing the multipath conditions. This would be of concern, since it is known that the available diversity-gain is strongly dependent on the prevailing multipath conditions; in particular, the absence of any multipath does not lead to any diversity-gain (other than the 3dB SNR free-space gain inherent in the use of the two element antenna array here).

However, the measured or simulated S-parameters *in the presence of multipath(s)* used here will inherently reflect the influence, of any multipath present. So, this concern is included in an *implicit* manner in the formulation here.

Nonetheless, limited measurements are planned shortly and will be analysed to ensure that the diversity gain obtained by conventional means agrees with that obtained from S-parameters using the method proposed here.

A3 Depolarisation Analysis Programme

A listing of this MATLAB programme ‘trial17.m’, written by the present author, is included here for reference. This programme evaluates the various formulae given in Chapter 4 (here) to derive the reduction in the average co/x-polar ratio of the ‘Rufa’ antenna when used on-body, rather than in Free-Space.

```
%%%%%%%%%%%%%%%%%%%%%%%%%%%%%%%%%%%%%%%%%%%%%%%%%%%%%%%%%%%%%%%%%%%%%%%%%
%%%
%
% 'trial17.m' :-
%
% i)     Computes mag(rho_perp), phse(rho_perp), mag(rho_para) and
%        phse(rho_para) for various GRAZING angles using equations (4.12)
%        & (4.13) in 'Propagation of Radiowaves', edited by Hall, Barclay
%        and Hewitt
% ii)    Using muscle dielectric properties and frequency as in 'Wave
%        Excitation on Human Body by a Short Dipole', Hall P.S. et al.,
%        EuCAP 2010
% iii)   Plots, reflection parameters versus angle of INCIDENCE w.r.t.
%        NORMAL
% iv)    Computes radii from point directly above dipole source on
%        illumination plane to common points of arrival of DIRECT and
%        INDIRECT rays from dipole source
% v)     Computes signal intensities on the basis of different distances
%        (radii) between illumination-plane intersection points for
%        different AoA's
% vi)    Finally computes ON-BODY Co/X-pol ratio, taking into account the
%        original Co/X-pol ratio of antenna when in FREE-SPACE
%
%%%%%%%%%%%%%%%%%%%%%%%%%%%%%%%%%%%%%%%%%%%%%%%%%%%%%%%%%%%%%%%%%%%%%%%%%
%%%

% Initialisation process
clear all;        % Clears all VARBLS
clc;              % Clears COMMAND WINDOW
close all;        % Clears (previously open) figures
format;           % 15-bit precision, except where defined otherwise

% 1)     Specifying programme constants
eps=52.7          % Dielectric permittivity
cond=1.77         % Dielectric conductivity [S/m]
freq=2.44175E9    % Frequency [Hz](Fc ISM band)
c=3E8;            % Free-Space velocity [m/s]
lambda=c/freq     % Wavelength [m]
h1=lambda/40      % Dipole source height 'above' air/dielectric interface
incr=1;           % Increment in grazing angle [deg]

% 2)        Inputting Variables
% Antenna Co/X-polar ratio when in FREE SPACE
```

```
FS_CoXpol_ratio_dB=input('Input antenna Co/X-polar ratio when in FREE
SPACE [dB]: ');
% Illumination plane height 'above' dipole source
h2_over_h1=input('Input (h2/h1) ratio: ');
h2=h1*h2_over_h1

% 3)    Initial computation to derive 'gamma' common to all angles
gamma=18E9*cond/freq;

% 4)    Computing storage array(s) size for specified increments in
%       grazing angle, given maximum grazing amgle
deg_max=90.01;
a_max=round(deg_max/incr);

% 5)    Step in grazing angle increments of from 0 to 40deg to give
%       magnitudes and phases for perp-pol versus grazing angle

for a=1:1:a_max;
    graze_ang_deg=incr*(a-1);
    AoA_deg=(90-graze_ang_deg);
    AoA_rad=AoA_deg*pi/180;
    graze_ang_rad=graze_ang_deg*pi/180;
    A=sin(graze_ang_rad);                             % real
    B=sqrt((eps-gamma*1i)-(cos(graze_ang_rad))^2);    % complex
    rho_perp_pol=(A-B)/(A+B);                         % complex
    re_rho_perp_pol=real(rho_perp_pol);               % real
    im_rho_perp_pol=imag(rho_perp_pol);               % real
    mag_rho_perp_pol=abs(rho_perp_pol);               % real
    phs_rho_perp_pol_rad=angle(rho_perp_pol);         % real
    phs_rho_perp_pol_deg=phs_rho_perp_pol_rad*180/pi; % real
    %   Constrain phases to be in range [0,-180] for comparison with
    %   those in Barclay et al., Fig 4.19 or Fig ?.? in Saunders
    if(phs_rho_perp_pol_deg>0)
        phs_rho_perp_pol_deg=phs_rho_perp_pol_deg-360;
    end
    perp_pol(a,1)=AoA_deg;
    perp_pol(a,2)=mag_rho_perp_pol;
    perp_pol(a,3)=re_rho_perp_pol;
    perp_pol(a,4)=im_rho_perp_pol;
    perp_pol(a,5)=phs_rho_perp_pol_deg;
end
% perp_pol

% 6)    Step in grazing angle increments of from 0 to 40deg to give
%       magnitudes and phases for V-pol versus grazing angle
for a=1:1:a_max
    graze_ang_deg=incr*(a-1);
    graze_ang_rad=graze_ang_deg*pi/180;
    C=(eps-gamma*1i)*sin(graze_ang_rad);            % complex, now
    D=sqrt((eps-gamma*1i)-(cos(graze_ang_rad))^2);  % complex
    rho_para_pol=(C-D)/(C+D);                           % complex
    re_rho_para_pol=real(rho_para_pol);                     % real
    im_rho_para_pol=imag(rho_para_pol);                     % real
    mag_rho_para_pol=abs(rho_para_pol);                     % real
    phs_rho_para_pol_rad=angle(rho_para_pol);               % real
```

```
    phs_rho_para_pol_deg=phs_rho_para_pol_rad*180/pi;        % real
    %   Constrain phases to be in range [0,-180] for comparison with
    %   those in Barclay et al., Fig 4.19
    if(phs_rho_para_pol_deg>0)
        phs_rho_para_pol_deg=phs_rho_para_pol_deg-360;
    end
    para_pol(a,1)=AoA_deg;
    para_pol(a,2)=mag_rho_para_pol;
    para_pol(a,3)=re_rho_para_pol;
    para_pol(a,4)=im_rho_para_pol;
    para_pol(a,5)=phs_rho_para_pol_deg;
end
% Vpol

% 7)    Plot out Reflection AMPLITUDES vs. Grazing Angle for :-
%       i)   perp-pol,
%       ii)  para-pol
%       on a common plot using information contained in the
%       [a_max x 5] matrices 'perp_pol' & 'para_pol'

X_axis = perp_pol(:,1);
Y1x = perp_pol(:,2);
Y2x = para_pol(:,2);
plot(X_axis, Y1x, 'b', X_axis, Y2x,'g')

xlim([0.0  90.0])         %  Explicitly  declare  this  for  inter-graph
comparisons
ylim([0  1.0])              %  Explicitly  declare  this  for  inter-graph
comparisons
xlabel ('Angle of Arrival (w.r.t. Normal) [deg]','fontsize',14)
ylabel ('Reflected Amplitude [ratio]','fontsize',14)
legend_title1 = '\fontsize{14}perp-pol';
legend_title2 = '\fontsize{14}para-pol';
legend (legend_title1,legend_title2,'Location','Best')
grid on;

% 8)    Now plot out Reflection PHASES vs. Grazing Angle for :-
%       i)   perp-pol,
%       ii)  para-pol
%       on a common plot using information contained in the
%       [a_max x 5] matrices 'perp_pol' & 'para_pol'

figure;               % Want a new figure - don't want to overwrite old
one
X_axis = perp_pol(:,1);
Y1x = perp_pol(:,5);
Y2x = para_pol(:,5);
plot(X_axis, Y1x, 'b', X_axis, Y2x,'g')

xlim([0.0  90.0])         %  Explicitly  declare  this  for  inter-graph
comparisons
ylim([-200 0])    % Explicitly declare this for inter-graph comparisons
xlabel ('Angle of Arrival (w.r.t. Normal) [deg]','fontsize',14)
ylabel ('Reflected Phase [deg]','fontsize',14)
legend_title1 = '\fontsize{14}perp-pol';
```

```
legend_title2 = '\fontsize{14}para-pol';
legend (legend_title1,legend_title2,'Location','Best')
grid on;

% 9)    Step in grazing angle increments of 1deg to give radius (R) to
%       common point of arrival on illumination-plane of DIRECT and
%       INDIRECT rays from dipole source
for a=1:1:a_max     % sec(AoA) tends to infinity for for AoA=90deg (a=1)
    graze_ang_deg=incr*(a-1);
    AoA_deg=(90-graze_ang_deg);
    AoA_rad=AoA_deg*pi/180;
    R(a,1)=AoA_deg;
    R(a,2)=(sqrt(((2*h1+h2)^2)*((sec(AoA_rad))^2)-4*h1*(h1+h2)-
h2^2))/lambda;
end
R(1,2)=100;          % say - tends to infinity for AoA=90deg (a=1)
% R

% 10)    Now plot out Radii vs. AoA w.r.t. NORMAL (0 to 85 [deg]) for
BOTH
%       compts using information contained in the [a_max x 2] matrix 'R'
figure;               % Want a new figure - don't want to overwrite old
one
X = R(:,1);
Y = R(:,2);
plot(X, Y, 'k')

xlim([0.0  85.0])         %  Explicitly declare this for inter-graph
comparisons
%ylim([0 1.0])    % Explicitly declare this for inter-graph comparisons
xlabel ('Angle of Arrival (w.r.t. Normal) [deg]','fontsize',14)
ylabel ('Radii in Aperture Plane [lambda]','fontsize',14)
% legend_title1 = '\fontsize{14}TBD';
% legend_title2 = '\fontsize{14}TBD';
% legend (legend_title1,legend_title2,'Location','Best')
grid on;

% 11)   Compute PATH length [lambda] for DIRECT ray at common point of
%         arrival on illumination-plane where DIRECT and INdirect rays
from
%       dipole source intersect this plane
for a=1:1:(a_max+1)
    graze_ang_deg=incr*(a-1);
    AoA_deg=(90-graze_ang_deg);
    AoA_rad=AoA_deg*pi/180;
    Path_DIR(a,1)=AoA_deg;
    Path_DIR(a,2)=(sqrt((sec(AoA_rad)^2)*((2*h1+h2)^2)-
4*h1*(h1+h2)))/lambda;
end
Path_DIR(1,2)=100; % say - tends to infinity for AoA=90deg (a=1)
% Path_DIR

% 12)   Compute PATH length [lambda] for INdirect ray at common point of
%         arrival on illumination-plane where DIRECT and INdirect rays
from
```

```
%       dipole source intersect this plane
for a=1:1:(a_max+1)
    graze_ang_deg=incr*(a-1);
    AoA_deg=(90-graze_ang_deg);
    AoA_rad=AoA_deg*pi/180;
    Path_INdir(a,1)=AoA_deg;
    Path_INdir(a,2)=((2*h1+h2)*(sec(AoA_rad)))/lambda;
end
Path_INdir(1,2)=100; % say - tends to infinity for AoA=90deg (a=1)
% Path_INdir

% 13)   Plot PATH lengths [lambda] for DIRECT and INdirect rays vs. AoA
%       w.r.t. NORMAL (0 to 85 [deg])
figure;                 % Want a new figure - don't want to overwrite old
one
X = Path_INdir(:,1);
Y1 = Path_INdir(:,2);
Y2 = Path_DIR(:,2);
plot(X, Y1, 'b',X, Y2,'g');
xlim([0.0  85.0])         %  Explicitly  declare  this  for  inter-graph
comparisons
%ylim([0  1.0])            %  Explicitly  declare  this  for  inter-graph
comparisons
xlabel ('Angle of Arrival (w.r.t. Normal) [deg]','fontsize',14)
ylabel ('Ray Path Length [lambda]','fontsize',14)
legend_title1 = '\fontsize{14}INdirect Path';
legend_title2 = '\fontsize{14}DIRECT Path';
legend (legend_title1,legend_title2,'Location','Best')
grid on;

% 14)   Now compute TOTAL Phases [deg] for INdirect and DIRECT ray paths
%           including  different  phases  for  para-pol  and  perp-pol  on
reflection of
%       INdirect rays from dielectric
for a=1:1:a_max
    Phse_DIR(a,1)=Path_DIR(a,1);
    Phse_DIR(a,2)=360*Path_DIR(a,2);
    Phse_INdir_para_pol(a,1)=Path_INdir(a,1);
    Phse_INdir_para_pol(a,2)=(360*Path_INdir(a,2))+para_pol(a,5);
    Phse_INdir_perp_pol(a,1)=Path_INdir(a,1);
    Phse_INdir_perp_pol(a,2)=(360*Path_INdir(a,2))+perp_pol(a,5);
    % Ensure that these lie in region 0deg to -180 for compatibility
    %                 Phse_INdir_para_pol(a,2)=Phse_INdir_para_pol(a,2)-
180*round(Phse_INdir_para_pol(a,2)/180);
    %                 Phse_INdir_perp_pol(a,2)=Phse_INdir_perp_pol(a,2)-
180*round(Phse_INdir_perp_pol(a,2)/180);
end
% Phse_DIR
% Phse_INdir_para_pol
% Phse_INdir_perp_pol

% 15)   Now plot out TOTAL PHASES vs. AOA w.r.t NORMAL for DIRECT and
%        INdirect paths on a common plot using information contained in
the
%                      matrices   'Phse_DIR',   'Phse_INdir_perp_pol'   &
'Phse_INdir_para_pol'
```

```
figure;                % Want a new figure - don't want to overwrite old
one
X_axis = perp_pol(:,1);
Y1x=Phse_DIR(:,2);
Y2x = Phse_INdir_perp_pol(:,2);
Y3x = Phse_INdir_para_pol(:,2);
plot(X_axis, Y1x, 'r',X_axis, Y2x, 'b', X_axis, Y3x,'g')

xlim([0.0 85.0])  % Explicitly declare this for inter-graph comparisons
%  ylim([-200  0])        %  Explicitly  declare  this  for  inter-graph
comparisons
xlabel ('Angle of Arrival (w.r.t. Normal) [deg]','fontsize',14)
ylabel ('Ray Path Phase [deg]','fontsize',14)
legend_title1 = '\fontsize{14}DIRECT Path (para or perp-pol)';
legend_title2 = '\fontsize{14}INdirect Path (perp-pol)';
legend_title3 = '\fontsize{14}INdirect Path (para-pol)';
legend (legend_title1,legend_title2,legend_title3,'Location','Best')
grid on;

% 16)    Now Compute (relative) AMPLITUDES of DIRECT and INdirect rays,
at
%       the point where they intersect on the illumination plane, for
%       different AOAs w.r.t NORMAL. This assumes that these scale
%       according to SQRT(path length) for CYLINDRICAL wavefronts here.
%       Also included for the INdirect rays are the different magnitudes
%       of the reflection coefficients for para-pol and perp-pol
for a=1:1:a_max
    Ampl_DIR(a,1)=Path_DIR(a,1);
    %Ampl_DIR(a,2)=Path_DIR(a,2);
    Ampl_DIR(a,2)=sqrt(Path_DIR(a,2));
    Ampl_INdir_para_pol(a,1)=Path_INdir(a,1);
    %Ampl_INdir_para_pol(a,2)=(para_pol(a,2))*Path_INdir(a,2);
    Ampl_INdir_para_pol(a,2)=(para_pol(a,2))*(sqrt(Path_INdir(a,2)));
    Ampl_INdir_perp_pol(a,1)=Path_INdir(a,1);
    %Ampl_INdir_perp_pol(a,2)=(perp_pol(a,2))*Path_INdir(a,2);
    Ampl_INdir_perp_pol(a,2)=(perp_pol(a,2))*(sqrt(Path_INdir(a,2)));
end
% Ampl_DIR
% Ampl_INdir_para_pol
% Ampl_INdir_perp_pol

%  17)     Now  plot  out  (relative) AMPLITUDES vs. AOA w.r.t NORMAL  for
DIRECT
%        and INdirect paths on a common plot using information contained
in
%       the matrices 'Ampl_DIR', 'Ampl_INdir_perp_pol'
%       & 'Ampl_INdir_para_pol'
figure;                % Want a new figure - don't want to overwrite old
one
X_axis=perp_pol(:,1);
Y1x=Ampl_DIR(:,2);
Y2x=Ampl_INdir_perp_pol(:,2);
Y3x=Ampl_INdir_para_pol(:,2);
plot(X_axis, Y1x, 'r',X_axis, Y2x, 'b', X_axis, Y3x,'g')
```

```
xlim([0.0 85.0])  % Explicitly declare this for inter-graph comparisons
% ylim([-200 0])  % Explicitly declare this for inter-graph comparisons
xlabel ('Angle of Arrival (w.r.t. Normal) [deg]','fontsize',14)
ylabel ('Ray Path Relative Amplitude','fontsize',14)
legend_title1 = '\fontsize{14}DIRECT Path (para or perp-pol)';
legend_title2 = '\fontsize{14}INdirect Path (perp-pol)';
legend_title3 = '\fontsize{14}INdirect Path (para-pol)';
legend (legend_title1,legend_title2,legend_title3,'Location','Best')
grid on;

% 18)   Do vector summation of DIRECT and INdirect components to give
%       Resultant Vectors for perp-pol and para-pol
for a=1:1:a_max
    % perp-pol  RESULTANT:  DIRECT  compt  +  perp-pol  compt  of  INdirect
compt

Re_RES_perp_pol(a,2)=(Ampl_DIR(a,2))*cos((pi/180)*Phse_DIR(a,2))+(Ampl_I
Ndir_perp_pol(a,2))*cos((pi/180)*Phse_INdir_perp_pol(a,2));

Im_RES_perp_pol(a,2)=(Ampl_DIR(a,2))*sin((pi/180)*Phse_DIR(a,2))+(Ampl_I
Ndir_perp_pol(a,2))*sin((pi/180)*Phse_INdir_perp_pol(a,2));

Mag_RES_perp_pol(a,2)=sqrt((Re_RES_perp_pol(a,2))^2+(Im_RES_perp_pol(a,2
))^2);

Phse_RES_perp_pol(a,2)=atan(Im_RES_perp_pol(a,2)/Re_RES_perp_pol(a,2));
    % para-pol  RESULTANT:  DIRECT  compt  +  para-pol  compt  of  INdirect
compt

Re_RES_para_pol(a,2)=(Ampl_DIR(a,2))*cos((pi/180)*Phse_DIR(a,2))+(Ampl_I
Ndir_para_pol(a,2))*cos((pi/180)*Phse_INdir_para_pol(a,2));

Im_RES_para_pol(a,2)=(Ampl_DIR(a,2))*sin((pi/180)*Phse_DIR(a,2))+(Ampl_I
Ndir_para_pol(a,2))*sin((pi/180)*Phse_INdir_para_pol(a,2));

Mag_RES_para_pol(a,2)=sqrt((Re_RES_para_pol(a,2))^2+(Im_RES_para_pol(a,2
))^2);

Phse_RES_para_pol(a,2)=atan(Im_RES_para_pol(a,2)/Re_RES_para_pol(a,2));
end

% 19)    Now plot out RESULTANT (MAGNITUDES and PHASES) vs. AOA w.r.t
NORMAL
%          for perp-pol and para-pol components on a common plot using
information
%                    contained   in   the   matrices   'Mag_RES_perp_pol'&
'Phse_RES_perp_pol' plus
%       'Mag_RES_para_pol'& 'Phse_RES_para_pol'
figure;                 % Want a new figure - don't want to overwrite old
one
X_axis=perp_pol(:,1);
Y1x=Mag_RES_perp_pol(:,2);
Y2x=Phse_RES_perp_pol(:,2);
Y3x=Mag_RES_para_pol(:,2);
Y4x=Phse_RES_para_pol(:,2);
```

```
plot(X_axis, Y1x, '--b',X_axis, Y2x, 'b', X_axis, Y3x,'--g', X_axis,
Y4x,'g')
xlim([0.0 85.0])  % Explicitly declare this for inter-graph comparisons
% ylim([-200 0])  % Explicitly declare this for inter-graph comparisons
xlabel ('Angle of Arrival (w.r.t. Normal) [deg]','fontsize',14)
ylabel ('Resultant Relative Amplitude / Phase [rads]','fontsize',14)
legend_title1 = '\fontsize{14}Resultant MAG (perp-pol)';
legend_title2 = '\fontsize{14}Resultant PHSE (perp-pol)';
legend_title3 = '\fontsize{14}Resultant MAG (para-pol)';
legend_title4 = '\fontsize{14}Resultant PHSE (para-pol)';
legend
(legend_title1,legend_title2,legend_title3,legend_title4,'Location','Bes
t')
grid on;

% 20)   Differences between radii of common intersection points on
%       illumination plane
for a=1:1:(a_max-1)
    R(a,3)=R(a,2)-R((a+1),2);
end
% R

% 21)   Calculate normalised (ampl)^2 on basis of radii differences,
%             assuming fixed increments in orthogonal plane, to give
intensities
%       for corresponding AoA's
for a=1:1:(a_max-1)
    I_RES_perp_pol(a,1)=R(a,1);
    I_RES_perp_pol(a,2)=(Mag_RES_perp_pol(a,2))^2/R(a,3);
    I_RES_perp_pol(a,2)=I_RES_perp_pol(a,2)/10;
    %I_RES_perp_pol(a,3)=phse_RES_perp_pol(a,2);
    I_RES_para_pol(a,1)=R(a,1);
    I_RES_para_pol(a,2)=(Mag_RES_para_pol(a,2))^2/R(a,3);
    I_RES_para_pol(a,2)=I_RES_para_pol(a,2)/10;
    %Phase_RES_para_pol(a)=phse_RES_para_pol(a,2);
end
I_RES_perp_pol(90,2)=150; % (say, at AoA = 0deg) to make arrays equal
length
I_RES_para_pol(90,2)=100; % (say, at AoA = 0deg) to make arrays equal
length
% I_RES_perp_pol
% I_RES_para_pol

% 22)    Now plot out RESULTANT (INTENSITY and PHASE) vs. AOA w.r.t
NORMAL
%          for perp-pol and para-pol components on a common plot using
information
%                    contained in the matrices 'Mag_RES_perp_pol'&
'Phse_RES_perp_pol' plus
%       'Mag_RES_para_pol'& 'Phse_RES_para_pol'
figure;                 % Want a new figure - don't want to overwrite old
one
X_axis=I_RES_perp_pol(:,1);
Y1x=I_RES_perp_pol(:,2);
Y2x=(Phse_RES_perp_pol(:,2))*(180/pi);
Y3x=I_RES_para_pol(:,2);
```

```
Y4x=(Phse_RES_para_pol(:,2))*(180/pi);
plot(X_axis,  Y1x,  '--b',X_axis,  Y2x,  'b',  X_axis,  Y3x,'--g',  X_axis,
Y4x,'g')
xlim([2.0 85.0])  % Explicitly declare this for inter-graph comparisons
ylim([-100 200])  % Explicitly declare this for inter-graph comparisons
xlabel ('Angle of Arrival (w.r.t. Normal) [deg]','fontsize',14)
ylabel ('Resultant Relative Intensity / Phase [deg]','fontsize',14)
legend_title1 = '\fontsize{14}Resultant INT (perp-pol)';
legend_title2 = '\fontsize{14}Resultant PHSE (perp-pol)';
legend_title3 = '\fontsize{14}Resultant INT (para-pol)';
legend_title4 = '\fontsize{14}Resultant PHSE (para-pol)';
legend
(legend_title1,legend_title2,legend_title3,legend_title4,'Location','Nor
thWest')
grid on;

% 23)   Now compute ratio of intensity for perpendicular polarisation to
%        that for parallel polarisation, which is Co/X polarisation ratio
in
%       ONBODY case here. WHEN DOING SO, include the original Co/X
%         polarisation of the antenna in FREE-SPACE to take this factor
into
%       account
for a=1:1:(a_max-1)
    AoA(a)=I_RES_perp_pol(a,1);
    FS_Co_X_pol_ratio_dB(a)=FS_CoXpol_ratio_dB;

On_body_Co_X_pol_ratio(a)=(I_RES_perp_pol(a,2))/(I_RES_para_pol(a,2));
    On_body_Co_X_pol_ratio_dB(a)=10*log10(On_body_Co_X_pol_ratio(a))+
FS_Co_X_pol_ratio_dB(a);
end
%FS_CoXpol_ratio_dB
On_body_Co_X_pol_ratio(1)=0;      %  Otherwise,  this  uncalculated  value
screws-up calculation of mean
% On_body_Co_X_pol_ratio
Mean_On_body_CoXpol_ratio=mean(On_body_Co_X_pol_ratio);
%On_body_Co_X_pol_ratio_dB
Mean_On_body_Co_X_pol_ratio_dB=10*log10(Mean_On_body_CoXpol_ratio)+FS_Co
_X_pol_ratio_dB;
ON_BODY_Mean_CoX_pol_ratio_dB=10*log10(mean(On_body_Co_X_pol_ratio))+FS_
CoXpol_ratio_dB

% 24)   Now plot ratio of intensity for perpendicular polarisation to
%        that for parallel polarisation, which is Co/X polarisation ratio
in
%       ONBODY case here. Also include MEAN on-body ratio
figure;               % Want a new figure - don't want to overwrite old
one
X_axis=AoA;
Y1x=FS_Co_X_pol_ratio_dB;
Y2x=On_body_Co_X_pol_ratio_dB;
Y3x=Mean_On_body_Co_X_pol_ratio_dB;
plot(X_axis, Y1x,'b', X_axis, Y2x,'r', X_axis, Y3x,'--r')
xlim([2.0 85.0])  % Explicitly declare this for inter-graph comparisons
ylim([-20 15])  % Explicitly declare this for inter-graph comparisons
xlabel ('Angle of Arrival (w.r.t. Normal) [deg]','fontsize',14)
```

```
ylabel ('Co/X-pol Ratio [dB]','fontsize',14)
legend_title1 = '\fontsize{12}Free-Space Co/X-pol ratio';
legend_title2 = '\fontsize{12}On-Body Co/X-pol ratio';
legend_title3 = '\fontsize{12}On-Body Mean Co/X-pol ratio';
legend (legend_title1,legend_title2,legend_title3,'Location','Best')
grid on;

% 25)    Finally compute Co/X-pol ratio reduction when On-Body, rather
than
%       in FS
CoX_pol_ratio_REDUCTION_dB=FS_CoXpol_ratio_dB-
ON_BODY_Mean_CoX_pol_ratio_dB
```

END OF DOCUMENT